Macroscopic bit-flip times in two-photon dissipative oscillator

Camille Berdou

PSL UNIVERSITÉ PARIS

THÈSE DE DOCTORAT
DE L'UNIVERSITÉ PSL

Préparée à Mines Paris PSL

Macroscopic bit-flip times in a two-photon dissipative oscillator

Temps de bit-flip macroscopiques dans un oscillateur pourvu de la dissipation à deux photons

Soutenue par

Camille Berdou

Le 14 mars 2023

École doctorale n°621

Ingénierie des Systèmes, Matériaux, Mécanique, Énergétique

Spécialité

Mathématique et Automatique

Composition du jury :

Per DELSING Professeur, Chalmers University of Technology	*Président du jury*
Anja METELMANN Professeure, Karlsruher Institut für Technologie	*Rapporteuse*
Patrice BERTET Directeur de recherche, CEA/Université Paris-Saclay	*Rapporteur*
Jérôme ESTÈVE Chargé de recherche, CNRS, Université Paris-Saclay	*Examinateur*
Zaki LEGHTAS Professeur, Mines Paris-PSL	*Directeur de thèse*

MINES PARIS | PSL

Résumé

Les bits quantiques, plus communément appelés "qubits", subissent encore trop d'erreurs dans leurs implémentations actuelles pour pouvoir être assemblés en processeur quantique pertinent. Ces erreurs sont de deux sortes : des erreurs de flips de bits (ou bit-flips), équivalentes aux erreurs affectant les bits classiques, et des erreurs de flips de phase (ou phase-flips), intrinsèquement dues à la nature quantique du qubit. Une stratégie originale pour contrer les bit-flips consiste à encoder l'information quantique dans deux états stables d'un oscillateur qui échange des photons par paires avec son environnement. La lignée de travaux dans laquelle s'inscrit cette thèse a démontré que ce mécanisme spécifique de dissipation fournit de la stabilité sans induire de décohérence qui détruirait les superpositions quantiques entre les états.

Ces travaux ont alors conduit à la conception d'un nouveau qubit basé sur ce mécanisme de dissipation non-linéaire : le qubit de chat, implémenté au sein du champ d'une cavité résonante réalisée dans un circuit supraconducteur. Augmenter le nombre de photons dans les états de la cavité accentue la séparation inter-états permettant des temps de bit-flips macroscopiques même pour un faible nombre de photons dans la cavité. En effet, il est important de rester dans un régime à faible nombre de photons pour que le système soit compatible avec des superpositions quantiques d'états, l'augmentation du nombre de photons accroissant par ailleurs la distinguabilité entre les états. Pourtant, même si des grands temps de bit-flips pouvaient être en principe atteints, les réalisations expérimentales précédant cette thèse saturaient à des temps de l'ordre de la milliseconde.

Le but principal de cette thèse est alors de maximiser le temps de bit-flip atteignable dans un oscillateur pourvu de la dissipation à deux photons. À partir de la réalisation expérimentale préexistante, la démarche a été de retirer du prototype tout ce qui n'était pas essentiel au processus de stabilisation à deux photons. Tout d'abord, le mécanisme d'échange à deux photons repose sur un élément non-linéaire fait à base de jonctions de Josephson. Dans cette thèse, nous nous sommes placés dans un régime à faible non-linéarités afin d'éviter de potentielles instabilités dynamiques du système. De plus, nous avons enregistré les trajectoires entre les états de la cavité de la façon la moins invasive possible, en collectant simplement la fluorescence émanant de la cavité. Toutefois, ces choix de conception de l'expérience ont abouti à un taux de dissipation à un photon supérieur au taux de dissipation à deux photons, rendant caduques la préparation et la mesure de superposition d'états quantiques.

Le résultat central de cette thèse est la démonstration expérimentale d'un temps de bit-flip de 100 secondes pour des états dans un oscillateur à dissipation à deux photons, contenant environ 40 photons. Ainsi, cette expérience démontre que des temps de bit-flips macroscopiques peuvent être atteints avec un nombre mésoscopique de photons dans la cavité, critère essentiel

pour préserver la nature quantique de l'information stockée. Ce travail constitue un point de référence pour les futures implémentations qui pourront revenir progressivement dans un régime où le taux de dissipation à deux photons dépasse celui des pertes dissipatives à un photon, ce qui permettra d'exploiter totalement la nature quantique de l'oscillateur à deux photons. Dès lors, les bit-flips étant corrigés de façon continue et autonome, il restera à utiliser les ressources de la correction d'erreur quantique pour éradiquer les flips de phase, seul canal d'erreur restant. Les performances démontrées dans cette thèse permettent ainsi d'envisager une réalisation concrète de la feuille de route menant à un ordinateur quantique universel à base de qubits de chats.

Mots clés : Correction d'erreur quantique, Circuits supraconducteurs, Jonction Josephson

Abstract

Current implementations of quantum bits, also commonly called qubits, continue to undergo too many errors to be scaled into useful quantum machines. An emerging strategy is to encode quantum information in the two meta-stable pointer states of an oscillator exchanging pairs of photons with its environment, a mechanism shown to provide stability without inducing decoherence. This strategy is at the core of a recent qubit, called the cat-qubit, which is embedded in the cavity field of a superconducting resonator with tailored interaction with its environment. Adding photons in these states increases their separation, and macroscopic bit-flip times are expected even for a handful of photons, a range suitable for quantum information processing. However, the bit-flip time demonstrated in previous experimental realizations have saturated in the millisecond range.

The primary goal of this thesis work is to maximize the bit-flip time in a two-photon dissipative oscillator, by stripping the circuit from everything we can afford and noticing how much the bit-flip time can be increased. First, the two-photon exchange mechanism is based on a non-linear circuit element made out of Joesphson junctions. In this thesis work, this circuit element is designed in a low nonlinearity regime in order to circumvent all suspected dynamical instabilities. Morevover, we employ a minimally invasive fluorescence detection tool to record the individual oscillator state trajectories. These choices come at the cost of a two-photon exchange rate dominated by single-photon loss, hence losing our ability to prepare quantum superposition states and measuring the phase-flip rate.

The main result of this thesis is the experimental demonstration of bit-flip times exceeding 100 seconds for computational states pinned by two-photon dissipation and containing about 40 photons. This experiment demonstrates that macroscopic bit-flip times are attainable with mesoscopic photon numbers in a two-photon dissipative oscillator. This thesis work is a solid foundation for future experiments that can gradually enter the regime suitable to implement a qubit where two-photon loss is the dominant dissipation mechanism. This experimental work supports the strategy of eradicating bit-flip errors continuously and autonomously at the single qubit level, and reserving the costly arsenal of measurement based quantum error correction to address the only significant remaining error: phase-flips. This work paves the way for cat-qubit based universal set of gates and phase-flip error correction, in line with the roadmap for a universal quantum computer.

Keywords : Quantum Error Correction, Superconducting circuits, Josephson junction

Contents

Acronyms

AC Alternative Current

ATS Asymmetrically Threaded SQUID

AWG Arbitrary Waveform Generator

DC Direct Current

GKP Gottesman-Kitaev-Preskill

IF Intermediate Frequency

JPA Josephson Parametric Amplifier

LO Local Oscillator

MAA Methacrylic acid

OPO Optical Parametric Oscillator

PCB Printed Circuit Board

PMMA Poly(Methyl Methacrylate)

QEC Quantum Error Correction

RF Radio Frequency

RIE Reactive Ion Etching

RWA Rotating Wave Approximation

SEM Scanning Electron Microscope

SQUID Superconducting QUantum Interference Device

TWPA Travelling Wave Parametric Amplifier

Chapter 1

Introduction

Contents

Résumé en français

Ce chapitre introductif rappelle tout d'abord des généralités à propos de l'étude des systèmes dynamiques et plus particulièrement sur la notion de stabilité, notion clef de ce domaine. Dans ce cadre, ce travail de thèse se focalise sur une classe spécifique de systèmes appelés oscillateurs paramétriques. L'étude des oscillateurs paramétriques révèle une physique très riche, avec des comportements drastiquement différents selon les régimes de paramètres. Ce chapitre aborde alors les conditions de stabilité dans le cas d'oscillateurs paramétriques linéaires et non-linéaires. Les oscillateurs paramétriques peuvent donc être utilisés pour de nombreuses applications : l'amplification paramétrique est une des plus connues et est décrite dans la suite.
Ce travail de thèse porte sur un système dynamique non-linéaire présentant deux états stables spécifiques, pouvant servir de support d'information quantique. L'objectif de cette thèse est de stocker de manière robuste de l'information quantique dans un oscillateur paramétrique non-linéaire implémenté dans un circuit supraconducteur. Ainsi, ce chapitre rappelle d'abord le cadre de l'informatique quantique à base de circuits supraconducteurs. Puis, un mécanisme spécifique de stabilité compatible avec la nature intrinsèquement fragile de l'information quantique est exhibé. Ce mécanisme est implémenté au sein de l'oscillateur muni de la dissipation à deux photons, qui est le système au cœur de ce sujet de thèse. Finalement, ce chapitre expose le cadre théorique et expérimental des études précédentes sur l'oscillateur muni de la dissipation à deux photons avant d'annoncer un plan du manuscrit.

Mechanisms for regulating and adjusting systems are common in nature and are central to the operation of many technologies and engines. A typical example of such systems is the Watt governor, invented during the industrial revolution in the 18^{th} century to regulate the operating speed of a steam-engine. In 1868, the physicist James Clerk Maxwell published a mathematical analysis of this governor system [1]. This paper is considered as a foundation for mathematical systems theory, which has gradually evolved over centuries and scientific progress. Dynamical system study is complex and rich and continue to play a major role in science and engineering today. A fundamental notion of this theory is stability which predicts whether the system can be maintained in the vicinity of a predefined state despite the presence of external perturbations.
This thesis work focuses on a system hosting two stable states in order to store quantum information. The first challenge is identifying stability mechanisms. Two ingredients are essentials for stabilizing a system in a relevant state: losses to the environment and a power supply. We focus here on a subset of systems known as parametric oscillators in which energy is supplied by modulating a parameter of the oscillator. Thanks to this specificity, parametric oscillators are hosting rich physics, with many applications, the most well-known of which is parametric amplification. Taking nonlinearities into account in those oscillators reveals multiple stable states suitable for information storage.
The second obstacle lies in the quantum nature of the information we want to store. Indeed, quantum information is inherently fragile and we must engineer a mechanism that provides stability without blurring quantum information. This thesis work focuses on a specific dissipation mechanism that simultaneously stabilizes two states while remaining compatible with their quantum superpositions.
This thesis work presents an experimental implementation of this mechanism using superconducting circuits. Performances demonstrated in this thesis provide a solid foundation for using this mechanism in future quantum computing applications.

1 Dynamical systems and stability notions

First, let us recall some basic notions of mathematical systems theory. These notions can be found in many textbooks about system dynamics, in the following we refer to [2].
A dynamical system is represented by a vectorial differential equation

$$\frac{d}{dt}\hat{x} = f(\hat{x}, t) \tag{1.1}$$

where $\hat{x} \in \mathbb{R}^n$ stores the states variables and f is a function from $\mathbb{R}^n \times \mathbb{R}^+ \to \mathbb{R}^n$. If the f function does not depend on time, the system is said to be stationary.

1.1 Steady states

The notion of equilibrium state, also called steady state, is central in the study of dynamical states. A state $\bar{x}$ is a steady state when the differential system (1.1) initialised at this point $\hat{x}(t = 0) = \bar{x}$ remains in this state for all times.

Stability notion An important notion is the stability of the steady state. An equilibrium point is stable if a small initial perturbation results in only small deviations for all subsequent times, that is to say the system stays close around this point. In the contrary case, a steady state is said to be unstable.
It is also important to study the trajectory of the system around the steady state. Indeed, there are multiples ways of evolving towards a steady state (fast convergence, cycling around the steady state,..). Mathematical tools and criteria have been developed in order to easily characterize the asymptotic evolution given a dynamical equation.

1.2 Example on the driven harmonic oscillator

The harmonic oscillator example lies at the heart of physics since it can represent first-order simplifications of a system's behavior around its stable position. Normalized position and momentum coordinates, x and p are used to parameterize the oscillator state. The harmonic oscillator has a natural frequency $\omega_0/2\pi$ and internal losses due to a finite quality factor Q. We consider here that it is driven at frequency $\omega_d/2\pi$, with a drive strength of ϵ. The differential equations of the harmonic oscillator dynamics are

$$\dot{x} = p \ , \quad \dot{p} = -\omega_0^2 x - \omega_0 Q^{-1} p + \epsilon \cos(\omega_d t) \, . \tag{1.2}$$

When this system is not driven ($\epsilon = 0$) it has one steady state which is the $(x = 0, p = 0)$ state. The losses help to bring the oscillator system to this state: they contribute to stabilize the system. In order to stabilize non-trivial states, we can turn on the drive. Exciting the oscillator at its natural frequency is the most efficient way to drive it. In the following, we will only consider the case where: $\omega_d = \omega_0$.

Poincaré maps The Poincaré map is a convenient way to visualize the system's dynamics and asymptotic behavior. We are going to introduce the Poincaré maps through the study case of the driven damped oscillator.
Looking at the system dynamics (1.2) we can see there are three variables (x, p, t). We can consider the time evolution of the system as a 3D trajectory in this coordinates space. Plus, since $\omega_d = \omega_0$, the dynamical equation is $\frac{2\pi}{\omega_0}$ periodic in time. In these conditions, it is convenient to only consider the intersections of the trajectories with a section of phase-space when studying the dynamics of the system. We choose here the section $(x, p, t = 0)$. We can define the Poincaré map on this section, which is the application defined from the section to itself, that maps a point of intersection to the next one in time. This is very useful in studying the existence of stable periodic orbits: the fixed points of a Poincaré map are periodic orbits of the full dynamics.
Figure 1.1 shows the intersection of the Poincaré section $t = 0$ with typical trajectories of dynamical system (1.2). It has a single limit orbit, and the size of that orbit is determined by the ratio between the drive strength and the damping rate.
This example brings out the two ingredients we will be experimenting with for systems' stabilization. The losses are critical for system stability. However, a drive, which is an energy input

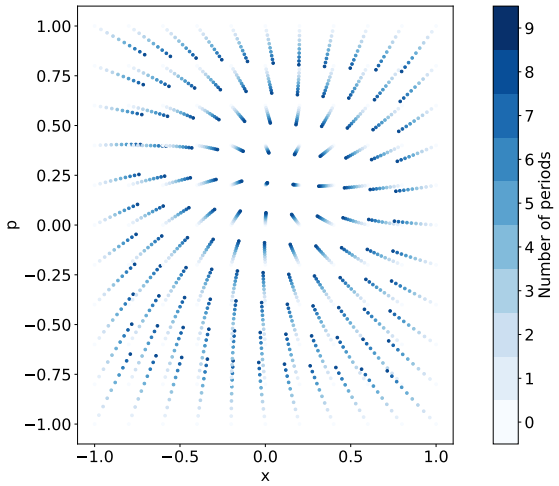

Figure 1.1: Visualization of the dynamics of a driven damped linear oscillator. Intersection of typical trajectories of the dynamical system with Poincaré section $t = 0$. Each trajectory is represented by a set of 10 points with fading color. The color of the point is darkening as the time increases: the time is indicated in the color scale in units of period of the system $\omega_0/2\pi$.The dynamics is numerically simulated using the equation (1.2) and the following parameters: natural pulsation $\omega_0 = 1$ rad.s^{-1}, losses $Q^{-1} = 5 \times 10^{-3}$, drive pulsation $\omega_d = \omega_0$ and drive amplitude $\epsilon_d = 2.5 \times 10^{-3}$. We have chosen a regime parameters in order to clearly visualize the dynamics, especially conditioning the losses rate with respect to the natural frequency. We have chosen to represent up to 10 periods in order not to overload the plot.

in the system, is required to prevent losses from bringing the system to a trivial steady state. In the following, we are going to study the interplay between those two elements in various types of driven oscillators, using the Poincaré section representation.

2 Parametric oscillator

Parametric oscillator is the generic name for an oscillator from which one parameter is modulated during the evolution. A child on a swing is the most common illustration of parametric oscillator. Indeed, a child swinging can be assimilated to an oscillating pendulum. When the child periodically stretches and folds their legs, they effectively changes their mass position along the swing rope. Since the position of the mass along the pendulum rod determines the natural frequency of this oscillator, the movement of the child periodically modulates the natural frequency of the oscillator.

Parametric oscillator are hosting rich physics, with drastically different behaviors depending on the parameter regimes. They are used in many areas in physics and in particular for amplification as it is discussed it in Section 3. In this case, the energy input is provided in a different manner than in the previous driven oscillator example. We are going to investigate the conditions that provide stability in such parametric oscillators. These results will be exploited in the following sections.

2.1 Linear parametric oscillator

First, we study a linear parametric oscillator with damping. We describe an oscillator whose resonant frequency ω_0 is periodically modulated at frequency ω_p with driving amplitude ϵ. In the lossless case, the dynamics of the oscillator is described by the Mathieu equation [3]

$$\dot{x} = p \ , \quad \dot{p} = -\omega_0^2(1 + \epsilon\cos(\omega_d t))x \, . \tag{1.3}$$

Taking into account the phenomenon of losses at a rate Q^{-1} leads to the following equation

$$\dot{x} = p \ , \quad \dot{p} = -\omega_0^2(1 + \epsilon\cos(\omega_d t))x - \omega_0 Q^{-1} p \, . \tag{1.4}$$

We refer to [4] for the study of these equations. The equation (1.4) with losses can be reduced to Mathieu equation (1.3) using an auxiliary function.
Floquet theorem implies that the time dependent solution of equation (1.3) writes for times t

$$x(t) = \exp(ict) g(\omega_p t) \tag{1.5}$$

where g is a 2π periodic function and c is the Mathieu exponent that can be solved numerically. This c exponent determines the stability of the solution, resulting in Figure 1.2 which exhibits the stable and unstable zones depending on the drive amplitude ϵ and the drive frequency ω_p. Instability lobes appear at $\omega_p = 2\omega_0/n, \ n \in \mathbb{N}$ and broaden for increasing parametric drive amplitude ϵ. The instability lobes are shifted to larger ϵ values when dissipation is added, reducing the size of the unstable zone. We should highlight that contrary to the driven damped harmonic oscillator, there are still parameters regions where the system is unstable with exponentially growing amplitudes.
Going back to the example of the child on a swing, by stretching and folding their legs, the child parametrically drives the swing. The modulation is being performed spontaneously by the child at a frequency that is twice the natural frequency of the oscillator. In this regime of modulation parameters, Figure 1.2 shows that we are in an unstable zone for zero amplitude solution for small drive amplitude. As a result, the amplitude of swing oscillations increases efficiently under the child action. Parametric oscillator can be seen as transferring energy of parametric excitation to the resonant mode of the system. Therefore, one of they major application is dedicated to amplification.
Figure 1.3 brings out the difference on the stable and unstable regions for a parametric oscillator driven at frequency $\omega_p = 2\omega_0$. Depending on the strength of the parametric drive, the solution either exponentially converges to zero or diverges towards $x = \pm\infty$ (the dissipation rate is staying the same). This behaviour with exponential amplitude greatly differs from the driven damped oscillator of the previous section.

2.2 Nonlinear parametric oscillator

We keep on focusing our analysis on the first instability lobe with frequency $\omega_p = 2\omega_0$. Our goal is now to investigate the effect of nonlinearities on parametric oscillators and to study how

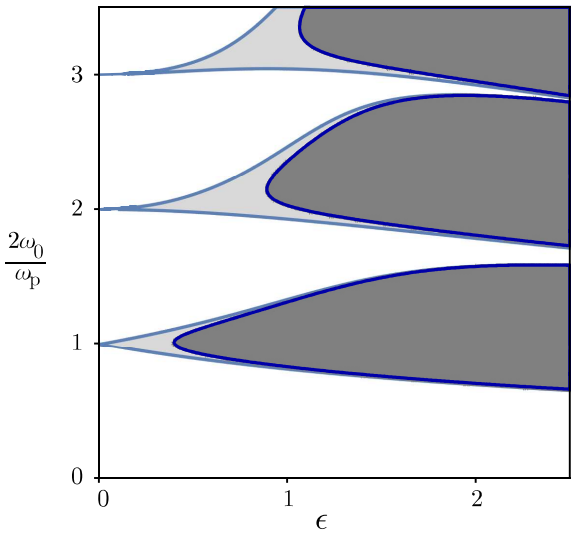

Figure 1.2: Stability diagram of the parametric oscillator as a function of inverse driving frequency $2\omega_0/\omega_d$ and driving strength ϵ in the lossless case $Q^{-1} = 0$ (light grey) and for $Q^{-1} = 0.2$ (dark grey). In the grey region the zero amplitude solution is unstable. Instability lobes appear at $2\,\omega_0/\omega_d = n,\ n \in \mathbb{N}$. The damping shifts the lobes to higher driving amplitudes. This figure is courtesy of Toni Heugel, extracted from [4].

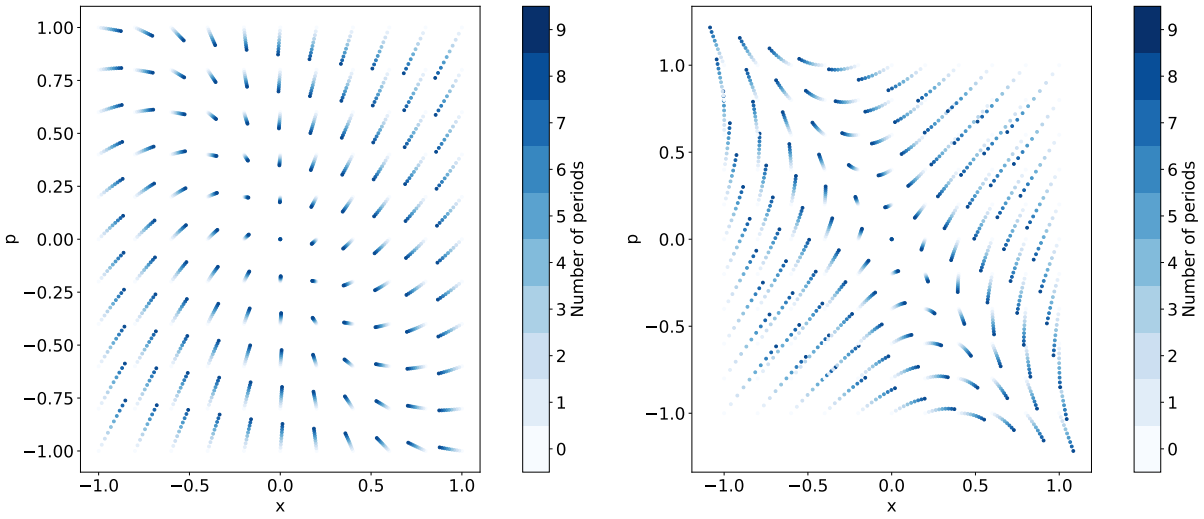

(a) Parametric drive amplitude: $\epsilon = 0.02$

(b) Parametric drive amplitude: $\epsilon = 0.05$

Figure 1.3: Visualization of the dynamics of a lossy linear parametric oscillator driven at twice its natural frequency, with different parametric drive amplitude. Intersection of typical trajectories of the dynamical system with Poincaré section $t = 0$. Each trajectory is represented by a set of 10 points with a darkening color as the time increases. The dynamics is numerically simulated using the equation (1.4) and the following parameters: natural pulsation $\omega_0 = 1$ rad.s^{-1}, losses $Q^{-1} = 5 \times 10^{-3}$, parametric drive pulsation $\omega_d = 2\omega_0$.

they can stabilize the system to a finite amplitude. Indeed, the diverging solution of Figure 1.3 is unphysical: in a real system nonlinearities prevent the divergence towards infinite amplitudes at some point.

Kerr type oscillator A first type of existing nonlinearity consists in the detuning of the natural frequency with the amplitude of oscillation. When the amplitude increases, the resonator frequency shifts while the parametric drive frequency remains constant. The parametric driving is detuned, making it less efficient and preventing oscillations amplitude from diverging. This nonlinearity is known as Kerr type because it corresponds to the Kerr effect in optics, discovered in the 19$^{\text{th}}$ century by the Scottish physicist John Kerr. The system is described by the following equation of motion, with α being the amplitude of the nonlinearity [4, 5]

$$\dot{x} = p \ , \quad \dot{p} = -\omega_0^2 \left(1 + \epsilon \cos(2\omega_0 t)\right) x + \alpha x^3 - \omega_0 Q^{-1} p \, . \tag{1.6}$$

Figure 1.4 depicts the system dynamics. The parameters of the losses and the parametric drive are the same as in the diverging case of Figure 1.3. Here, the nonlinearity implies that the system will settle to a stable state with an amplitude in between zero and infinity. There are three fixed points: one is the trivial zero amplitude one and the other two are stabilized by the natural damping of the oscillator. These two limit cycles are located at the same distance from the origin ($x = 0, p = 0$), that is to say, they have the same energy. This location is determined by the relative strengths of parametric driving, nonlinearity and system losses, as illustrated by the comparison of the three cases in Figure 1.4 where the steady point position varies with the α and Q^{-1} values.
Stability is ensured by regular energy damping and this is the main flaw of this oscillator. When comparing Figure 1.4a and 1.4c, it is appears that higher losses contribute to higher rate of convergence. Thus, if we want to boost the convergence rate towards the steady state, we have to increase the loss rate and thus deteriorate the quality factor of the resonator. This strategy does not favor encoding quantum information in this oscillator, as we will explain in the Kerr oscillator paragraph of Section 2.

Nonlinear dissipation A second type of nonlinearity exists when the losses scale with the amplitude of the oscillation. The nonlinearity amplitude is noted here η and the system dynamics is [4, 5]

$$\dot{x} = p \ , \quad \dot{p} = -\omega_0^2 \left(1 + \epsilon \cos(2\omega_0 t)\right) x - \omega_0 Q^{-1} p + \eta p^3 \, . \tag{1.7}$$

As in the previous case, Figure 1.5 exhibits three limit cycles. We recover the trivial zero amplitude state and the two limit cycles with the same amplitude. The comparison of the three parameters regimes reveals that the amplitude of the limit orbits depends on the relative strength between the nonlinearity factor η, the losses, and the parametric drive amplitude. Contrary to Figure 1.4, increasing the losses does not contribute to higher rate of convergence towards the steady states: it simply changes the location in (x, p) space of the limit cycles. Moreover, the fact that these states are indistinguishable by the drive is an important feature for the quantum

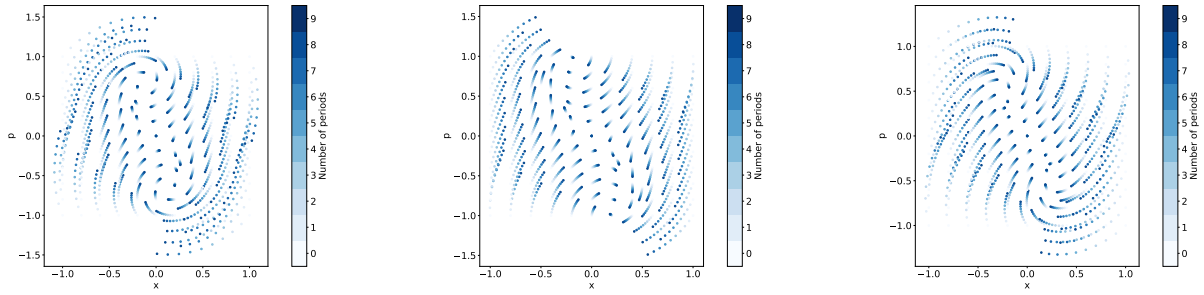

(a) $\alpha = 0.02$, $Q^{-1} = 5 \times 10^{-3}$ (b) $\alpha = 0.01$, $Q^{-1} = 5 \times 10^{-3}$ (c) $\alpha = 0.02$, $Q^{-1} = 10^{-2}$,

Figure 1.4: Visualization of the dynamics of a lossy Kerr nonlinear parametric oscillator driven at twice its natural frequency, with different ratios between nonlinearity factor and losses. Intersection of typical trajectories of the dynamical system with Poincaré section $t = 0$. Each trajectory is represented by a set of 10 points with a darkening color as the time increases. The dynamics is numerically simulated using the equation (1.6) and the following parameters: natural pulsation $\omega_0 = 1$ rad.s^{-1}, parametric drive pulsation $\omega_d = 2\omega_0$, parametric drive amplitude $\lambda = 0.02$. The losses factor and nonlinearity α are indicated below each plot.

version of the oscillator. This nonlinearity is equivalent in quantum version to a two-photon dissipation as we are going to discuss in Section 4.

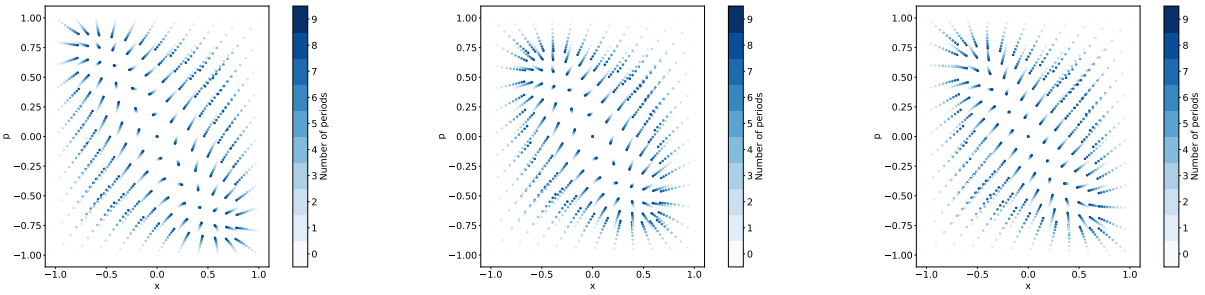

(a) $\eta = 0.01$, $Q^{-1} = 5 \times 10^{-3}$ (b) $\eta = 0.02$, $Q^{-1} = 5 \times 10^{-3}$ (c) $\eta = 0.01$, $Q^{-1} = 10^{-2}$

Figure 1.5: Visualization of the dynamics of a lossy nonlinear parametric oscillator driven at twice its natural frequency, with different ratios between nonlinearity factor and losses. Intersection of typical trajectories of the dynamical system with Poincaré section $t = 0$. Each trajectory is represented by a set of 10 points with a darkening color as the time increases. The dynamics is numerically simulated using the equation (1.7) and the following parameters: natural pulsation $\omega_0 = 1$ rad.s^{-1}, parametric drive pulsation $\omega_d = 2\omega_0$, parametric drive amplitude $\lambda = 0.02$. The losses factor and nonlinearity η are indicated below each plot.

3 Parametric amplification

The rich dynamics of parametric oscillators makes them versatile systems. One of their most common application is domain of amplification. Indeed, parametric oscillation is a way of transferring energy from parametric excitation to the resonant mode of the system. This can be used

for amplifying signal via parametric amplification. In this section, we first introduce the historical background of technological development of devices that perform parametric amplification. The principle of parametric amplification is then presented with emphasis on two applications: one in optical domain with optical parametric oscillators and the other in Radio Frequency (RF) domain with superconducting circuits.

3.1 History of parametric amplification

This subsection is based on the historical notes of [6, 7]. Parametric oscillators were first studied by Faraday, Melde and Rayleigh on mechanical systems in the 19^{th} century [8]. This then led to early 20^{th} century applications using electronic circuits to amplify and transmit radio signals. Thus, for instance, before World War I an electrical circuit with a varying inductance was used in radio telephonic communication between Vienna and Berlin [6]. This paved the way for the development of electronic parametric amplifiers throughout the twentieth century: parametric amplifiers based primarily on modulation of the capacitance of varactor diodes were widely used in RF domain. However, they were competing with other technologies in terms of gain and noise performance at microwave frequencies. In the 1970s, the transistor technology became sufficiently advanced to replace the parametric amplifiers for amplification in microwave domain. Despite this, research on microwave-frequency parametric amplifiers has continued leading to current superconducting circuits applications. Concomitantly, parametric amplification in the optical frequency range has been studied and optical parametric amplifiers are used for variety of optics applications, as described in the dedicated subsection.
The first parametric device based on a tunable inductance out of a Josephson junction has been created in 1975 [9]. With the development of quantum information, the need for low-noise amplifiers to enable highly efficient microwave measurements of quantum circuits has shifted the spotlight on superconducting parametric amplifiers. [10] is the first experimental application of a parametric amplifier for the dispersive readout of a qubit, observing quantum jumps of the qubit. Furthermore, numerous experimental results have demonstrated quantum-limited noise performance for Josephson junction based parametric amplifiers [11, 12, 13, 14].

3.2 General principle of parametric amplification

Parametric oscillators can be used in electronics or mechanical systems for signal amplification or high-precision sensing and detection. This subsection is mainly based on reviews made in [7, 15, 16].
Going back to Section 2, studying the behavior of parametric oscillators under different parameters regime reveals the possibility of amplification in specific parameter regimes. Hereafter, we introduce the general principles and terms of parametric amplification.
The modulating excitation is called the pump, at frequency f_p. This pump couples two modes called, the signal at frequency f_s and the idler at frequency f_i. Parametric excitation, in a sense, stimulates the transfer of energy from the pump to the signal. The remaining energy is routed

to another mode known as the idler. The frequency are linked by[1]

$$f_p = f_s + f_i \,. \tag{1.8}$$

This equation expresses the energy conservation, which is evident when both sides of this equation are multiplied by the Planck constant h.

Degenerated and non-degenerated amplification When the frequency of the signal and the idler are the same we call a parametric amplifier degenerated: $f_s = f_i$. In this case, the amplification is phase-sensitive, which means it can only amplify one quadrature. We recall the most famous classical illustration of parametric amplification: the child on the swing. Whenever the child reaches the maximum swing excursion, they bend or stretch their legs causing the natural frequency of the oscillator (composed of the swing and the child) to change. The signal and idler modes have the same frequency in this case (they correspond to the swinging movement with opposite phase). This pumping is performed empirically by the child at twice the natural frequency. They inject energy into the system at precisely the right time, resulting in amplification. Conversely, if the child moves their legs at the wrong time, energy is drawn out of the system, resulting in deamplification. Consequently, this example demonstrates the phase-sensitivity for degenerate parametric amplification. In the quantum limit, degenerated parametric amplification can be really useful for noiseless amplification. This regime is discussed in greater detail in the subsection devoted to Josephson parametric amplification (see Subsection 3.4).
Conversely, when the signal and the idler have a different frequency we call a parametric amplifier non-degenerated: $f_s \neq f_i$. The amplification in this case is phase-preserving: both signal quadratures are amplified with the same gain. This case will also be discussed in greater detail in Subsection 3.4.

3.3 Optical parametric oscillators

In optics, the application of parametric amplification is embedded in Optical Parametric Oscillators (OPO) devices. They are based on the use of dielectric materials in which nonlinear optical processes arise from the non-harmonical response of electric dipoles in the media when submitted to a strong electrical field [17]. Optical parametric oscillators are devices that can convert the frequency of the light emitted by a laser to another frequency, while preserving essential light properties such as temporal and spatial coherence. The generated frequencies can be tuned by adjusting the phase matching condition, which is based on the dependence of the indices of refraction upon the crystallographic orientation, temperature, light polarization, and even mechanical strain [18].
As explained in the previous section, when the signal wave is incident together with the pump on the nonlinear crystal, the signal is amplified while the pump is depleted. At the same time,

[1] In this case, the amplifier is called a three-wave parametric amplifier. Four-waves parametric amplifier can exist and the frequencies are linked in this case as: $f_p + f_p = f_s + f_i$.

an idler wave is generated at the difference frequency. Their respective frequencies match the equation (1.8). It can also be interpreted as a pump photon splitting into a signal photon and an idler photon. An OPO is realized by inserting the nonlinear crystal into an optical cavity. The signal and idler are amplified further during each round trip in the optical cavity.
There are two types of OPOs: continuous-wave OPOs and pulsed OPOs. Five years after the invention of laser, the first optical parametric oscillator was demonstrated in 1965 [19]. OPOs are used as a coherent light source in many applications, such as in spectroscopy where lasers cannot reach the infrared range. They are also widely used in quantum optics, as a reliable source of squeezed light and entangled states of light, for a variety of quantum communication and quantum computing applications.

3.4 Josephson Parametric Amplifier

Parametric amplification is also used in Josephson junction based circuit devices. Based on the reviews [15, 20, 21, 22], this subsection introduces the Josephson parametric amplifier.

Need of amplification in the quantum limit The development of quantum computing processing using superconducting circuits goes with a need of low-temperature low-noise amplifiers. Since microwave quantum signals typically contain only a few photons, they must be amplified to achieve acceptable signal-to-noise ratios. Moreover, to protect the qubit from unwanted back-action, one way flow of information through the amplification channel must be ensured: this falls under the property of nonreciprocity. In this frame, parametrically coupled systems can be used to generate nonreciprocal behavior [23, 24].

Josephson devices for amplification Modern low-noise microwave amplifiers are based on superconducting Josephson parametric devices and they allow to reach the standard quantum limit of amplification. A typical example of such a device is the flux-driven Josephson Parametric Amplifier (JPA) [25]. In this case, the JPA is composed of a superconducting quantum interference device (SQUID) combined with a coplanar waveguide resonator. The SQUID is made up of two Josephson junctions connected in a loop and can be flux-driven by an external magnetic field applied to the loop. Thus, it functions as a lossless flux-tunable inductance. First, a static DC-flux can be used to thread the loop and tune the resonator's eigenfrequency. In addition, a strong RF-flux drive at twice the resonant frequency is used to activate parametric amplification, as previously explained. As a result, weak quantum signals incident at the JPA are amplified. This example is one of the many designs and modes of operation for Josephson parametric amplifiers that have been developed to improve the amplification performances (see for example [26, 27, 28]).
The fact that this device is nonlinear is an important feature. It falls under the results of Section 2 in the nonlinear case analysis. Accordingly, since it is driven at $\omega_p = 2\omega_0$ the drive amplitude has two regimes. If the drive amplitude is less than a certain threshold, only one steady state exists, and the JPA is used as an amplifier. On the contrary, if the drive amplitude exceeds the threshold, there are two steady states with opposite phases that are a precious resource for

amplification or information storage as we will see later. In the amplifier regime, the parametric amplification can be degenerated or non-degenerated and the JPA can be used for different purposes.
This parametric amplification mechanism can also be exploited to generate quantum signals in the form of squeezed vacuum states. More generally, parametrically driven Josephson based devices can serve as a rich investigation platform to better understand the complex nonlinear dynamics of Josephson parametric oscillators [16, 29, 30] or even to study the dynamical Casimir effect [31].

Non degenerate amplification The frequency of the input signal differs from the frequency of the idler: $f_s \neq f_i$. Both quadratures are amplified equally in this situation and the JPA serves as a phase-preserving amplifier. Due to the standard quantum limit, phase-preserving amplifiers must add at least 1/2 of photon of quantum noise in the amplified signal [32]. The JPA achieves this limit with excellent noise performances and are commonly used as low-noise amplifiers of microwave signals in the GHz regime (for examples of high-performances JPA, see [13, 14]).

Degenerate amplification The signal and idler have the same frequency in this case: $f_s = f_i$. The JPA functions as a phase sensitive amplifier, amplifying the two quadratures with different gains. In this case, JPAs allow for amplification on one quadrature without adding any additional noise to the signal (since in this case we are only interested in one quadrature, the noise can be "thrown away" in the other quadrature [32]). Experiments have demonstrated that JPAs can phase-sensitively amplify weak microwave signals with a noise performance reaching the standard quantum limit [33].

Amplification thanks to phase detection Above the drive amplitude threshold, the JPA behaves like a Josephson parametric phase-locked oscillator, with two dynamical coherent states inside the oscillator [34]. This device can be used as a sensitive phase detector, and switching between these states has been used for amplification for a long time [35, 36].

4 Macroscopic bit-flip time in a two-photon dissipative oscillator

The precedent sections have demonstrated that a nonlinear dynamical system that interacts with its environment in a specific way exhibits a rich dynamical phase space hosting multiple stable steady states. As stated above, this can be beneficial for the amplification domain in both the classical and quantum worlds. This section now focuses on a different application. In this thesis work, we use those properties to store quantum information in a nonlinear parametrically driven oscillator implemented in a superconducting circuit.

4.1 Quantum information with superconducting qubits

Quantum information is stored on a two-level quantum system, called qubit, that is the quantum equivalent of a classical bit. The main distinction between a quantum bit and a classical bit, is that a quantum bit can be in a superposition of its two basis states, $|0\rangle$ and $|1\rangle$ also referred to as the computational basis. Due to the coupling to its environment the qubit is plagued by errors that should be corrected. The first type of error is a bit-flip error, which is equivalent to the classical bit-flip error in that it inverts the $|0\rangle$ and $|1\rangle$ states. The second type of error is a phase-flip error, which typically swaps the $|0\rangle + |1\rangle$ state to $|0\rangle - |1\rangle$ state. These errors are inherent in the quantum nature of the qubit and have no classical equivalent.
Quantum Error Correction (QEC) is a protocol developed in the 1990s in order to fight against those errors. It entails encoding quantum information across large ensembles of qubits rather than in a single qubit. By periodically detecting and correcting errors, the ensemble, called a logical qubit, is more stable than each individual part. The hardware overhead which quantifies the number of physical qubits required to encode a single logical qubit is the key parameter in QEC. Nowadays, experimental implementations are still on a race to decrease this overhead.

Superconducting qubits The development of quantum information came along with different promising physical supports for storing quantum information, such as electronic or nuclear spins [37], trapped ions [38], ultra-cold atoms [39, 40], or photons [41, 42]. In this thesis, we consider the qubit implementation in superconducting circuits. Quantum information is encoded in natural microscopic quantum systems in all of the implementations mentioned above. Superconducting qubits, on the other hand, are macroscopic in size and the superconducting properties are essential for creating collective motions of the current carriers, leading to quantization of energy levels of those circuits [43]. The typical electromagnetic modes of superconducting circuits are in frequency range of GHz and have a naturally excellent quality factor thanks to superconductivity. The Josephson junction, which functions as a nonlinear inductor component, is another essential component of superconducting circuits. This component provides an easily tunable nonlinearity and brings non-trivial dynamics to the circuits without inducing dissipation. Superconducting circuits are patterned on typical micrometer dimensions using lithography techniques and gaining from the expertise of semiconductor industry. Working in the GHz frequency range also benefits from the RF-industry know-how.

4.2 Nonlinear parametric oscillators as logical circuit elements

Recent experimental advances have rekindled interest in parametric oscillators in both the classical and quantum regimes. This subsection describes various types of nonlinear parametric oscillators that are used to store information. The key issue in storing quantum information is to find a stabilization mechanism that is compatible with quantum coherences.

Nonlinear parametric oscillator for classical information Nonlinear parametric oscillating electronic devices were used to store digital information at the dawn of the digital era. Indeed, we demonstrated in Section 2 that the nonlinearity of the parametric oscillator generates

two stable oscillation states with equal amplitude and opposite phase. They can be considered as elementary information units for computation and data storage, with one phase state labeled as the "0" state and the other as the "1" state. Thus [44] has invented the "parametron" in the 1950s which is a logic circuit element made of nonlinear inductances of ferrite-core coils. This device was widely used as a basic element in Japanese electronic computers at the time before being surpassed by transistor elements [45].
The bistability of nonlinear resonators can also be exploited for ultra-low energy classical logic. Theoretical proposal [46] suggests to implement photonic sequential logic by using optical Kerr resonators containing a handful of photons, the binary logic gates being generated by interference effects. Based on the same principle, [47] is an experimental realization of a latch[2] in a superconducting circuit for classical logic.

Schrödinger cat states as a quantum information storage resource In the traditional QEC approach, the physical qubits are implemented in discrete two-level physical systems. Then, the usual QEC schemes require a large number of ancillary systems and interconnected qubits. These interconnections are the entry points for errors that are detrimental for the overall device performance. A more resource-efficient method, on the other hand, is to encode a logical qubit in the states in the phase-space of a single oscillator. This strategy is at the core of the corrections codes denoted as bosonic codes [48], which include the binomial codes [49], the GKP codes [50] or the four-legged Schrödinger cat codes [51]. Here, we focus on the two-legged Schrödinger cat codes based on the superpositions of coherent states of the oscillator, with equal amplitude and opposite phase (those states are denoted as the Schrödinger cat states, hence the code name). If we note down $|\alpha\rangle$, the coherent state in the oscillator of complex amplitude $\alpha \in \mathbb{C}$, the qubit computational basis is

$$\begin{aligned} |+\rangle_\alpha &\propto |+\alpha\rangle + |-\alpha\rangle \quad ; \quad |-\rangle_\alpha \propto |+\alpha\rangle - |-\alpha\rangle \\ |0\rangle_\alpha &= \frac{|+\rangle_\alpha + |-\rangle_\alpha}{\sqrt{2}} = |+\alpha\rangle + \mathcal{O}(e^{-2|\alpha|^2}) \quad ; \quad |1\rangle_\alpha = \frac{|+\rangle_\alpha - |-\rangle_\alpha}{\sqrt{2}} = |-\alpha\rangle + \mathcal{O}(e^{-2|\alpha|^2})\,. \end{aligned} \tag{1.9}$$

Note that the amplitude squared of the coherent states corresponds to the number of photons in the resonator $\bar{n} = |\alpha|^2$, and thus determines the size of the cat code. One main advantage of the two-legged cat code is that it is intrinsically resilient to bit-flip errors as we will explain in next subsection. It is called biased-noise since the other error type (phase-flip error) occurs with a much higher probability than the bit-flip error. It is beneficial since the next QEC layer only has to tackle one single type of errors.
Single photon losses are the dominant error for a quantum harmonic oscillator. As a result, a cat state prepared in an undriven harmonic oscillator will leak out of the code space and eventually decay to the vacuum state. At the very least, some energy input has to be provided to maintain the cat state. We recover the two ingredients, losses and additional energy supply, as we discussed previously. Nonlinearities are essential to implement an autonomous stabilization of

[2] A latch, or a flip-flop, is an electronic logical circuit. It has two states and it can be flipped from one state to the other by an external signal.

the cat states. Moreover this stabilization mechanism has to supply energy and evacuate entropy from the system in a way that is entirely agnostic to the oscillator state. This autonomous stabilization can be realized in two ways described in the following paragraphs. The article [52] compares the strengths and weaknesses of both approaches and suggests a new efficient confinement scheme inspired by both methods.

Kerr nonlinear oscillator The first strategy to stabilize the cat states relies on engineered Hamiltonian. It is based on a Kerr nonlinear resonator endowed with two-photon driving [53]. This is the quantum equivalent of the nonlinear parametrically driven oscillator with dynamics of equation (1.6). The cat states of equation (1.9) are exactly the degenerate states of the Kerr nonlinear resonator under two-photon driving, even in presence of single photon losses. As highlighted in Section 2, raising the single photon losses will increase the rate of convergence towards the steady states. Large single photon loss rate, on the other hand, is detrimental for the qubit coherences. This is why, this nonlinear oscillator has to be implemented in a regime where the Kerr nonlinearities dominate over the single photon losses. This autonomous stabilization scheme was implemented in a superconducting circuit in [54, 55]. This was realized using a nonlinear superconducting resonator, with a nonlinearity provided by a Josephson based component. In this experiment, a complete set of single-qubit gates were performed on timescales faster than the shortest system coherence time. Readout of the qubit state in a quantum non-destructive way in presence of the stabilization mechanisms was also demonstrated.

Two-photon dissipative oscillator The second strategy to stabilize the cat states is based on engineered dissipation. Experiments [56, 57] were demonstrations of stabilization of a single quantum state via a tailored interaction with an auxiliary dissipative system. Here, the challenge is to stabilize all the superpositions of the computational basis states. It is realized in a nonlinear resonator that only exchanges pairs of photons with its environment. This specific dissipation pins down the cavity field on the cat states of (1.9) without affecting their quantum superpositions. This mechanism is the quantum equivalent of the nonlinear parametrically driven oscillator (see equation (1.7)). In this frame, the two stabilized states cannot be distinguished by the parametric drive, which is essential for being compatible with quantum information storage.

Experimental realizations in superconducting circuits of this two-photon dissipation for stabilizing quantum information [58, 59] are based on the use of Josephson junctions as nonlinear wave-mixing elements. Interestingly, a new approach [60] shows that this dissipative process could also be engineered via the nonlinear coupling of a microwave mode to a tunnel junction. The tunnelling process between the two reservoirs on both junction sides creates the dissipation in the microwave mode, that can be tuned in terms of the number of involved photons.

Finally, this dissipative approach defies the common intuition that a qubit must be well isolated from its environment. Autonomous stabilization using two-photon dissipation is at the center of this thesis work and next section focuses on the experimental realizations in superconducting circuits.

4.3 The two-photon dissipative oscillator experiment

In this thesis work, we aim for the maximum bit-flip time we could achieve in a two-photon dissipative oscillator implemented in a superconducting circuit. Indeed, thanks to the engineered interaction with the environment, the two-photon dissipative oscillator is a new architecture for storing information with macroscopic bit-flip times. The thesis experiment demonstrates bit-flip times of the order of 100 seconds for states in the resonator pinned by two-photon dissipation and containing about 40 photons. Accordingly, this work supports the strategy of eradicating bit-flips continuously and autonomously at the hardware level, thus reducing the overhead required for a fully protected logical qubit.

Exponential suppression of bit-flip errors As exposed before, the cat qubit is noise-biased. The parameter setting the bit-flip time in the cat qubit experiment is the number of photons in the cavity. Increasing the number of photons $\bar{n} = |\alpha|^2$ in these two steady states has two opposing effects [59]. On the one hand, their distinguishability by an inevitably coupled uncontrolled environment increases linearly with $\bar{n}$. This results in a linear increase of the phase-flip error rate. Therefore, for this system to be suitable for quantum information processing, it must operate at low photon number. On the other hand, as soon as the states separation exceeds their vacuum fluctuations, that is $|\alpha-(-\alpha)|^2 = 4\bar{n} > 1$, the states wave-function overlap rapidly decreases, reducing random tunneling between them and hence exponentially increasing the bit-flip time. It is remarkable that, at least in principle, it is possible to reach macroscopic bit-flip times with computational states pinned down by two-photon dissipation containing only a handful of photonic excitations.

Previous experiments with limited bit-flip times Previous experiments have succeeded in implementing a two-photon exchange mechanism to observe the squeezing of a Schrödinger cat state out of vacuum [58], the dynamics of a quantum gate [61], the exponential suppression of bit-flips and linear increase of phase-flips [59]. However, in all these implementations, the bit-flip time saturated in the millisecond range, limited by errors impinging from the cat-qubit tomography apparatus [59], and possible dynamical instabilities [62, 63]. Progress towards a cat-qubit quantum processor [64, 65, 66], with a universal set of gates and phase-flip error correction, first requires the demonstration of macroscopic bit-flip times for a cavity field containing only a handful of photons.

Presentation of the experiment In this thesis experiment, we aim for the maximum bit-flip time we could achieve in a two-photon dissipative oscillator. To reach this goal, we first design a circuit with the objective of removing all suspected sources of dynamical instabilities and ancillary systems that could propagate uncorrectable errors. We fabricate a two-photon exchange dipole element close to the regime where its energy landscape exhibits a single global minimum at any operating point, a possible requirement for stability [63, 67]. Second, we entirely remove the tomography apparatus: our design does not contain a transmon and readout mode. Instead, we directly measure the field radiated by the cavity through a travelling wave

parametric amplifier (TWPA), thereby accessing individual oscillator state trajectories. Figure 1.6 summarizes the principle of this experiment.

Our design choices come at the cost of a two-photon exchange rate dominated by single-photon loss, hence losing our ability to prepare quantum superposition states and hence measuring the phase-flip rate. Nevertheless, since quantum fluctuations play a central role in this experiment, a full quantum model is necessary to explain our data. However, in this thesis experiment, we measure a bit-flip time exceeding 100 seconds for computational states pinned by two-photon dissipation and containing about 40 photons. Thus, this proves that nothing at the core of the two-photon exchange mechanism is detrimental for reaching macroscopic bit-flip times. It also demonstrates the efficiency of the two-photon dissipative oscillator as an information storage resource. This thesis work is an appropriate benchmark for future experiments that can then gradually go back to the regime suitable to implement a qubit where two-photon loss is the dominant dissipation mechanism.

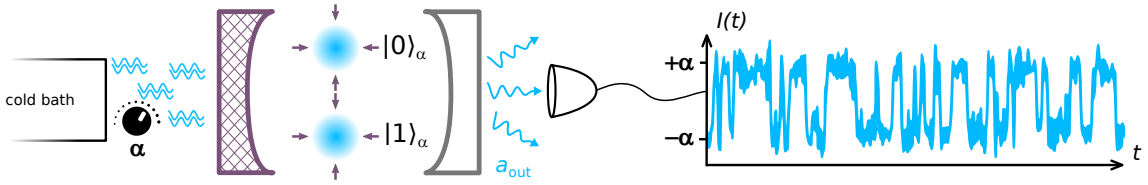

Figure 1.6: Principle of the two-photon dissipative oscillator experiment. A cavity is endowed with a special mechanism (dashed left mirror) that exchanges pairs of photons (blue double waves) at variable intensity (control knob) with a cold bath. Two meta-stable pointer states emerge, represented by the blue distributions centered around amplitudes $\pm\alpha$. A fraction of the cavity field (blue waves) escapes through the weakly transmissive mirror and is collected by our heterodyne detector. By monitoring the signal over time, we track individual trajectories undergoing bit-flips (blue time trace).

5 Outline and contributions

My main contributions to this project were the design and fabrication of all the samples described in this manuscript. Data acquisition was carried out by Anil Murani and Zaki Leghtas, and the photon number calibration of the two-photon dissipative oscillator experiment was conceived and implemented by Ulysse Réglade.

The two-photon dissipative oscillator experiment is central to this thesis work, and is described in Chapter 2 on the basis of [68]. This chapter first focuses on the experimental device, and on the calibration protocol for activating the two-photon interaction to stabilize the resonator states. We recall that the calibration of the photon number in the resonator state is a key feature of this experiment. Thus, this chapter exposes the photon number calibration method which is then used to investigate the time dynamics of the state in the resonator on short and long timescales. Statistics on the time trajectories reveal the macroscopic bit-flip times that this experiment device can achieve.

Since the photon number calibration of the resonator states is critical, we independently proceed to another calibration method in Chapter 3. In the main experiment displayed in Figure 1.6, there is no in situ component to directly measure the photon number in the cavity. Then, in order to calibrate the photon number in the resonator, we fabricate a new device composed of the two-photon dissipative oscillator coupled to a transmon.
The final two chapters of this manuscript are devoted to my principal contributions on the experiment of [68]. First, the two-photon dissipative oscillator is implemented in a circuit quantum electrodynamics coplanar waveguide architecture. Then, on-chip RF elements had to be designed to make the entire circuit operational. Chapter 4 focuses on RF design and electromagnetic simulations of coplanar structures.
Finally, I fabricated all the devices described in this manuscript. The experiment samples are composed of coplanar waveguide structures and Josephson junctions. The methods for the nanofabrication of these elements are presented in Chapter 5.

Chapter 2

Two-photon dissipative oscillator experiment

Contents

Résumé en français

Le travail de cette thèse vise à maximiser le temps de bit-flip atteignable par un oscillateur pourvu de la dissipation à deux photons (cet oscillateur est aussi appelé dans la suite « cavité »). Ce chapitre présente l'expérience conduite dans ce but et qui est développée dans l'article [68]. Tout d'abord, la première section décrit les différents éléments composant le circuit de cette expérience et détaille des choix de conception pour ce prototype. Ensuite, la deuxième section présente les calibrations nécessaires pour atteindre le régime d'échange à deux photons pour l'oscillateur. De plus, dans cette expérience, il est crucial de connaitre le nombre de photons dans les états de la cavité : le procédé de calibration du nombre de photons est alors le sujet de la troisième section. Une fois les calibrations réalisées, l'état de la cavité peut être mesuré et son évolution peut être suivie dans le temps. La dernière section révèle alors les dynamiques de l'évolution temporelle des états de la cavité sur différentes échelles de temps. L'étude statistique de ces trajectoires temporelles permet de déterminer le temps de bit-flip atteignable au sein de cet oscillateur à deux photons. Finalement, un temps de bit-flip de plus de 100 secondes a été mesuré pour des états de la cavité contenant environ 40 photons.

In this thesis work, we aim for the maximum bit-flip time we could achieve in a two-photon dissipative oscillator. To reach this goal, we devise a Josephson circuit in a regime that circumvents all suspected dynamical instabilities, and we employ a minimally invasive fluorescence detection tool, at the cost of a two-photon exchange rate dominated by single-photon loss. We measure a bit-flip time exceeding 100 seconds for computational states pinned by two-photon dissipation and containing about 40 photons.
This chapter presents the two-photon dissipative oscillator experiment, based on the article [68]. First, the different elements composing the circuit of the experiment are introduced in Section 1. Then, Section 2 details the Direct Current (DC) and Radio Frequency (RF) calibration to achieve the two-photon exchange regime in the cavity. A crucial feature is the knowledge of photon number in the cavity states and the photon number calibration is the focus of Section 3. With all those calibrations, we can record and track the evolution of the cavity state: Section 4 studies the time dynamics of the memory states on short and long timescales. Statistics performed on the time trajectories reveal the bit-flip times we can achieve with this device.

1 Circuit analysis

The two-photon dissipative oscillator is embedded in the cavity field of a superconducting resonator that exchanges pairs of photons with its environment [51, 58, 69]. The cavity will be referred in the following as the memory. This interaction relies on the insertion of a circuit element that mediates a nonlinear coupling between the resonator and its environment. This circuit element is a nonlinear inductive dipole called Asymmetrically Threaded SQUID (ATS). It is composed by a SQUID split in its center by an inductance. The ATS can be biased with DC flux and we have to be at a specific operating flux point in order to activate the two-photon coupling interaction.
This section presents the different components of the two-photon dissipative oscillator circuit and demonstrates how the Hamiltonian of the total system can be reduced to a two-photon coupling dynamics.

1.1 The two-photon dissipative oscillator

An oscillator exchanging pairs of photons with its environment in addition to usual energy relaxation is modeled by the following Hamiltonian and loss operators

$$H_2/\hbar = i\epsilon_2 a^{\dagger 2} - i\epsilon_2^* a^2, \quad L_2 = \sqrt{\kappa_2}a^2 \ , \quad L_1 = \sqrt{\kappa_a}a \ , \tag{2.1}$$

where a is the annihilation operator of the mode referred to as the memory, ϵ_2 is the two-photon injection rate, κ_2 the two-photon loss rate, and κ_a is the energy damping rate. When the two-photon injection rate overcomes the damping rate, two meta-stable pointer states emerge

$$|0\rangle_\alpha = |+\alpha\rangle + \mathcal{O}(e^{-2|\alpha|^2}) \ , \quad |1\rangle_\alpha = |-\alpha\rangle + \mathcal{O}(e^{-2|\alpha|^2}) \ ,$$

where $|\alpha\rangle$ is a coherent state with complex amplitude α, verifying $\alpha^2 = \frac{2}{\kappa_2}(\epsilon_2 - \kappa_a/4)$ if $\epsilon_2 > \kappa_a/4$, and $\alpha^2 = 0$ otherwise.
Importantly, note that the confinement of the computational states $|0,1\rangle_\alpha$ is ensured by the two-photon damping process. The two-photon dissipation mechanism is engineered by implementing a two-to-one photon exchange interaction with a dissipative mode referred to as the buffer [58], modeled by the Hamiltonian

$$H_{ab}/\hbar = g_2^* a^2 b^\dagger + g_2 a^{\dagger 2} b - \epsilon_d b^\dagger - \epsilon_d^* b \,, \tag{2.2}$$

where b is the annihilation operator of the buffer, g_2 is the two-to-one photon coupling rate and ϵ_d the buffer drive amplitude. In the limit where the buffer energy decay rate κ_b is larger than $|g_2|$, as explained in [58] we recover eq. (2.1) with the correspondence

$$\begin{aligned} \kappa_2 &= 4|g_2|^2/\kappa_b \\ \epsilon_2 &= 2g_2\epsilon_d/\kappa_b \,. \end{aligned} \tag{2.3}$$

1.2 Circuit presentation

Our two-photon dissipative oscillator is implemented in a circuit quantum electrodynamics coplanar waveguide architecture. Figure 2.1 displays the circuit chip and Figure 2.2 presents a lumped element model of the circuit. The wiring setup of the experiment is exposed in Figure 2.3.

The memory The memory mode is the fundamental mode of a $\lambda/2$ resonator. We measure coupling and internal loss rates $\kappa_a^c/2\pi = 40$ kHz and $\kappa_a^i/2\pi = 18$ kHz. In order to minimize dielectric losses [70], we target the relatively low frequency of $\omega_a/2\pi = 4.0457$ GHz. An undesired side effect of coupling the memory to a lossy mode – the buffer – is to increase the decay rate of the memory due to the Purcell effect. To prevent this, we designed a stop-band filter centered at the memory frequency, consisting of three $\lambda/4$ sections on both routes linking the memory to its cold bath. The RF design of those filters is presented in Chapter 4.
A thermal population of about 1% was measured on a twin sample using a transmon: this measurement is detailed in Chapter 2, Section 3.

Buffer mode The buffer mode consists of a metallic plate of charging energy $E_C/h = 73$ MHz shunted to ground through an ATS [59]. The ATS is formed by two Josephson junctions in a loop – each of Josephson energy $E_J/h = 37$ GHz – split in its center by an inductance made of five junctions of total inductive energy $E_L/h = $ 62 GHz. A picture of the device's Josephson junctions is presented in Chapter 5 dedicated to the nanofabrication processes. This layout defines two loops that can be biased in DC flux $\varphi_{L,R}$. We can hence independently control the common and differential flux through the ATS: $\varphi_\Sigma = \frac{1}{2}(\varphi_L + \varphi_R)$ and $\varphi_\Delta = \frac{1}{2}(\varphi_L - \varphi_R)$. Radio-frequency signals are routed to the ATS through a 180° hybrid coupler. The buffer drive propagates in phase through both arms of the two-photon exchange apparatus. When reaching the ATS, these waves combine, inducing currents in the inductance and thereby driving the buffer mode. On the other hand, the pump propagates with opposite phases, inducing common

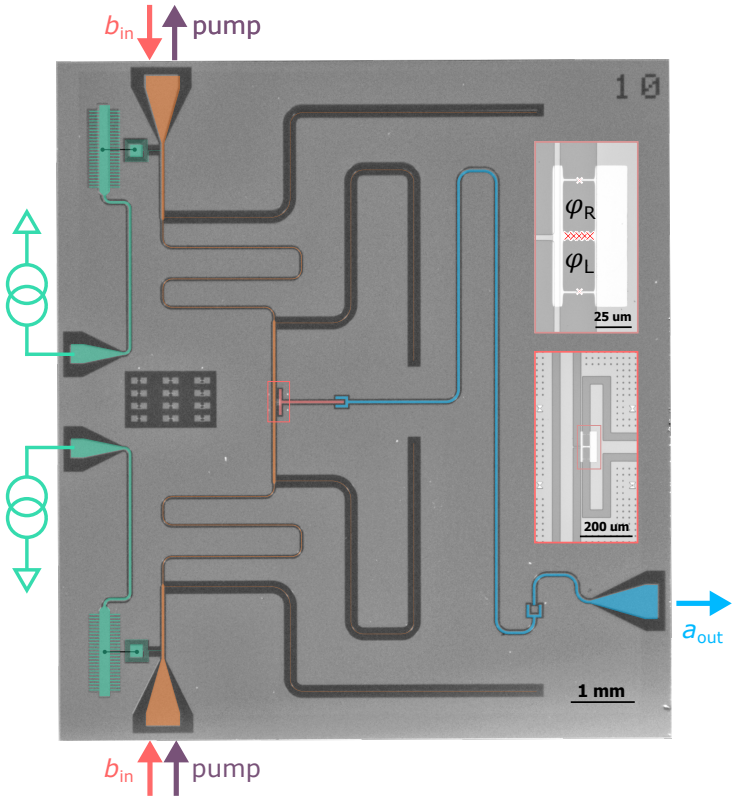

Figure 2.1: False-color optical micrograph of the experimental superconducting circuit in a coplanar waveguide geometry. The cavity is a $\lambda/2$ resonator (blue) that radiates a field a_{out} through a weakly coupled 50 Ω port. The cavity also couples to a two-photon exchange device composed of a buffer mode (red) shunted to ground through an asymmetrically threaded SQUID (ATS) as emphasized in the insets. DC currents enter through on-chip bias tees (green) and impose phase biases $\varphi_{L,R}$. A differential pump (purple arrows) and a common buffer drive (red arrows) are channeled through filtered transmission lines (orange).

flux in the ATS. At the experiment operating point the buffer resonates at $\omega_b/2\pi = 6.1273$ GHz with an energy decay rate $\kappa_b/2\pi = 16$ MHz (see Section 2).
Both RF drives and DC currents are routed to the ATS thanks to on-chip bias tees, whose design is described in Chapter 4.

Tomography part Previous experiments constructed the Wigner distribution of the memory field using a nonlinear coupling of the memory resonator to a transmon qubit and its readout resonator [59]. However, the finite thermal occupation of the transmon was suspected to limit the bit-flip time to the millisecond range (see Section 1 of Chapter 3). Instead, we monitor our memory through a minimally invasive detection tool: a weakly coupled transmission line connected to a TWPA. This added leakage channel slightly decreases the total quality factor but has the advantage of not inducing any additional nonlinear couplings to a lossy ancillary system.

1.3 Circuit Hamiltonian

The dynamics of the circuit displayed in Figure 2.1 is well captured by a reduced lumped element model (see Figure 2.2) with the following Hamiltonian [59]

$$H = \hbar\omega_{a,0}a^\dagger a + \hbar\omega_{b,0}b^\dagger b - 2E_J\cos(\varphi_\Sigma)\cos(\varphi+\varphi_\Delta) + 2\Delta E_J\sin(\varphi_\Sigma)\sin(\varphi+\varphi_\Delta) \tag{2.4}$$

where a, b are the memory and buffer annihilation operators. The buffer's angular frequency verifies $\omega_{b,0} = \sqrt{8E_LE_C}/\hbar$, where E_L, E_C are the energies associated to the buffer's inductive and capacitive shunt respectively. The angular frequency of the memory is denoted $\omega_{a,0}$. We denote $2E_J$ the sum of the Josephson energies of the single junctions composing the SQUID loop, and $2\Delta E_J$ their difference.
The ATS is threaded with a common and differential flux $\varphi_{\Sigma,\Delta} = \frac{1}{2}(\varphi_L \pm \varphi_R)$, where $\varphi_{L,R}$ is the flux threading the left and right loop of the ATS. The buffer and memory modes hybridize through their capacitive coupling. In the limit where the hybridization factor υ between the buffer and memory is much smaller than 1, the phase across the ATS denoted φ, verifies $\varphi = \varphi_b\left(b + b^\dagger + \upsilon(a+a^\dagger)\right)$, where the zero point phase fluctuations for the buffer reads $\varphi_b = (2E_C/E_L)^{1/4}$.

Self-Kerr sources During the fabrication process, we aim for the smallest possible junction asymmetry. However in practice we are left with $\Delta E_J/E_J \approx 0.5\%$ (see Table 2.1) which leads to spurious Kerr and cross-Kerr effects. Actually, self-Kerr terms on the buffer can come from two main sources.

- Asymmetry ΔE_J between the two junctions of the ATS creates Kerr term, expressed at the saddle point of our experiment as: $\chi_{bb}^{\Delta E_J} = -\Delta E_J\varphi_b^4$.
- Finite number $N_J = 5$ of Josephson junctions composing the array of the central inductance leads to Kerr term: $\chi_{bb}^{N_J} = -\frac{E_L}{2N_J^2}\varphi_b^4$.

Subsection 4.2 presents a discussion on these self-Kerr estimated values thanks to a comparison between numerical simulation and recorded experimental data of buffer dynamics.

1.4 The Asymmetrically Threaded SQUID

The Asymmetrically Threaded SQUID (ATS) is the nonlinear inductive dipole that mediates the exchange of pairs of photons between the memory and its environment. This dipole consists of a SQUID split in its center by an inductance at a specific DC flux bias and is represented by the circuit of Figure 2.2.
The inductive energy of the ATS writes (see [59])

$$U_{\varphi_\Sigma,\varphi_\Delta}(\varphi) = \frac{1}{2}E_L\varphi^2 - 2E_J\cos(\varphi_\Sigma)\cos(\varphi+\varphi_\Delta) + 2\Delta E_J\sin(\varphi_\Sigma)\sin(\varphi+\varphi_\Delta)\,, \tag{2.5}$$

where E_L is the inductive energy of the shunt inductance, $E_J \pm \Delta E_J$ are the Josephson energies of the left and right Josephson junctions respectively, φ is the superconducting phase difference

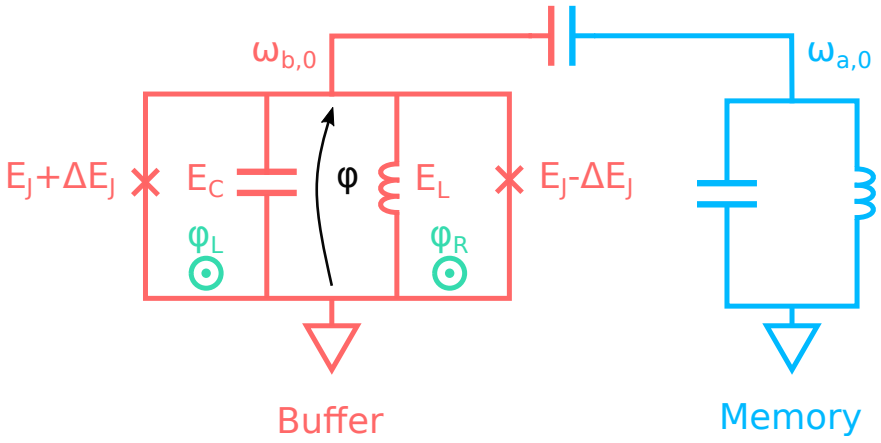

Figure 2.2: Lumped element model of the circuit. The buffer (red) with bare frequency $\omega_{b,0}/2\pi$ is constituted with an ATS (inductive energy E_L, mean Josephson energy E_J, asymmetry ΔE_J), and a capacitor with charging energy E_C. The ATS loops are threaded with fluxes φ_L, φ_R (green). The buffer is connected to the memory (blue), with bare frequency $\omega_{a,0}/2\pi$. The phase φ is indicated with an arrow (black).

across the ATS and $\varphi_{\Sigma,\Delta} = (\varphi_L \pm \varphi_R)/2$ are related to the common and differential flux threading the ATS with $\varphi_{L,R}$ threading the left and right loop of the ATS respectively.

Symmetries The ATS potential has the following translational symmetries

$$U_{\varphi_\Sigma,\varphi_\Delta}(\varphi) = U_{\varphi_\Sigma+\pi,\varphi_\Delta+\pi}(\varphi) = U_{\varphi_\Sigma+\pi,\varphi_\Delta-\pi}(\varphi)\,. \tag{2.6}$$

and an inversion symmetry center at $(\varphi_\Sigma, \varphi_\Delta) = (\pi/2, \pi/2)$ such that

$$U_{\pi/2+\varphi_\Sigma,\pi/2+\varphi_\Delta}(\varphi) = U_{\pi/2-\varphi_\Sigma,\pi/2-\varphi_\Delta}(-\varphi)\,. \tag{2.7}$$

Combining these three symmetries gives rise to a second inversion symmetry center located at $(\varphi_\Sigma, \varphi_\Delta) = (\pi/2, -\pi/2)$. Hence, all the information about the system is contained in the region $\varphi_\Sigma \in [0, \pi]$, $\varphi_\Delta \in [-\pi/2, \pi/2]$. Note that provided $\Delta E_J = 0$, we have additional symmetry axes $\varphi_\Sigma = 0$ and $\varphi_\Delta = 0$ such that

$$U_{\varphi_\Sigma,\varphi_\Delta}(\varphi) = U_{-\varphi_\Sigma,\varphi_\Delta}(\varphi) = U_{\varphi_\Sigma,-\varphi_\Delta}(-\varphi)\,. \tag{2.8}$$

Note that expanding the potential in power series, $U(\varphi)$ and $U(-\varphi)$ will have the same even terms and odd terms that differ by just a sign. Consequently, the effective inductance (second derivative) and Kerr or cross-Kerr nonlinearities will be the same for $U(\varphi)$ and $U(-\varphi)$.

Saddle points Let us study the potential around the inversion symmetry points $(\varphi_\Sigma, \varphi_\Delta) = (\pi/2 + \epsilon, \pm\pi/2 + \delta)$

$$U(\varphi, \epsilon, \delta) = \frac{1}{2}E_L\varphi^2 \mp 2E_J \sin(\epsilon)\sin(\varphi + \delta) \pm 2\Delta E_J \cos(\epsilon)\cos(\varphi + \delta)\,. \tag{2.9}$$

For small ϵ and δ

$$\begin{aligned} U(\varphi, \epsilon, \delta) = &\frac{1}{2}E_L\varphi^2 \\ &\mp (-2\Delta E_J + 2E_J\epsilon\delta + \Delta E_J(\epsilon^2 + \delta^2))\cos(\varphi) \\ &\mp (2E_J\epsilon + 2\Delta E_J\delta)\sin(\varphi)\,. \end{aligned} \tag{2.10}$$

For $\epsilon = \delta = 0$, the potential reaches its minimum at $\varphi_{\min} = 0$. At $\epsilon, \delta \neq 0$, we search for a first order perturbation of $\varphi_{\min}$. Solving for $\frac{\partial}{\partial_\varphi}U(\varphi_{\min}, \epsilon, \delta) = 0$, we get

$$\varphi_{\min} = \pm\frac{2E_J\epsilon + 2\Delta E_J\delta}{E_L \mp 2\Delta E_J}\,. \tag{2.11}$$

Around the minimum $\varphi_{\min}$, the second derivative of the potential with respect to φ, i.e. the inductive energy of the ATS writes

$$\frac{\partial^2}{\partial\varphi^2}U(\varphi_{\min}, \epsilon, \delta) = E_L \mp 2\Delta E_J + E_L\varphi_{\min}^2 \pm 2E_J\epsilon\delta \mp \Delta E_J(\varphi_{\min}^2 - \epsilon^2 - \delta^2)\,. \tag{2.12}$$

The ATS inductive energy has no linear terms in ϵ or δ so the points $(\varphi_\Sigma, \varphi_\Delta) = (\pi/2, \pm\pi/2)$ are critical points of the inductive map of the ATS as a function of ϵ and δ. Its quadratic dependence around the critical point has the following matrix representation

$$M(E_L, E_J, \Delta E_J) = \frac{4(E_L \mp \Delta E_J)}{(E_L \mp 2\Delta E_J)^2}\begin{bmatrix} E_J^2 & E_J\Delta E_J \\ E_J\Delta E_J & \Delta E_J^2 \end{bmatrix} \pm \begin{bmatrix} \Delta E_J & E_J \\ E_J & \Delta E_J \end{bmatrix} \tag{2.13}$$

the determinant of which writes

$$\det(M) = E_L^2\frac{\Delta E_J^2 - E_J^2}{(E_L \mp 2\Delta E_J)^2}\,. \tag{2.14}$$

The determinant is negative (provided $\Delta E_J < E_J$) hence the critical point is a saddle point. This property is used to tune the DC working point experimentally (see Figure 2.6). When $\Delta E_J \neq 0$, the two points $(\varphi_\Sigma, \varphi_\Delta) = (\pi/2, \pm\pi/2)$ are non equivalent saddle points of the ATS with inductive energy $E_L \mp 2\Delta E_J$.
Since in the experiment we have $\Delta E_J/E_J \approx 0.5\%$ (see Table 2.1), we can neglect ΔE_J in the rest of the following analysis.

Choice of parameters In the process of choosing the ATS parameters, we were guided by the intuition that dynamical instabilities would be avoided in a system with $2E_J/E_L \lesssim 1$ [63, 67]. However, this criterion needs to be balanced with the requirement of large two-to-one photon

coupling rate g_2 (see equation (2.17)). In this experiment, we favoured stability over coupling strength and chose: $2E_J/E_L = 1.2$, a factor of 3.3 smaller than the previous implementation [59]. Moreover, we engineered a weak hybridization between the memory and buffer mode in order to minimize undesired nonlinear couplings such as the Kerr effect, with a rate estimated below 1 Hz.

1.5 From operating point to two-photon coupling

By flux pumping the ATS around a well chosen DC working point [59]

$$\begin{aligned} \varphi_\Sigma &= \frac{\pi}{2} + \epsilon_p \cos(\omega_p t) \\ \varphi_\Delta &= \frac{\pi}{2} \end{aligned} \tag{2.15}$$

we engineer a two-to-one photon exchange Hamiltonian between the memory and the buffer, provided the pump frequency ω_p is close to the matching condition $\omega_p = 2\omega_a - \omega_b$ and driving the buffer mode at $\omega_d = \omega_b$. This two-to-one photon exchange Hamiltonian converts the strong single photon losses of the buffer into an effective two-photon loss channel for the memory. Likewise, a microwave drive at frequency ω_d close to the buffer frequency, is converted into an effective two-photon drive of the memory (or squeezing) at frequency $(\omega_d+\omega_p)/2$. By definition, this frequency is close to the memory frequency.
For the memory, the combination of the two-photon loss and two-photon drive, stabilizes two coherent states with frequency $(\omega_p+\omega_d)/2$ of equal amplitude and opposite phase. The heterodyne demodulation frequency ω_{dm} for the memory is constrained accordingly

$$\omega_{\mathrm{dm}} = \frac{\omega_p + \omega_d}{2}\,. \tag{2.16}$$

By going in the frame rotating at frequency ω_{dm} for the memory and ω_d for the buffer and performing first order rotating wave approximation (RWA), the Hamiltonian (2.4) writes [59]

$$\begin{aligned} &H/\hbar = -\Delta_a a^\dagger a - \Delta_b b^\dagger b + g_2^* a^2 b^\dagger + g_2 {a^2}^\dagger b \\ &\text{with } \hbar g_2 = -\frac{1}{2} E_J \varepsilon_p \upsilon^2 \varphi_b^3 \end{aligned} \tag{2.17}$$

and where $\Delta_a = \omega_{\mathrm{dm}} - \omega_a$, $\Delta_b = \omega_d - \omega_b$, and ω_a and ω_b are respectively the memory and buffer frequency accounting for the AC-stark shift due to the pump [59]. Incorporating the buffer drive and the dissipation of the two modes, the dynamics of the system is governed by

$$\begin{aligned} H/\hbar = &-\Delta_a a^\dagger a - \Delta_b b^\dagger b \\ &+ g_2^* a^2 b^\dagger + g_2 {a^\dagger}^2 b - \epsilon_d b^\dagger - \epsilon_d^* b \\ L_a = &\sqrt{\kappa_a}\, a \\ L_b = &\sqrt{\kappa_b}\, b \end{aligned} \tag{2.18}$$

where ϵ_d is the buffer drive strength and κ_a and κ_b are the single photon loss rate of the memory and the buffer respectively.
We gain further insight on the dynamics of the system by performing the adiabatic elimination of the buffer. This is justified provided $g_2 \ll \kappa_b$. Following the method of [71], we find that the reduced dynamics of the memory is given by

$$\begin{aligned} H_a/\hbar &= -\Delta_a a^\dagger a + K_{\text{eff}}(a^2-\zeta^2)^\dagger(a^2-\zeta^2) \\ L_{a^2} &= \sqrt{\kappa_{2,\text{eff}}}(a^2-\zeta^2) \\ L_a &= \sqrt{\kappa_a}a \end{aligned} \tag{2.19}$$

with

$$K_{\text{eff}} = \kappa_2\eta\frac{\Delta_b}{\kappa_b}, \quad \kappa_{2,\text{eff}} = \kappa_2\eta, \quad \kappa_2 = \frac{4|g_2|^2}{\kappa_b}, \quad \zeta^2 = \frac{\epsilon_d}{g_2}, \quad \eta = \frac{1}{1+4\Delta_b^2/\kappa_b^2}\,. \tag{2.20}$$

Equivalently,

$$\begin{aligned} H_a/\hbar &= -\Delta_a a^\dagger a - \epsilon_d\gamma a^{\dagger 2} - \epsilon_d\gamma^* a^2 + \Delta_b|\gamma|^2 a^{\dagger 2}a^2 \\ L_{a^2} &= \sqrt{\kappa_b|\gamma|^2}a^2 \\ L_a &= \sqrt{\kappa_a}a \end{aligned} \tag{2.21}$$

with $\gamma = \frac{g_2}{\Delta_b + i\kappa_b/2}$. At $\Delta_a = \Delta_b = 0$, we recover eq. (2.1)

$$\begin{aligned} H_2/\hbar &= i\epsilon_2 a^{\dagger 2} - i\epsilon_2^* a^2 \\ L_2 &= \sqrt{\kappa_2}a^2 \\ L_1 &= \sqrt{\kappa_a}a \end{aligned} \tag{2.22}$$

with $\epsilon_2 = 2\epsilon_d g_2/\kappa_b$ and $\kappa_2 = 4|g_2|^2/\kappa_b$.

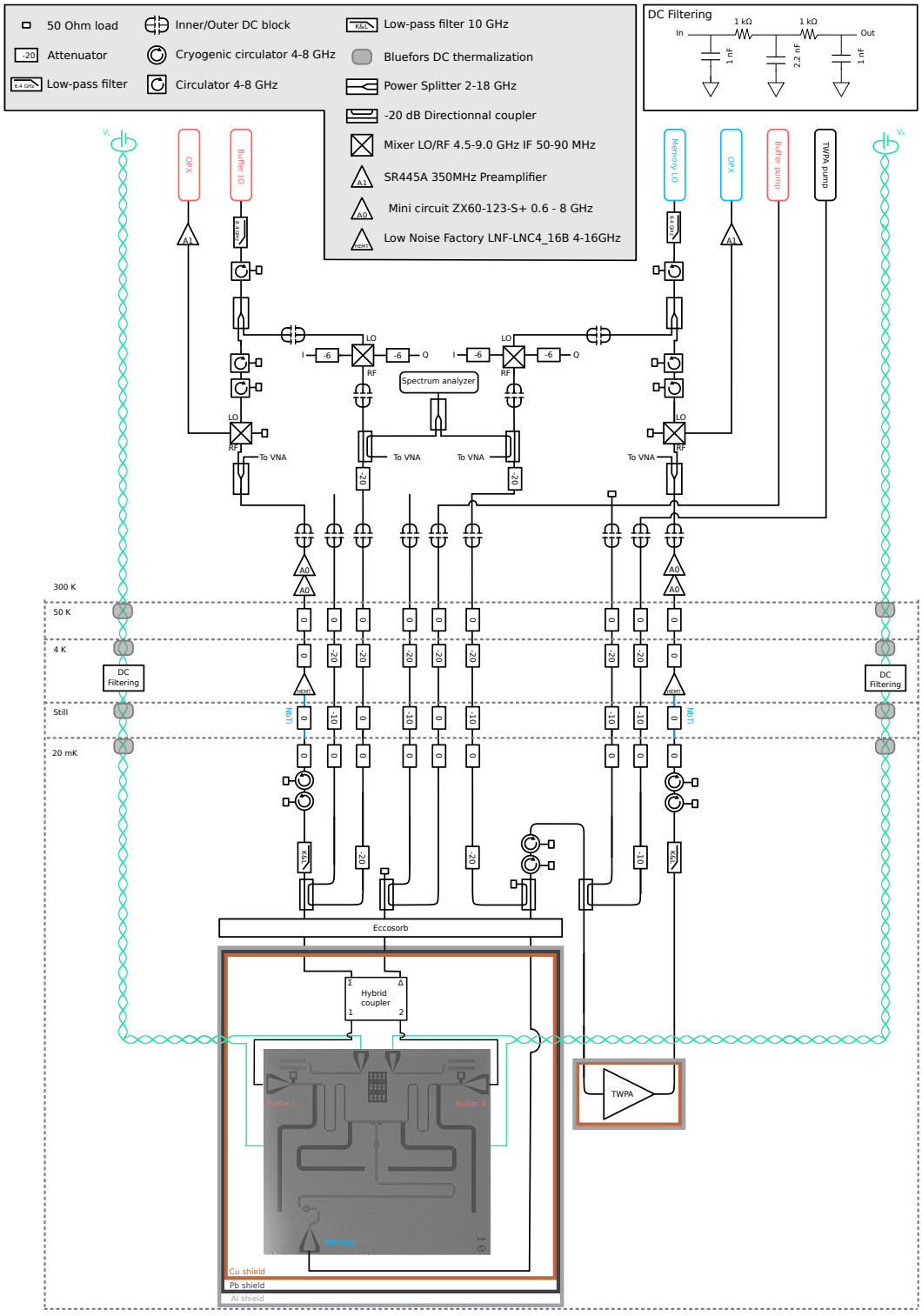

Figure 2.3: Wiring of the experiment. Measurement apparatus for the memory (blue labels), buffer (red labels), and TWPA pump (black label) connect to the experiment through RF lines (black lines). DC voltage sources are used to drive flux lines (green lines). Dashed lines indicate the different temperature stages of the dilution refrigerator. Additional information is provided in the legend (grey background), annotations and in the text.

2 Experiment calibration

The first step in conducting the experiment is to activate the two-photon conversion regime. For this, we have to calibrate the experiment to meet the conditions so that the total dynamics of the system is equivalent to a two-photon exchange dynamics for the memory, as explained in Subsection 1.5. The first condition is to DC bias in flux the ATS in order to reach the operating point $(\varphi_\Sigma, \varphi_\Delta) = (-\pi/2, \pi/2)$. The second condition is to reach the frequency matching conditions between the pump frequency, the memory mode frequency and the buffer drive frequency. Moreover, the buffer drive frequency has to be aligned with the buffer mode resonance frequency. The AC-Stark shift on the modes frequencies when turning on a strong pump complicates this matching condition. This section exposes the calibration procedure to finely align those frequencies.

2.1 DC calibration and extraction of circuit parameters

We start the experiment by measuring the buffer mode frequency map as a function of the two DC currents. Conveniently, the desired operating point $(\varphi_\Sigma, \varphi_\Delta) = (-\pi/2, \pi/2)$ is easily recognisable since it corresponds to a saddle point of this map. Consequently, the buffer and memory modes are first order insensitive to flux noise.
The first calibration experiment we perform is to extract the buffer and memory frequencies as a function of the common and differential flux in the ATS loop (see Figure 2.5). From these maps we identify the circuit parameters and locate the ATS saddle points.

Measurement protocol of frequency flux maps We set a tone at frequency f on the buffer port and record its reflected amplitude and phase as a function of the DC voltages $V_{\Sigma,\Delta} = (V_L \pm V_R)/2$ (see Figure 2.3). The physical controls $V_{\Sigma,\Delta}$ are transformed to the common and differential flux basis $\varphi_{\Sigma,\Delta}$ to match the symmetries of the circuit Hamiltonian of eq. (2.4). A variation in the reflected signal is detected at flux points $\varphi_{\Sigma,\Delta}(f)$ where the buffer frequency enters the vicinity of f. This sequence is repeated by scanning f in between 5.2 GHz and 9 GHz in steps of 100 MHz. Figure 2.4 presents maps at different frequencies values. In Figure 2.5, the frequency f is encoded in the color of pixels located at $\varphi_{\Sigma,\Delta}(f)$, so as to compile all the maps exposed in Figure 2.4.
We repeat the same protocol on the memory port to extract the memory frequency flux map.

Saddle points localization The theory plots in Fig. 2.5 are obtained for the numerical diagonalization of the Hamiltonian in eq. (2.4). From the ATS symmetries, we know that there exist two nonequivalent families of saddle points, those generated from $(\varphi_\Delta, \varphi_\Sigma) = (-\pi/2, \pi/2)$, and those from $(\varphi_\Delta, \varphi_\Sigma) = (\pi/2, \pi/2)$. The junction asymmetry ΔE_J lifts the degeneracy of the buffer frequency between these points.
We refine the flux and frequency sweeps around these saddle points in order to precisely pin down their location. In Figure 2.6, we directly display the reflected amplitude on the buffer port at different frequencies f. A saddle point is easily identified as the closing of the buffer

E_C/h	72.6 MHz
E_L/h	62.40 GHz
E_J/h	37.00 GHz
$\Delta E_J/h$	0.207 GHz
$\omega_{b,0}/2\pi$	6.020 GHz
φ_b	0.220
$\omega_{a,0}/2\pi$	4.0457 GHz
υ	3.6%

Table 2.1: Buffer and memory parameters entering the Hamiltonian (2.4). E_C and E_L are respectively the buffer's charging and inductive energy. E_J and ΔE_J are the ATS mean Josephson energy and asymmetry. $\omega_{b,0}/2\pi$ and $\omega_{a,0}/2\pi$ are buffer and memory bear frequencies. φ_b is the buffer zero point fluctuations. υ is the hybridization strength. From these numbers, we can estimate the Kerr nonlinearity of the memory $K_a < 1$ Hz.

frequency contour line. Note that the saddle point at $(-\pi/2, \pi/2)$ appears at $f_{b1} = 6.00$ GHz as shown in the top middle panel. The second one appears at $f_{b2} = 6.04$ GHz as shown in the bottom middle panel.

Extraction of parameters The parameters entering eq. (2.4) are listed in Table 2.1. The charging energy E_C is extracted from 3D finite elements electromagnetic simulations. The inductive energy E_L and the junction asymmetry ΔE_J are computed from the buffer frequencies at the saddle points that verify, in the weakly hybridized limit

$$f_{b1,b2} = \frac{1}{h}\sqrt{8E_C(E_L \pm 2\Delta E_J)}\,. \tag{2.23}$$

The Josephson energy E_J is extracted from the maximum buffer frequency $f_{b_{\max}}$ measured in the buffer flux map of Figure 2.5. This maximum value $f_{b_{\max}} = 8.9$ GHz is reached for $(\varphi_\Delta, \varphi_\Sigma) = (0, 0)$ and verifies, in the weakly hybridized limit: $f_{b_{\max}} = \frac{1}{h}\sqrt{8E_C(E_L + 2E_J)}$.
The memory frequency f_a is extracted from the memory frequency flux map in Figure 2.5 at the saddle points. Due to the weak hybridization with the buffer, the memory frequency difference at the two saddle points is negligible. Finally we numerically find the hybridization factor υ that produces a memory frequency flux map in agreement with the data in Figure 2.5.

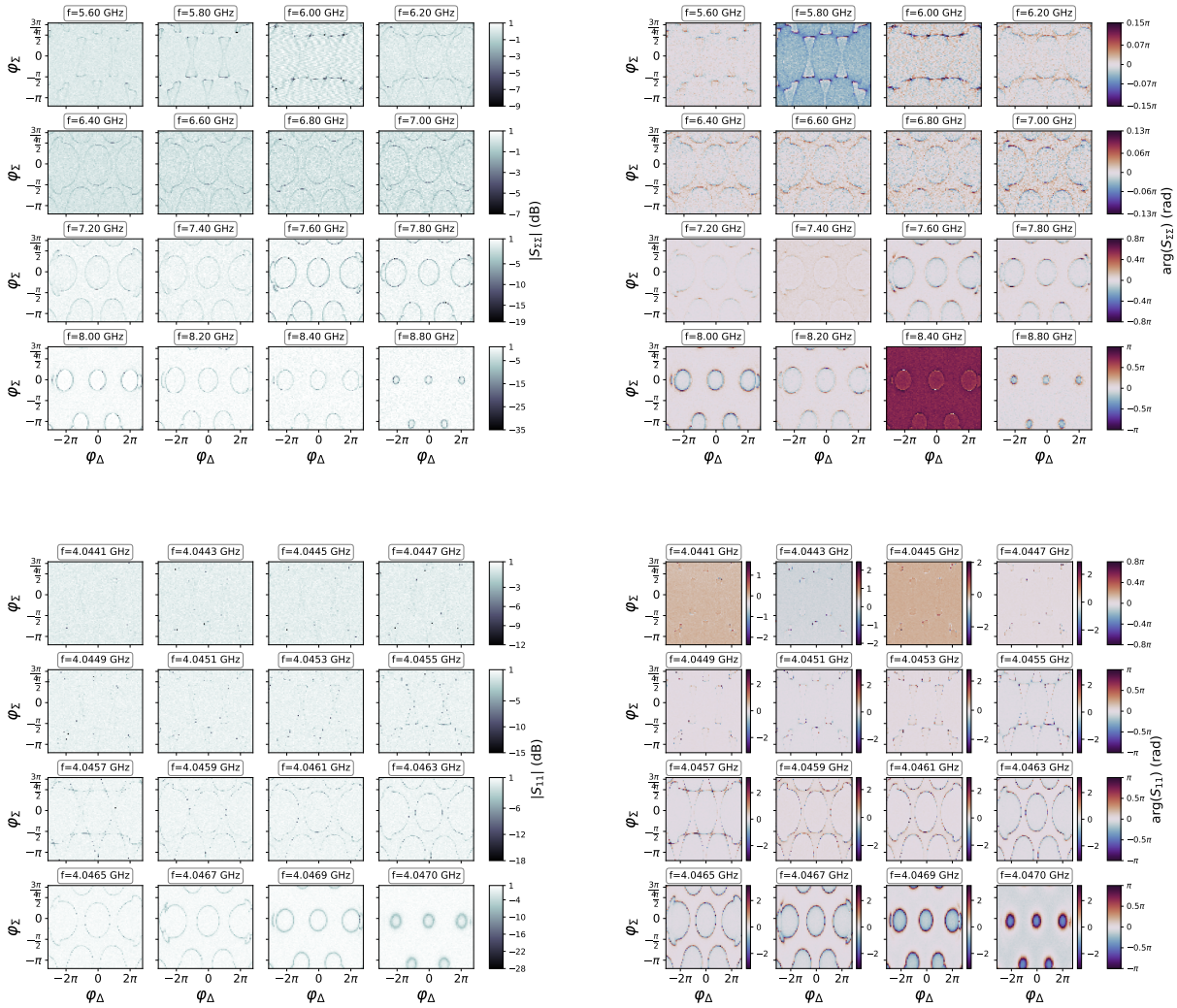

Figure 2.4: Flux maps of the buffer (top) and the memory (bottom) displayed with the measured relative amplitude (left plots) and phase (right plots) of the reflected signal of the buffer, respectively memory, port. Each panel encodes in the color scale the measured relative amplitude, respectively phase, of the signal sent at the frequency f (specified in each label box) as a function of the differential (x-axis) and common (y-axis) flux biases.

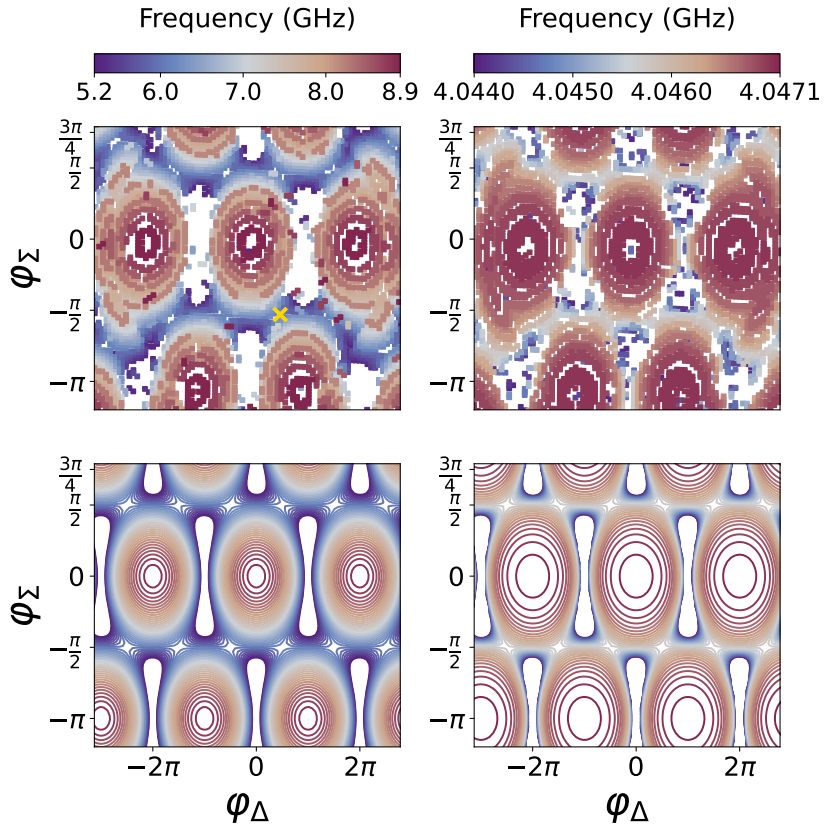

Figure 2.5: Measured (top) and simulated (bottom) frequencies (color) of the buffer (left) and memory (right) as a function of the differential flux (x-axis) and common flux (y-axis) in the ATS loop. The orange cross marks the flux point at which we operate the experiment.

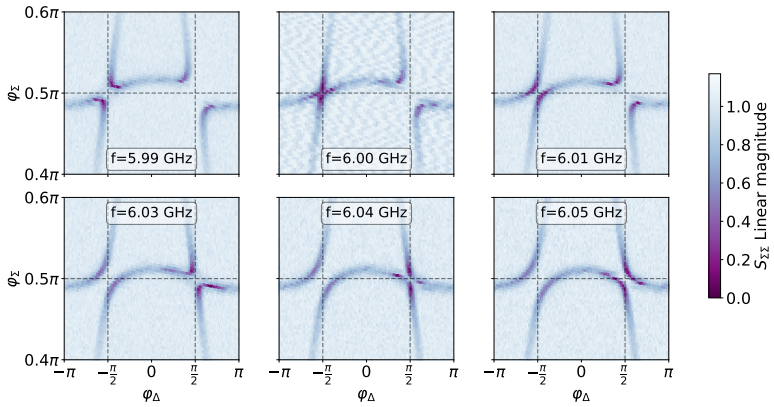

Figure 2.6: Each panel displays the measured relative amplitude (color) of the reflected signal on the buffer port at the frequency f specified in each label box, as a function of the differential (x-axis) and common (y-axis) phase biases. The dashed grey lines are guides for the eye corresponding to $\varphi_\Delta = \pm\pi/2$ and $\varphi_\Sigma = \pi/2$.

2.2 Turning on RF pumping

Once the DC biases are tuned at one saddle point and the memory and buffer resonance frequencies are determined by direct spectroscopy in reflection on their respective ports, we turn on the RF pump and the buffer drive.

Phase locking In the following paragraphs, we are going to study the energy radiated out from the memory while driving and pumping the buffer to activate the two-photon conversion. In this process, the frequencies of the waves in the buffer and the memory channels are connected with the phase matching condition. Therefore, in order to observe two-photon pumping, there is a phase locking requirement to meet in the measurement channels of the buffer and memory. In the laboratory frame, at any point in time, the phase of the pointer states resulting from the junction mixing process is given by

$$\theta_a = (\theta_p + \theta_d)/2 \tag{2.24}$$

where θ_p and θ_d are respectively the pump and drive tone phase. The pump tone is directly generated by the microwave signal generator and pulsed via a microwave switch whereas the drive tone is pulsed via an IQ-mixer (Figure 2.3).The resulting phases of the tones are

$$\theta_p = \theta_p^{LO}, \quad \theta_d = \theta_d^{LO} + \theta_d^{IF} \tag{2.25}$$

where θ_p^{LO} and θ_d^{LO} are the Local Oscillator (LO) phases of the microwave generator and θ_d^{IF} is the Intermediate Frequency (IF) signal phase delivered by the Arbitrary Waveform Generator (AWG) channel to pulse the drive tone. The radiated signal from the memory is demodulated in a frame with phase

$$\theta_{dm} = \theta_{dm}^{LO} + \theta_{dm}^{IF} \tag{2.26}$$

where θ_{dm}^{LO} is the phase of the demodulation LO and θ_{dm}^{IF} is the phase of the Analog-Digital Converter (ADC). In order to phase-lock the pointer states with the demodulation frame, we should ensure

$$\theta_a - \theta_{dm} = \text{cst}\,. \tag{2.27}$$

The three LOs are generated with a single four channel Anapico signal generators, and the two IFs with a single Quantum Machines OPX. The accuracy of these instruments ensure that all the LOs share the same time reference and all the IFs share the same time reference. However, given the high frequencies at stake, the instruments sharing the same 50 MHz clock is not sufficient for this two time references to be considered identical. The LO time is referred to as t and the IF time as t'. Hence

$$\begin{aligned} \theta_a - \theta_{dm} &= (\omega_p^{LO} t + \omega_d^{LO} t + \omega_d^{IF} t')/2 + \text{cst} \quad - (\omega_{dm}^{LO} t + \omega_{dm}^{IF} t') + \text{cst} \\ &= ((\omega_p^{LO} + \omega_d^{LO})/2 - \omega_{dm}^{LO}) t \quad + (\omega_d^{IF}/2 - \omega_{dm}^{IF}) t'\,. \end{aligned} \tag{2.28}$$

and the phase-locking condition imposes the frequency matching conditions

$$\begin{aligned}(\omega_p^{LO} + \omega_d^{LO})/2 - \omega_{dm}^{LO} &= 0 \\ \omega_d^{IF}/2 - \omega_{dm}^{IF} &= 0\,.\end{aligned} \tag{2.29}$$

Wave mixing processes The ATS is a nonlinear wave mixing component. We can then activate different wave mixing processes by turning on the RF pump at sufficiently large amplitudes. While scanning the pump frequency and the buffer drive frequency for spectroscopy, we can recognize nonlinear processes signatures in Figure 2.7. We can identify each wave mixing process with some arithmetic combination of pump frequency, noted ω_p, buffer drive frequency, ω_d, memory mode frequency, ω_a, and second harmonic of the memory mode, noted ω_{2a} (see Figure 2.7).
We are interested in the two-photon conversion process which involves two photons of memory mode ω_a (that is to say of total energy: $2\hbar\omega_a$). However, the second harmonic of the memory mode ω_{2a} is by definition such as: $\omega_{2a} \approx 2 \times \omega_a$. Thus, as shown in Figure 2.7, some conversion processes involving second harmonic of memory mode are close to the two-photon conversion process. In order to isolate this specific two-photon process, the next generation of two-photon dissipative oscillator circuits will have a cavity mode with a different value of the second harmonic frequency. This can be accomplished by replacing the $\lambda/2$ resonator implementing the memory in the current circuit with a $\lambda/4$ resonator. In this case, the second harmonic of memory will be at $\omega_{2a} \approx 3\omega_a$, avoiding the confusion.

2.3 Finely tuning pump and drive frequencies

In the presence of this strong pump, the modes' frequencies are Stark shifted. Therefore, a precise calibration of the pump frequency $\omega_p/2\pi$ and drive frequency $\omega_d/2\pi$ is required to rigorously verify the frequency matching conditions: $\omega_p = 2\omega_a - \omega_d$ (two-photon conversion) $\omega_d = \omega_b$ (driving the buffer at its resonance frequency).

Method for tuning the pump frequency We pick the largest pump power that does not deteriorate the buffer and memory modes spectra. We acquire the memory mode fluorescence as a function of detunings from these matching conditions. The pump frequency is determined via two-tone spectroscopy: a weak drive tone is used to perform buffer spectroscopy while sweeping the pump frequency around the frequency matching condition. As this operation is being performed, we also perform the heterodyne detection of the field radiated by the memory (Figure 2.8). As the drive amplitude ϵ_d is increased, the region over which the drive and pump combine to populate the memory expands around the frequency matching point as it is clearly visible in the different diagrams of Figure 2.9 and in Figure 2.12 (a).
When the two-to-one photon exchange is resonant, a sharp feature is observed within buffer resonance, referred to as a diamond, and the memory starts to radiate power. The discrepancy between the ideal and measured diamond shape is used as a witness for the appearance of higher order processes. The pump amplitude is set so as to maximize the two-to-one photon coupling

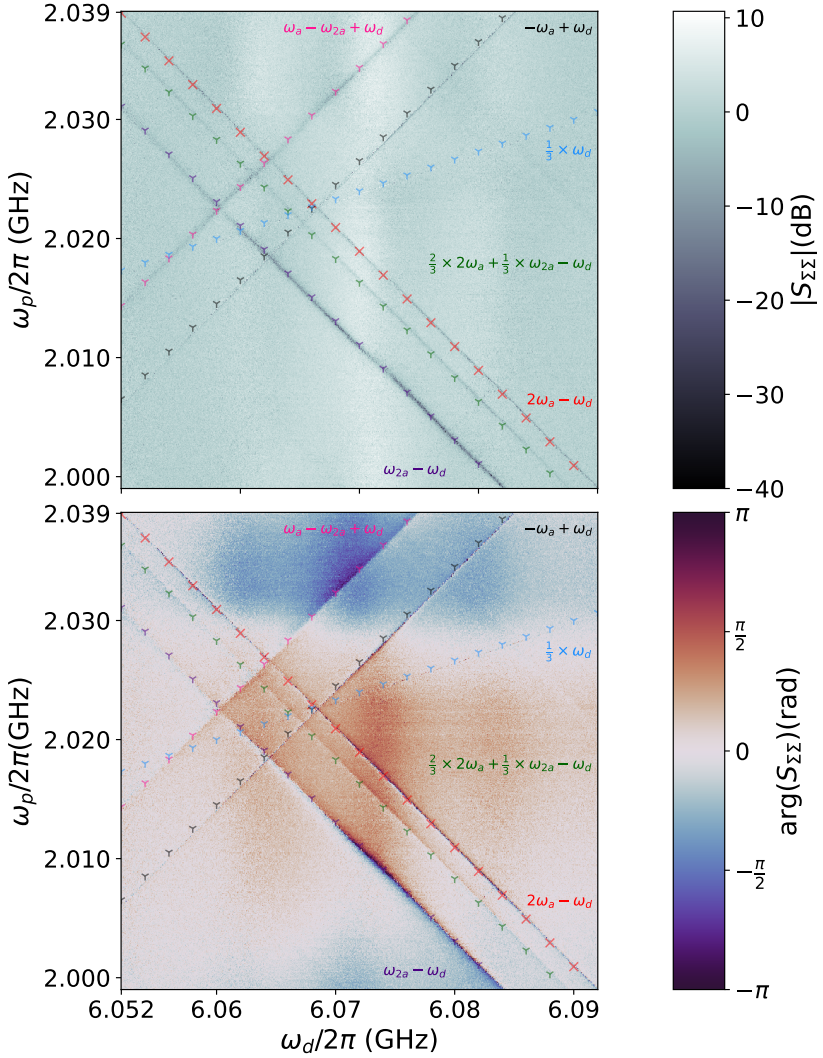

Figure 2.7: Measured relative amplitude (top, color scale represents amplitude) and phase (bottom, color scale represents phase) of the reflected signal on the buffer as a function of the drive frequency $\omega_d/2\pi$ (x-axis) and the pump frequency $\omega_p/2\pi$ (y-axis). We observe a dip in amplitude and a phase shift in the reflected signal for some combinations of the pump and the buffer drive frequencies. This means that some conversion processes is activated in the buffer mode. We have highlighted those processes with coloured crosses. For clarity, the line equations are indicated next to each line. They are frequency matching conditions between the pump frequency $\omega_p/2\pi$, the buffer drive frequency $\omega_d/2\pi$, the memory first harmonic mode $\omega_a/2\pi = 4.045$GHz and the memory second harmonic mode $\omega_{2a}/2\pi = 8.083$GHz. The red 4-line crosses highlight the two-photon conversion process at the core of the device: $\omega_p = -\omega_d + 2\omega_a$. The 3-line crosses indicate other nonlinear processes: $\omega_p = \omega_{2a} - \omega_d$ (purple), $\omega_p = \omega_d - \omega_a$ (grey), $\omega_p = \omega_d + \omega_a - \omega_{2a}$ (pink), $\omega_p = \omega_d \times \frac{1}{3}$ (light blue), $\omega_p = -\omega_d + 2\omega_a \times \frac{2}{3} + \omega_{2a} \times \frac{1}{3}$ (green, this last process is a high order process so it could derive from another frequencies combination). This picture's data was collected during a different cooldown than the experiment's main cooldown.

rate g_2 while mitigating detrimental higher order effects.

Process for data acquisition In order to minimize the amount of data collected and accurately zoom on the diamond feature Figure 2.8a is acquired in the following way:

- at a fixed pump frequency the buffer spectroscopy is done by varying the buffer IF frequency (x-axis of Figure 2.8a) with a fixed LO frequency. Due to the frequency constraint of eq. (2.29) the heterodyne detection of the radiated memory field is done by varying the memory IF frequency with a fixed LO frequency.
- for the demodulation frequency to remain close to the memory frequency while varying the pump frequency, (y-axis of Figure 2.8a) the pump and drive LO frequencies are varied in opposite directions. In this way, we have $\omega_p + \omega_b^{LO} = 2\omega_{dm}^{LO} = \text{cst}$.

Change of coordinates We recall that Δ_a, respectively Δ_b, are the detuning between memory, respectively buffer, resonant frequency and their respective drives. In the coordinates of Figure 2.8a (buffer IF frequency for x-axis, pump frequency for y-axis), Δ_b and $2\Delta_a$ are thus varied along the x-axis and Δ_b is varied along the y-axis. If there was no Stark shift, the buffer resonance would be a diagonal line of slope 1 and the memory line (when the two-photon drive is tuned with the memory mode) a vertical line. In practice, these two lines are distorted and we numerically fit the buffer and memory frequencies as a function of the pump frequency to perform the change of basis leading to the diamond of Figure 2.8d in the Δ_a, Δ_b coordinate system.
To perform this change of coordinates, we evaluate the following functions from measurements by linear interpolation

$$\begin{aligned} \Delta_b &= f(\omega_d^{IF}, \omega_p) = \omega_d^{IF} + \omega_d^{LO} - \omega_b[\omega_p] \\ \Delta_a &= g(\omega_d^{IF}, \omega_p) = \frac{\omega_b^{IF}}{2} + \frac{\omega_p + \omega_d^{LO}}{2} - \omega_a[\omega_p] = \omega_{dm}^{IF} + \omega_{dm}^{LO} - \omega_a[\omega_p]\,. \end{aligned} \tag{2.30}$$

For each data point, we can now compute the actual value of Δ_a and Δ_b. This enables us to display radiated energy by the memory in the basis of Hamiltonian eq. (2.18): previously distorted, the diamonds recover their shape.

Center of the diamonds By construction, the diamond center should coincide with the zero detuning point. By exploiting the diamonds inversion symmetry, we can verify that the maximum of the auto-correlation function

$$(\Delta_a^0, \Delta_b^0) = \max_{(\Delta_a, \Delta_b)} \left(\iint |\alpha|^2(\delta_a, \delta_b) |\alpha|^2(\Delta_a - \delta_a, \Delta_b - \delta_b) \delta_a \delta_b \right) \tag{2.31}$$

gives back the zero detuning point, up to a slight discrepancy due to the diamond imperfection. Experimentally, we find the zero detuning point as the convergence point of the diamond feature at vanishingly small drive amplitude (see Figure 2.8c). All three centers (construction, auto-correlation, experimental) are shown in Figure 2.9 and lie in a small region at the center of

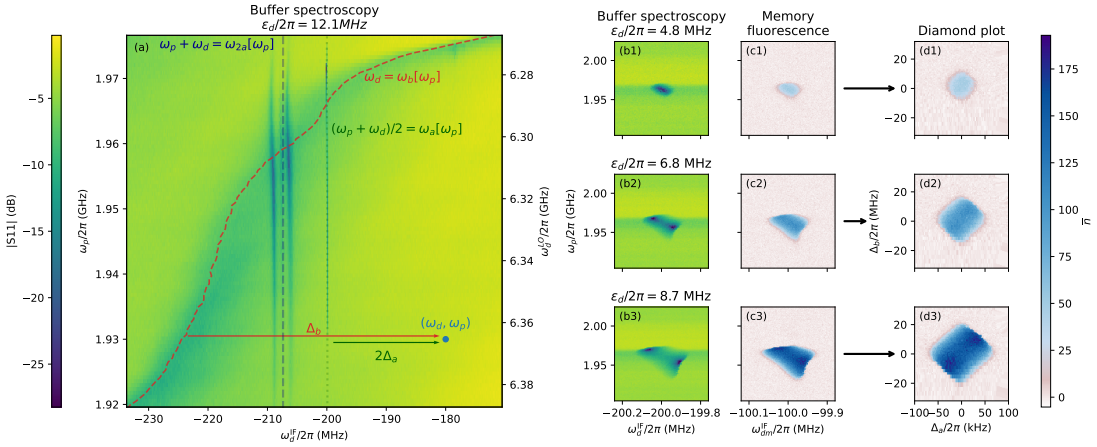

Figure 2.8: (**a**) Relative amplitude (color) of the reflected signal on the buffer port as a function of the pump frequency ω_p (left y-axis), drive local oscillator (LO) frequency ω_d^{LO} (right y-axis) and drive intermediate frequency ω_d^{IF} (x-axis). The drive frequency is given by $\omega_d = \omega_d^{\mathrm{IF}} + \omega_d^{\mathrm{LO}}$. For each pump frequency, the drive LO frequency is set to $\omega_d^{\mathrm{LO}} = (2\omega_a - \omega_p) + 200$ MHz, such that vertical lines correspond to constant detuning from the frequency matching condition ($\Delta_a = \mathrm{cst}$). The buffer drive resonance condition $\Delta_b = 0$ is determined by fitting each horizontal cuts of the map (dashed red line). In the vicinity of $\Delta_a = 0$ and $\Delta_b = 0$, a sharp feature indicates that the two-to-one photon exchange transition is resonant (dotted green line). Spurious transitions appear near the frequency matching condition $\omega_p + \omega_d = \omega_{2a}$ (blue dashed line), where ω_{2a} is the frequency of the second harmonic of the memory $\lambda/2$-resonator measured independently. (**b**) Zoom on the two-to-one photon exchange transition for increasing drive amplitude ϵ_d. (**c**) Radiated energy from the memory in units of circulating photon number (color) as a function the pump frequency ω_p (left y-axis) and two-photon drive intermediate frequency $\omega_{dm}^{\mathrm{IF}}$ (x-axis), for increasing drive amplitude. On these panels, the two-photon drive LO frequency is set to $\omega_{dm}^{\mathrm{LO}} = \omega_a + 100$ MHz. When the two-to-one photon exchange transition is resonant, the engineered two-photon drive populates the memory. The average occupation of the memory is determined thanks to an undercoupled port via heterodyne detection. (**d**) Radiated energy from the memory in units of circulating photon number (color) as a function of the pump and drive detuning from the frequency matching condition Δ_a (x-axis), and the drive detuning from the buffer Δ_b (y-axis). In these coordinates, the feature takes the shape of a regular diamond.

the diamond. For the remaining of the experiment, we place ourselves at the center of these diamonds.

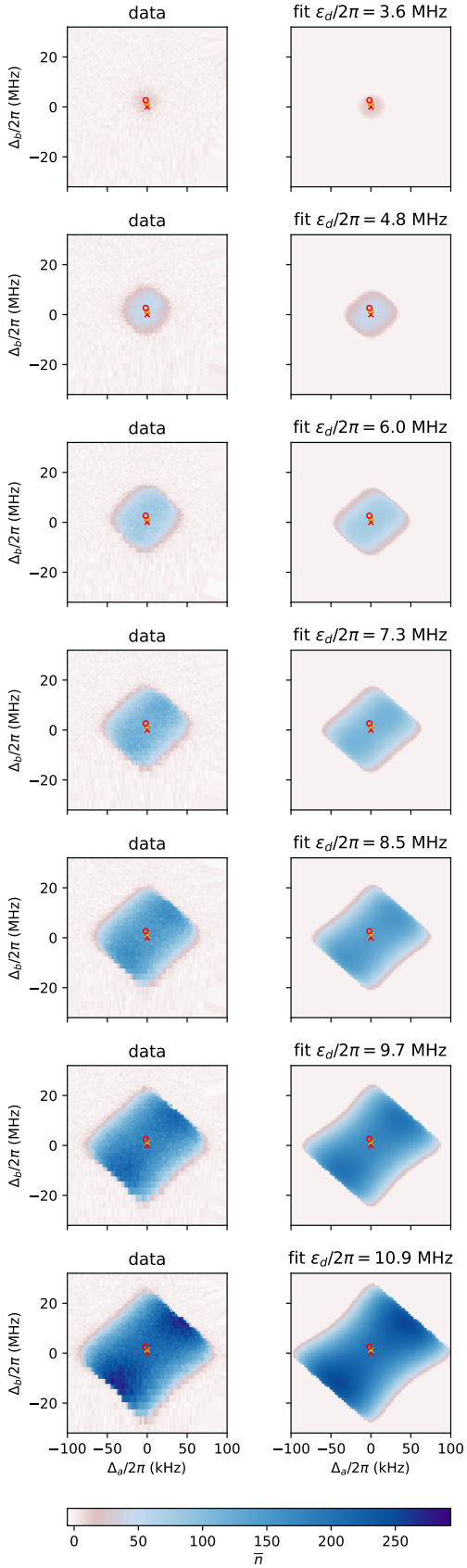

Figure 2.9: Radiated energy from the memory in units of circulating photon number (color) as a function of the detuning from the frequency matching condition Δ_a (x-axis), and the detuning from the buffer resonance Δ_b (y-axis). Left column displays data, right column displays semi-classical simulations for the corresponding drive amplitude. Orange cross shows the position of the maximum of the auto-correlation for the largest drive amplitude. Red cross shows the zero detuning point given by direct fit of memory and buffer spectroscopy. Red circle is the point at which well averaged data were taken to perform the fit of g_2.

3 Photon number calibration

Two-photon pumping activation leads to the creation of coherent states in the memory, as explained in Section 1. Our goal is to measure the macroscopic lifetime of these states. Nonetheless, it is critical to observe these macroscopic bit-flip times for states containing only a few tens of photons. As a matter of fact, this system can only function as a coherent qubit in the low photon number regime. Therefore, a reliable calibration of the number of photons, noted $\bar{n}$, is essential to this work. However, contrary to the circuit of [59], we have entirely removed the tomography apparatus for the memory in order to avoid ancillary systems propagating uncorrectable errors. Instead, we use a travelling wave parametric amplifier (TWPA) to directly measure the field radiated by the memory. As a result, there is no direct photon number scaling for the radiated energy collected out from the memory. This section is dedicated to the photon number calibration procedure of this experiment.
To begin, we compute the mapping between the cavity field properties and the measured quadratures. Then, to calibrate $\bar{n}$, we investigate the emergence in the memory of two meta-stable pointer states from a nonlinear dissipative phase transition. Finally, the measurement of the quantum detection efficiency performed in Chapter 3 corroborates this calibration.

3.1 Heterodyne detection

We want to measure the radiated field out of the memory: more precisely we want to measure $\overline{I^2+Q^2}$ where I and Q are the in-phase and out-of-phase quadratures of the radiated field acquired over an integration time T_m. This subsection details the procedure to perform this heterodyne detection.
The heterodyne detection of the field radiated by the memory results in two signals that are integrated over a integration time T_m to give out (I,Q) pairs time traces

$$\begin{aligned} I_t &= \sqrt{G}\int_t^{t+T_m}\left(\sqrt{2\kappa_a^c\eta}\mathrm{Tr}\left(\rho_{t'}(a+a^\dagger)/2\right)\mathrm{d}t' + \mathrm{d}W_I\right) \\ Q_t &= \sqrt{G}\int_t^{t+T_m}\left(\sqrt{2\kappa_a^c\eta}\mathrm{Tr}\left(\rho_{t'}(a-a^\dagger)/2i\right)\mathrm{d}t' + \mathrm{d}W_Q\right), \end{aligned} \tag{2.32}$$

where G is the gain of the amplification chain, κ_a^c is the coupling rate of the memory, η is the quantum detection efficiency, ρ_t is the instantaneous state and $\mathrm{d}W_I$, $\mathrm{d}W_Q$ are the noises added to each quadrature that verify $\mathrm{d}W_I^2 = \mathrm{d}W_Q^2 = \mathrm{d}t$. The statistics of the distribution of the (I,Q) pairs collected over time gives information about the memory state. In particular, we can verify that in the general case [72, 73] and in the limit of small T_m

$$\overline{I^2+Q^2} = 2GT_m + 2G\kappa_a^c\eta T_m^2\mathrm{Tr}(\rho_\infty a^\dagger a) = 2GT_m + 2G\kappa_a^c\eta T_m^2\bar{n} \tag{2.33}$$

where $\bar{n}$ is the mean photon number, $\overline{I^2+Q^2}$ is the statistical average over the (I,Q) pairs collected over time and ρ_∞ is the steady-state density operator of the cavity. In our specific case, we have verified both numerically and experimentally that this limit is practically reached for $T_m = 10$ µs. In eq. (2.33), the offset GT_m can be calibrated out from the average of $\overline{I^2+Q^2}$

when the cavity is in vacuum which results in the average energy radiated by the cavity over a period T_m of

$$\overline{I^2+Q^2} - \overline{I^2+Q^2}\Big|_{\text{vac}} = 2G\kappa_a^c \eta T_m^2 \bar{n}\,. \tag{2.34}$$

3.2 Steady state photon number

In this subsection we derive the stationary mean photon number in the memory using a semi-classical approximation. This will be useful in order to calibrate the acquired quadrature in the stationary state.

In the interaction picture, the dynamics arising from (2.18), writes

$$\begin{aligned} \frac{da}{dt} &= \left(i\Delta_a - \frac{\kappa_a}{2}\right) a - 2ig_2 a^\dagger b \\ \frac{db}{dt} &= \left(i\Delta_b - \frac{\kappa_b}{2}\right) b - ig_2^* a^2 + i\epsilon_d\,. \end{aligned} \tag{2.35}$$

We perform a mean-field approximation on mode a and b, and compute the steady-state of the simplified dynamics. The operators a and b are replaced by their mean value, the complex numbers α and β. This system always admits a solution in which the memory is in vacuum and corresponds to

$$\begin{aligned} \alpha &= 0 \\ \beta &= \frac{-\epsilon_d}{\Delta_b + i\kappa_b/2}\,. \end{aligned} \tag{2.36}$$

This solution is stable provided it is the only solution of eq. (2.35) for a given set parameters. Assuming $\alpha \neq 0$, we can write

$$\begin{aligned} i\frac{\kappa_a}{2} + \Delta_a &= 2g_2\beta e^{-2i\theta_a} \\ \left(i\frac{\kappa_b}{2} + \Delta_b\right)\beta &= g_2^*\alpha^2 - \epsilon_d \end{aligned} \tag{2.37}$$

where $\theta_a = \arg(\alpha)$.

Solving for β in the first equation and injecting in the second one, we get

$$\begin{aligned} |\alpha|^2 &= \frac{\epsilon_d}{g_2^*} e^{-2i\theta_a} + z \\ \text{with} \quad z &= \frac{(i\kappa_a/2 + \Delta_a)(i\kappa_b/2 + \Delta_b)}{2|g_2|^2}\,. \end{aligned} \tag{2.38}$$

Zero-detuning When $\Delta_a = \Delta_b = 0$, eq. (2.38) simplifies into

$$|\alpha|^2 = \frac{\epsilon_d}{g_2^*} e^{-2i\theta_a} - \frac{\kappa_a\kappa_b}{8|g_2|^2}\,. \tag{2.39}$$

leading to

$$|\alpha|^2 = \max\left[\left|\frac{\epsilon_d}{g_2^*}\right| - \frac{\kappa_a\kappa_b}{8|g_2|^2}, 0\right] = \max\left[\left|\frac{\epsilon_d}{g_2^*}\right|\left(1 - \frac{\kappa_a}{4|\epsilon_2|}\right), 0\right]\,. \tag{2.40}$$

We recover the critical point when the two-photon drive overcomes the cavity dissipation.
In the absence of calibrated input or output lines, the power radiated by the memory is defined up to a constant, in particular the quantity $|g_2\alpha|^2$ writes

$$|g_2\alpha|^2 = \max\left[|\epsilon_d g_2| - \frac{\kappa_a\kappa_b}{8}, 0\right] \tag{2.41}$$

which, as a function of $\epsilon_d g_2$, has a slope 1 and an x-intercept $\kappa_a\kappa_b/8$.
In terms of the single mode effective quantities, eq. (2.40) rewrites for $\epsilon_2 \geq \kappa_a/4$

$$|\alpha|^2 = \frac{1}{2\kappa_2}(4\epsilon_2 - \kappa_a) \qquad \text{(two-photon dissipation)}\ .$$

If instead of two-photon dissipation, Kerr effect of amplitude K_a was limiting the amplitude of the pointer states [53, 74], a similar semi-classical analysis predicts a mean photon number for $\epsilon_2 \geq \kappa_a/4$

$$|\alpha|^2 = \frac{1}{2K_a}\sqrt{(4\epsilon_2)^2 - (\kappa_a)^2} \qquad \text{(dissipative Kerr)}\ ,$$

which is qualitatively different from what is observed in this experiment.

General case Since θ_a and α are on separate sides of eq. (2.38), we can geometrically solve the system in the complex plane. The right-hand side is a circle of radius $|\epsilon_d/g_2^*|$ centered on z. The left-hand side is the positive real axis. In this picture, there can be 0, 1, or 2 intersections between this circle and the real positive axis, giving rise to 1, 3 or 5 solutions for the system, one for vacuum plus two for each intersection since $\pm\alpha$ are both valid solutions. Experimentally observed solutions are the ones that give rise to the largest field in the memory. Hence $|\alpha|^2$, the mean photon number in steady-state, writes

$$|\alpha|^2 = \begin{cases} \max\left[\mathrm{Re}(z) + \sqrt{\left|\frac{\epsilon_d}{g_2^*}\right|^2 - \mathrm{Im}(z)^2}, 0\right], & \text{if } \left|\frac{\epsilon_d}{g_2^*}\right|^2 > \mathrm{Im}(z)^2 \\ 0\,, & \text{otherwise.} \end{cases} \tag{2.42}$$

In the Δ_a, Δ_b coordinates, the region where α^2 is non-zero forms a diamond shape. Hereafter, we provide the equation for the borders of this feature colloquially referred to as a diamond. The Δ_a, Δ_b-plane is divided in two domains depending on the sign of the quantity $\Delta_a\Delta_b - \kappa_a\kappa_b/4$.
The top-right and bottom-left edges of the diamonds are located in the positive domain and are given by

$$\kappa_a\Delta_b + \kappa_b\Delta_a = \pm 4|\epsilon_d g_2|\,. \tag{2.43}$$

Note that the slope of this edge is determined by $-\kappa_b/\kappa_a$. The bottom-right and top-left edges are located in the negative domain and are defined by

$$\left(\frac{\kappa_a^2}{4} + \Delta_a^2\right)\left(\frac{\kappa_b^2}{4} + \Delta_b^2\right) = |2\epsilon_d g_2|^2\,. \tag{2.44}$$

Hence the border of the diamond only depends on the product $\epsilon_d g_2$ and does not carry information on g_2 nor ϵ_d independently. Moreover, we cannot determine g_2 and ϵ_d even with the full diamond information (not only the edges). Indeed, from the measurement of the rates κ_a, κ_b and the knowledge of the applied detunings Δ_a, Δ_b, one has independently access to the quantity

$$z' = \frac{1}{2}(i\frac{\kappa_a}{2} + \Delta_a)(i\frac{\kappa_b}{2} + \Delta_b)\,. \tag{2.45}$$

In the absence of photon number calibration, we only learn from eq. (2.42) that the power radiated by the memory is proportional to

$$\langle I^2 \rangle \propto \mathrm{Re}(z') + \sqrt{|\epsilon_d g_2|^2 - \mathrm{Im}(z')^2}\,. \tag{2.46}$$

Thus, we only have access to the product $\epsilon_d g_2$ but not g_2 or ϵ_d independently.

Discussion On the one hand, the top-right and bottom-left edges of the diamond are straight lines along which the photon number reaches its maximum value and suddenly drops to zero (see Figure 2.9) when increasing the detunings. One the other hand, the top-left and bottom-right edges have smoothly vanishing photon number when increasing the detunings. Hence, when increasing Δ_a at finite $\Delta_b > 0$, the photon number increases smoothly when $\Delta_a < 0$ and abruptly goes to zero at the $\Delta_a > 0$ edge. This qualitative behaviour is reminiscent from the response of a nonlinear parametric oscillator, whose dynamics is encoded in eq. (2.21).

3.3 Description of calibration steps

For various values of buffer drive amplitude ϵ_d, we measure the average energy radiated by the memory for a duration $T_m = 10$ µs which is proportional to $\bar{n}$ (see Figure 2.10 and Figure 2.12 (b)). The following paragraphs will attempt to calibrate this proportionality constant. The dependency of $\overline{I^2 + Q^2}$ as function of drive amplitude ϵ_d has some notable features. First, using semi-classical analysis, we can calibrate the axes so that the only unknown parameter is g_2. Then, a full quantum model is required to capture the curvature of this dependency, from which we extract the g_2 parameter.

3.3.1 Semi-classical analysis

Linear scaling for radiated energy as function of drive amplitude First, as presented in Figure 2.10 and in Figure 2.12 (b), in the limit of strong drives, the radiated energy scales linearly with the drive amplitude, a signature of the conversion of 1 buffer photon to 2 memory photons. This is in stark contrast with the common quadratic scaling for a driven harmonic oscillator. Moreover, the offset of this asymptote from the origin, that is consistent with the theoretical analysis of the previous subsection (see Subsection 3.2), excludes the Kerr effect as the underlying process.

Critical point: nonlinear phase transition The output power is close to zero up until a critical drive amplitude, reminiscent of a nonlinear dissipative phase transition [75]. This

transition occurs when the two-photon injection rate overcomes the memory losses, setting the scale for the product $\epsilon_d g_2$ to its value at the critical point $\epsilon_d g_2 = \kappa_a \kappa_b / 8$. This critical point clearly appears in equation (2.40). Using these properties, we calibrate the drive amplitude axis of Figure 2.10 in units of $|\epsilon_d g_2|$: the x-intercept of the linear dependence at large photon number (semi-classical regime) is located at $\kappa_a \kappa_b / 8$. The x-axis being calibrated, we linearly stretch the y-axis such that the asymptotic slope is 1 in the strong drive regime. According to semi-classical computation of steady state photon number of the previous subsection (eq. (2.41)), this transformation enforces the y-axis to $|\alpha g_2|^2$ and leads to the scaled data of Figure 2.10.

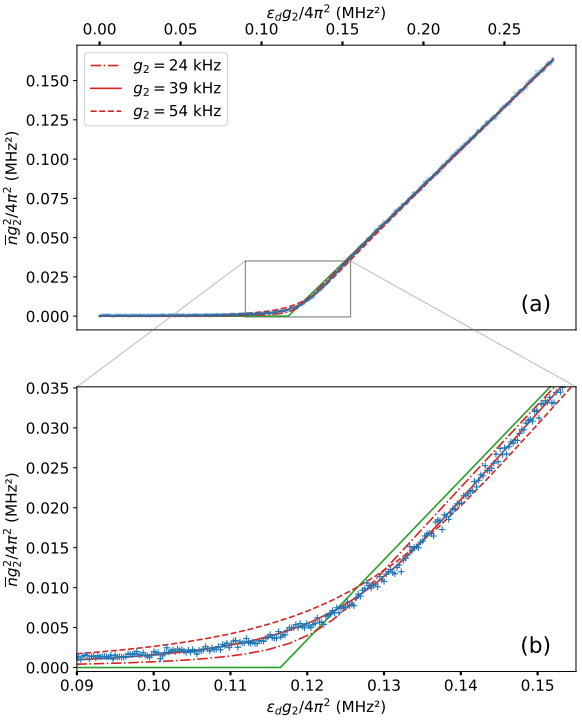

Figure 2.10: Two-photon coupling calibration. (a) Radiated energy from the memory (y-axis) as a function of drive amplitude (x-axis). There are two regimes: when the drive amplitude is small, single photon losses overcome the two-photon drive, and the memory stays in the vacuum. Once the critical point has been reached, the memory gets populated by a coherent state with photon number asymptotically proportional to the drive amplitude. The axes units are chosen so that the critical point is at $\kappa_a \kappa_b / 8$ and the asymptotic slope is 1. The data correspond to an integration time of 10 µs with 10000 averages (crosses). The semi-classical model (green solid line) captures the position of the critical point but fails to explain the curvature of the experimental data. A full numerical simulation is used to reproduce the data where the only fitting parameter is g_2 (red lines). (b) Zoom in on the curvature around the critical point (grey rectangle from (a)), emphasizing the agreement between simulations and experimental data.

Determination of κ_a and κ_b values This rescaling crucially depends on the values of κ_a and κ_b which are determined as follows. We measure the reflection coefficient of the memory in the presence of a pump tone slightly detuned from the frequency matching condition. This enables

to capture the shift of parameters (frequency, internal losses, coupling losses) due to nonlinear effects arising from the pump while disabling the two-photon losses. From this measurement we numerically fit $\kappa_a^i/2\pi \in [15, 22]$ kHz and $\kappa_a^c/2\pi \in [39, 42]$ kHz. The same protocol fails to determine precisely κ_b due to the background induced by the stop-band filters and the strong dependence of the buffer parameters on the pump frequency. Instead, we use the diamond property derived in eq. (2.43) that the top-right and bottom-left edge of the diamond have a slope of $-\kappa_b/\kappa_a$. As shown in Figure 2.11, we find $\kappa_b/2\pi$ in the range $[13, 20]$ MHz. We later propagate the parameter range found for κ_a and κ_b on the rest of the calibration to give a robust confidence interval for g_2 and $\bar{n}$. We make the approximation that both κ_a and κ_b are constant in our experimental regime. In reality, their effective values vary lightly with the pump frequency. From measurements described above, we deduce the range among which these variations occur. We use this range to deduce an upper and lower bound for the experimental parameters obtained using the described calibration procedure.

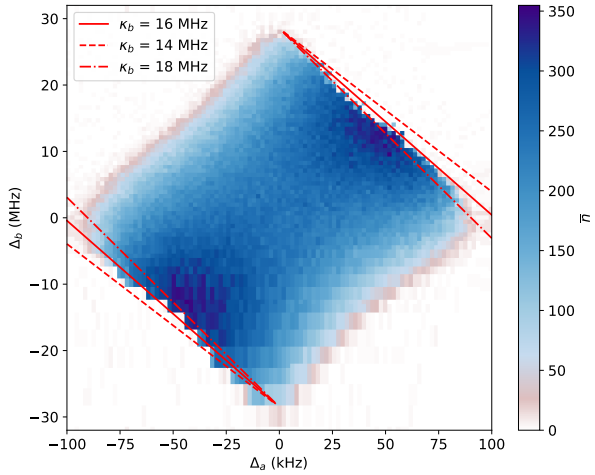

Figure 2.11: Radiated energy from the memory in units of circulating photon number (color) as a function of the detunings Δ_a (x-axis), and Δ_b (y-axis) defined in the text, for the drive amplitude $\epsilon_d/2\pi = 12.1$ MHz. The red solid line displays the fitted slope of the top-right and bottom-left edge, yielding the ratio κ_b/κ_a (see eq. (2.43)). The red dashed-dotted lines and the red dashed lines respectively give the upper and lower bound on this parameter (determined by graphical reading).

Independent checking of the calibration We can independently check the calibration of $|\alpha g_2|^2$ by studying the excess internal losses arising from the two-photon dissipation. When the two-photon dissipation becomes resonant, the internal losses of the memory measured by direct spectroscopy increase drastically and become nonlinear as a function of the probe power. The effective internal losses of the memory write

$$\kappa_{a,\text{eff}}^i = \kappa_a^i + 2\kappa_2|\alpha|^2 \tag{2.47}$$

where κ_a^i is the bare internal losses of the cavity and $|\alpha|^2$ is the average circulating photon number due to the spectroscopy tone. The excess losses rewrite $8|\alpha g_2|^2/\kappa_b$ and it provides an independent calibration of $|\alpha g_2|^2$ that we find in good agreement with the previous method.

3.3.2 Quantum signature

At the critical point, the semi-classical analysis fails to capture the curvature of the mean photon number $\bar{n}$ as a function of the drive amplitude ϵ_d (see the discrepancy between the plot from semi-classical analysis and experimental data on Figure 2.10 and Figure 2.12 (b)). This curvature results from the quantum fluctuations at the dissipative phase transition [75]. A full quantum model is necessary to capture this third notable feature, from which we extract the key parameter g_2. Instead, we perform a quantum analysis and compute the average photon number in the steady state ρ_∞ of the Lindblad equation generated by (2.21), $\bar{n} = \mathrm{Tr}(\rho_\infty a^\dagger a)$ using the `steadystate` function imported from the QuTiP python package [76, 77]. Once we express $|\alpha g_2|^2$ as a function of $|\epsilon_d g_2|$ (see Figure 2.10) the only fitting parameter is g_2. On Figure 2.10 it appears that the value of g_2 that best fits the experimental data is $g_2/2\pi = 39$ kHz. For the uncertainty interval, given the range of κ_a and κ_b, we estimate $g_2/2\pi \in [30, 46]$ kHz. This value will be independently confirmed by bit-flip times numerical simulations in the next section (see Subsection 4.1.3).

3.3.3 Recap of the extracted values

As a conclusion, the calibration gives the $\bar{n}$ reached in the cavity memory for every ϵ_d. Finally, with the photon number calibration in hand, the measurement records I and Q are rescaled to respectively coincide with a measurement of $(a + a^\dagger)/2$ and $(a - a^\dagger)/2i$.
Furthermore, for clarity, Table 2.2 gathers all experimental parameters values at the working point extracted in the Section 2 and in this current section (Section 3). Figure 2.12 is also recap of the distinct calibration steps.
From relation (2.3) and g_2 value we directly deduce the two-photon decay rate $\kappa_2/2\pi = 370$ Hz. This places our experiment in the regime where $\kappa_a/\kappa_2 = 150 \gg 1$. In the future the hybridization factor υ between the buffer and memory will be increased to enter the regime suitable for a qubit implementation: where the two-photon exchange rate largely dominates the cavity losses.
Eventually, with this method, we can extract the quantum efficiency number η from (2.20): we find $\eta = 2.8\%$. Next chapter will focus on measuring this quantity in a twin circuit, in order to check the order of magnitude of this quantity.

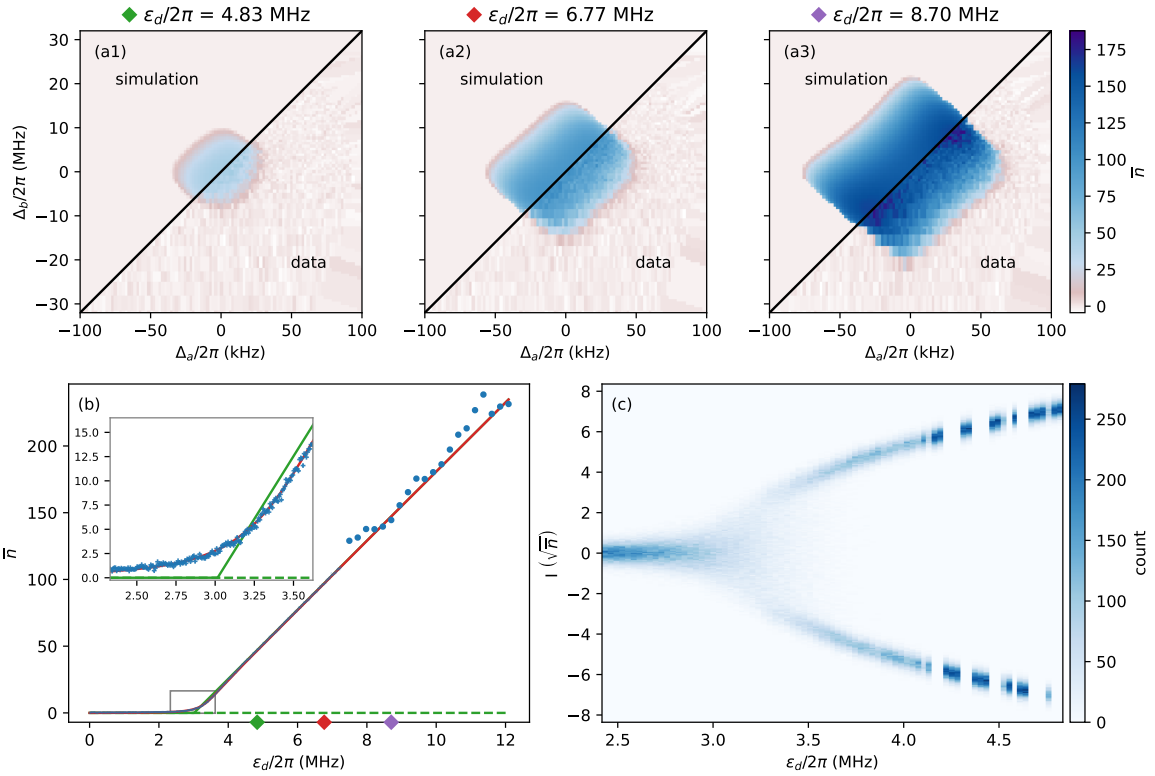

Figure 2.12: Emergence of two meta-stable pointer states from a nonlinear dissipative phase transition. (a1-a3) Radiated energy from the memory mode in units of circulating photon number (color) as a function of the detuning from the frequency matching condition $\Delta_a = \frac{1}{2}(\omega_p - (2\omega_a - \omega_d))$ (x-axis), and the detuning from the buffer resonance $\Delta_b = \omega_d - \omega_b$ (y-axis). We denote $\omega_{a,b,p,d}$ the memory, buffer, pump and drive angular frequencies respectively. Both data and semi-classical numerical simulations are shown in different regions of each panel corresponding to the specified drive amplitude ϵ_d. (b) Radiated energy from the memory in units of circulating photon number (y-axis) at $\Delta_a = \Delta_b = 0$ as a function of the drive amplitude (x-axis). The data correspond to an integration time of 10 µs with single averaging (circles) and 10000 averages (crosses). A semi-classical model (green solid line) captures the appearance of a critical point around $\epsilon_d/2\pi \approx 3$ MHz above which the vacuum state becomes unstable (green dashed line). A full quantum model (red solid line) is necessary to capture the curvature at the critical point, as emphasized by the zoom in the inset panel. (c) Histogram (color) of the I-quadrature integrated over 1 ms of the field radiated by the memory (y-axis) in units of the square root of circulating photon number as a function of the drive amplitude (x-axis). Passed the critical point, the memory field transits from the vacuum into two meta-stable pointer states.

$\omega_b/2\pi$	6.1273 GHz	$\kappa_a^i/2\pi$	18 kHz	$g_2/2\pi$	39 kHz
$\omega_a/2\pi$	4.0458 GHz	$\kappa_a^c/2\pi$	40 kHz	η	2.8%
$\omega_p/2\pi$	2.07 GHz	$\kappa_b/2\pi$	16 MHz	$\kappa_2/2\pi$	370 Hz

Table 2.2: Parameters at the operating point of the experiment. $\omega_b/2\pi$, $\omega_a/2\pi$, $\omega_p/2\pi$ are the buffer, memory and pump frequencies. $\kappa_a^i/2\pi$, $\kappa_a^c/2\pi$ are the internal and coupling loss rates of the memory, $\kappa_b/2\pi$ is the loss rate of the buffer, $g_2/2\pi$ is the two-photon coupling rate, $\kappa_2/2\pi$ is the two-photon dissipation rate and $\bar{n}_{\text{sat}}$ is the average number of photons at the bit-flip time saturation. The following parameters are given with confidence intervals: $\kappa_a^i/2\pi \in [15, 22]$ kHz, $\kappa_a^c/2\pi \in [39, 42]$ kHz, $\kappa_b/2\pi \in [13, 20]$ MHz, $g_2/2\pi/2\pi \in [30, 46]$ MHz, $\kappa_2/2\pi \in [270, 410]$, $\overline{n}_{\text{sat}} \in [43, 54]$.

3.4 Phase transition

At the critical point Figure 2.12 (c) clearly displays a phase transition of the memory internal state. This observed phase transition corresponds to a spontaneous symmetry breaking, where the cavity field adopts two opposite phases (or any quantum superposition of the two in the absence of single photon loss). We observe the emergence of these two phases by continuously acquiring, for each drive amplitude, 10000 times the I-quadrature of the radiated field integrated over $T_m = 1$ ms, for a total measurement duration of 10 s (see Fig. 2.12 (c)). For the lowest drive amplitudes ($\epsilon_d/2\pi \lesssim 2.7$ MHz), the cavity state remains in the vacuum, as signaled by the Gaussian distribution centered at $I = 0$. This distribution then broadens around the critical point (2.7 MHz $\lesssim \epsilon_d/2\pi \lesssim 3.5$ MHz), due to the significant overlap of the distributions of states $|\pm\alpha\rangle$ at small α and the multiple flips in between during the acquisition time $T_m = 1$ ms. For (3.5 MHz $\lesssim \epsilon_d/2\pi \lesssim 4$ MHz), the two states are well resolved, and their approximately equal weights hint towards a bit-flip time larger than the acquisition time of 1 ms and smaller than the full experiment duration of 10 s. For $\epsilon_d/2\pi \gtrsim 4$ MHz, the field stays pinned to one of the two computational states, hinting towards bit-flip times exceeding 10 s.

4 Time dynamics for the two-photon dissipative oscillator states

This section studies the time dynamics of the cavity states pinned by two-photon dissipation as a function of the time for various drive amplitudes (and thus various sizes of cavity states). For each cavity state size, we can extract a bit-flip time from the statistics of the time trajectory. We measure a bit-flip time exceeding 100 seconds for computational states containing about 40 photons.

The last part of this section is dedicated to the short timescale dynamics, that is to say the evolution of the buffer and memory states towards a stationary state once the two-photon pumping is turned on. Comparison of experimental data and theoretical behaviour on this timescale is another method for checking the values of previously derived experiment parameters.

4.1 Time trajectories and bit-flip times

4.1.1 Time trajectories

Trajectory calibration for different integration times We analyse the bit-flip time scale over several orders of magnitude, hence we increase the integration time T_m to keep manageable amount of data in long bit-flip traces. Thanks to the previous calibration, we can readily get the memory photon number from the (I, Q) statistics of the trace. Indeed, from eq. (2.33), we have both G from the value of $\overline{I^2+Q^2}\Big|_{\text{vac}}$ and $2G\kappa_a^c\eta$ from the calibration of $\bar{n}$. When given a trace with different integration time T'_m, we determine

$$\bar{n} = \frac{\overline{I^2+Q^2} - 2GT'_m}{2G\kappa_a^c\eta T'^2_m}\,. \tag{2.48}$$

This determination of $\bar{n}$ is more reliable than using the mapping between ϵ_d and $\bar{n}$ since this mapping may vary when the flux drifts.

Time statistics for jumps We access the dynamics of the memory by tracking individual trajectories over time (see Figure 2.13). For each trajectory, we set the drive amplitude at a fixed value ϵ_d, and record the I-quadrature of the radiated field. In order to resolve quantum jumps, we set the integration time T_m to be simultaneously smaller than the bit-flip time and sufficiently large to average out the heterodyne detection noise. We denote τ_{jump} the interval between two consecutive jump times, that we locate as the moments where I changes sign. To capture the statistical properties of each trajectory, we plot the cumulative distribution function of τ_{jump}. It shows approximately an exponential law, revealing an underlying Poisson process. The average of τ_{jump}, that defines the bit-flip time, undergoes a spectacular increase from 1 ms to 0.3 s to 206 s for an increase of photon number $\bar{n}$ from 11 to 28 to 43. With respect to the bare cavity lifetime of 2.7 µs, this represents a 10^8 increase of the bit-flip time, and (although inaccessible with our measurement scheme) an estimated $2 \times 43 = 86$ fold decrease of the phase-flip time.

4.1.2 Bit-flip time evolution

We quantify the scaling of the bit-flip time with the photon number by repeating the trajectory acquisition procedure for multiple drive amplitudes. From each trajectory we extract the bit-flip time and the corresponding photon number, and display them in Figure 2.14. We observe two distinct regimes.

Initially, the bit-flip time rises exponentially multiplying by a factor of about 1.4 for every added photon. In theory, in the limit where $\kappa_a/\kappa_2 \ll 1$, this factor would approach $e^2 \sim 7.4$ [51]. In this experiment we favoured stability over coupling strength, placing ourselves in the opposite regime $\kappa_a/\kappa_2 \sim 150$, which is expected to decrease this factor as confirmed by numerical simulations exposed in the next subsection (see 4.1.3).

For $\bar{n} \gtrsim 40$ photons, the bit-flip time saturates in the 100 second range. Although the origin of this saturation is yet to be established, its timescale is compatible with the measured rate of highly correlated errors in a large array of qubits [78], possibly due to high energy parti-

cle impacts [79, 80]. Future experiments could include monitoring oscillator trajectories over timescales of days or weeks to learn more about the phenomena causing these bit-flip events.

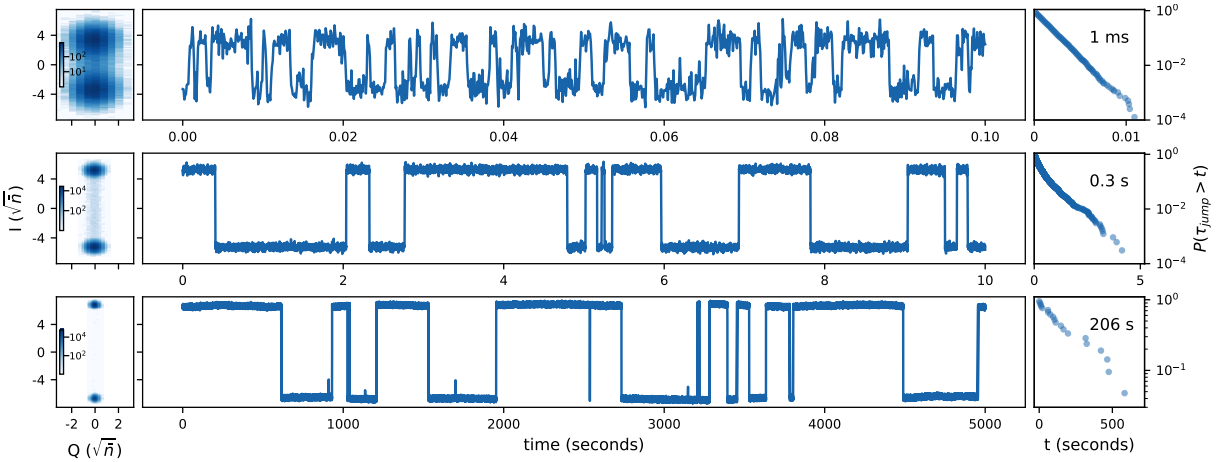

Figure 2.13: Real-time oscillator dynamics revealed by individual trajectories. For photon numbers $\bar{n} = 11, 28, 43$ (top, middle, bottom), we respectively set the integration time to $T_m = 0.1, 1, 5$ ms and the total measurement duration to $T_{tot} = 10, 1000, 5000$ s. (Left) Histogram of the (I, Q) quadratures of the radiated field. (Center) Trajectory of the I-quadrature as a function of time cropped from the full data-set. (Right) Cumulative distribution function of the stochastic time interval τ_{jump} in between two consecutive jumps. Its average value, that defines the bit-flip time, is printed on each panel.

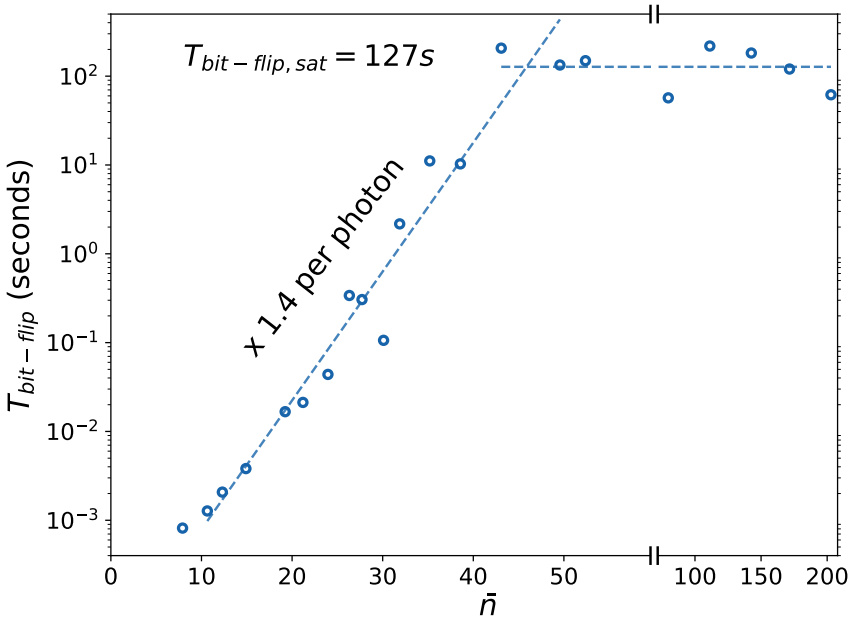

Figure 2.14: Exponential suppression of bit-flips. The bit-flip time (y-axis, log-scale) is measured (open circles) as a function of the number of photons contained in the pointer states $|0/1\rangle_\alpha$ (x-axis). The bit-flip time increases exponentially, multiplying by 1.4 per photon (tilted dashed line) before saturating at approximately 127 s (horizontal dashed line).

4.1.3 Bit-flip time simulation

We numerically simulate the dynamics of the memory described in eq. (2.1) using the `mesolve` function imported from the QuTiP python package [76, 77]. We run the simulation for three different values of g_2 (or equivalently κ_2). For each of these values, we sweep ϵ_2 in order to vary $\bar{n} = |\alpha|^2$ in the range of 4 to 40 photons. We initialize the memory in the coherent state $|\alpha\rangle$, and fit the expectation value of the annihilation operator a to an exponentially decaying function. The extracted decay time corresponds to the bit-flip time. In Figure 2.15, we display the computed bit-flip time as a function of the product $\bar{n} \times (g_2/2\pi)^2$, since it is a well calibrated quantity in our experiment. The data lie in the vicinity of the simulation results for $g_2/2\pi =$ 39 kHz, thus confirming our calibration of g_2.

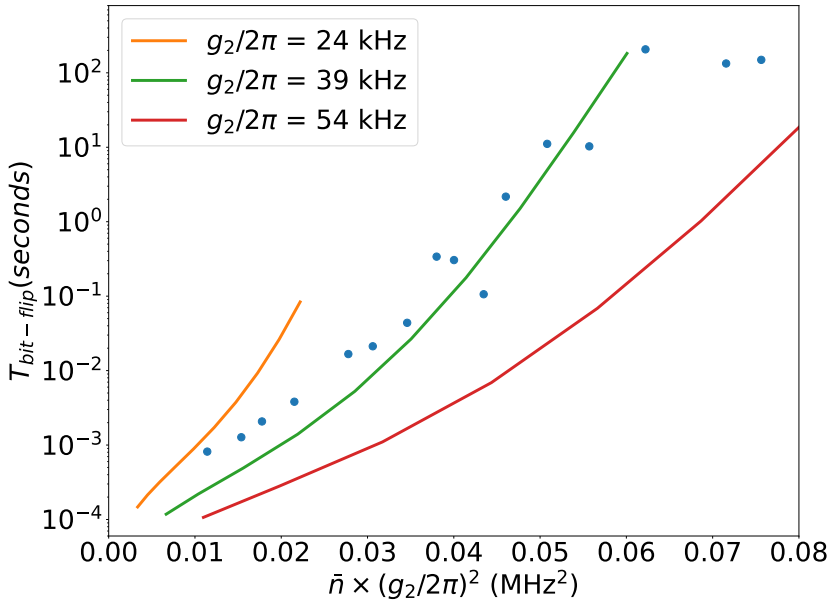

Figure 2.15: Numerical simulations (solid lines) of the bit-flip time (y-axis) for three values of g_2 (labels) as a function of the number of photons in the memory $\bar{n}$ multiplied by $(g_2/2\pi)^2$ (x-axis). The data (dots) from Figure 2.14 of the main text qualitatively matches the simulations for $g_2/2\pi = 39$ kHz, thus confirming our calibration of g_2.

4.2 Short timescale dynamics

The previous subsection focuses on the jumps statistics between the two meta-stable states stabilized by two-photon dissipation. In order to collect enough jumps events, the memory radiated field is recorded over a long timescale. Experimental data of the previous subsection lack an appropriate time resolution for analyzing the emergence of the two pointer states.
On the contrary, the goal of this subsection is to investigate the short timescale dynamics of the field inside the buffer and memory just after two-photon pumping is turned on. Here, we present experimental data acquired on a short timescale with high time resolution. We compare this data to simulated dynamics generated by a theoretical model fed with experiment parameters

extracted in previous sections (Sections 2 and 3). This comparison provides an additional check on the extracted parameters values.

Input/output theory The input/output theory allows us to connect the field inside the memory and the buffer to the collected signal out of these resonators. We send a single photon drive on the buffer port called b_{in}, and collect the signal out of the buffer and the memory via their respective dedicated ports. The experimentally acquired signal is proportional to a_{out} for the memory and to b_{out} for the buffer. Noting a the field inside the memory and b in the buffer, and κ_a^c, κ_b^c the respective coupling rates, the input/output theory yields

$$\begin{cases} a_{out} = \sqrt{\kappa_a^c}a \\ b_{out} = \sqrt{\kappa_b^c}b - b_{in}\,. \end{cases} \tag{2.49}$$

A specific calibration is required to determine the inner field characteristics of the memory and the buffer modes from the experimental raw acquired field quadrature.

4.2.1 Memory

Data calibration Figure 2.16 shows the time dynamics of the signal amplitude radiated out of memory. We have to calibrate the y-axis in number of photons as well as the drive amplitude ϵ_d value associated with each curve.
On this figure, we can clearly see how the field intensity in the memory evolves towards a stationary state. Once the stationary regime is reached, we pick the stationary state value for each drive amplitude, by averaging the reached values along the time axis. This results in a correlation between the drive amplitudes (in arbitrary units) and the steady state values of the field intensity (also in arbitrary units). The method previously exposed in Section 3 allows us to calibrate both the drive amplitude and the field intensity in number of photons at the same time. Then, we can report this linear scaling in number of photons for all data points (even before the stationary state) resulting in a complete calibration of Figure 2.16. It is important to note that this calibration is g_2, κ_a and κ_b dependent.

Simulation Since $\kappa_b \gg g_2$, adiabatic elimination allows the dynamics of the memory to be simulated using a one mode model of equation (2.1). We numerically simulate the dynamics of this equation using the `mesolve` function from the QuTiP python package [76, 77], with memory starting in vacuum as initial condition. The values of κ_2 and ϵ_2 are calculated from the experiment parameters according to equation (2.3).
As a result, one should keep in mind that both simulation and calibrated data rely on experimentally extracted parameters. They depend on the two-photon coupling rate g_2 which is extracted from calibration (see Section 3), as well as on directly fitted parameters: single photon loss rate of memory and buffer mode κ_a, κ_b and detunning of both modes, Δ_a, Δ_b.

Testing different g_2 values To test the robustness of the g_2 value, we plot the calibrated data and the simulation results in Figure 2.17 for two different values of two-photon coupling

$g_2/2\pi = 39\text{kHz} \pm 15$ kHz. We can see that for $g_2/2\pi = 24$ kHz the simulation underestimates the experimental data for small amplitudes and overestimates it for big amplitudes. Conversely, for $g_2/2\pi = 54$ kHz the simulation overestimates the data for small amplitudes and is even further away from the data for large drive amplitudes. This is an additional validation of the two-photon coupling rate value $g_2/2\pi = 39$kHz obtained in the previous section (see Section 3).

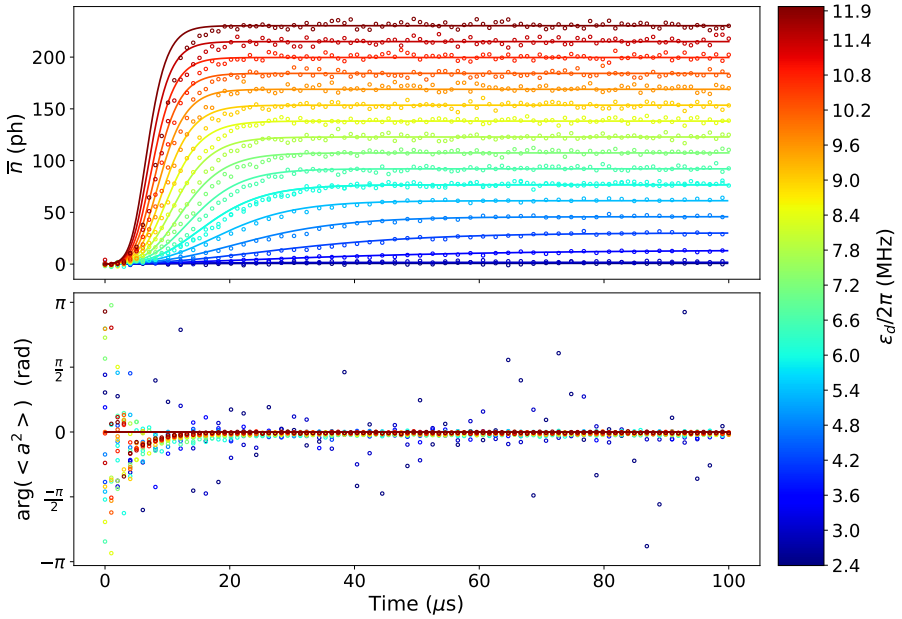

Figure 2.16: Real time number of photons dynamics inside the two-photon dissipative oscillator, from measurement and simulation, for increasing drive amplitudes. Top, respectively bottom, plot is modulus, respectively argument, of the average value of a^2 in the memory mode. Circles are experimental data points, solid lines stand for the simulated dynamics. The color scale indicates the single photon drive amplitude ϵ_d. The data were taken in two distinct data sets. The first data set contains amplitudes ranging from $\epsilon_d/2\pi = 2.39$ MHz to $\epsilon_d/2\pi = 5.98$ MHz with an integration time $T_{int} = 2$ µs. The second data set ranges from $\epsilon_d/2\pi = 5.98$ MHz to $\epsilon_d/2\pi = 11.97$ MHz with $T_{int} = 1$ µs. Each data point is averaged $N_{av} = 10000$ in both data sets. In order to have a meaningful phase average on the N_{av} repetitions, we plot the argument of mean value of a^2 rather than a. We took out the arbitrary angle due to initial phase from each data set. The photons numbers and the drive amplitudes were calibrated together taking $g_2/2\pi = 39$ kHz. The simulation was run with numerical parameters $\kappa_a/2\pi = 58$ kHz ; $\kappa_b/2\pi = 16$ MHz; $g_2/2\pi = 39$ kHz.

4.2.2 Buffer

Data calibration Because of the presence of an input drive, calibrating the signal collected out from the buffer port in terms of number of photons is more complex than for the memory. Fortunately, the buffer steady state has some properties that we can exploit for this calibration. A steady state regime is clearly displayed in Figure 2.18 just as it is for the memory: we pick the

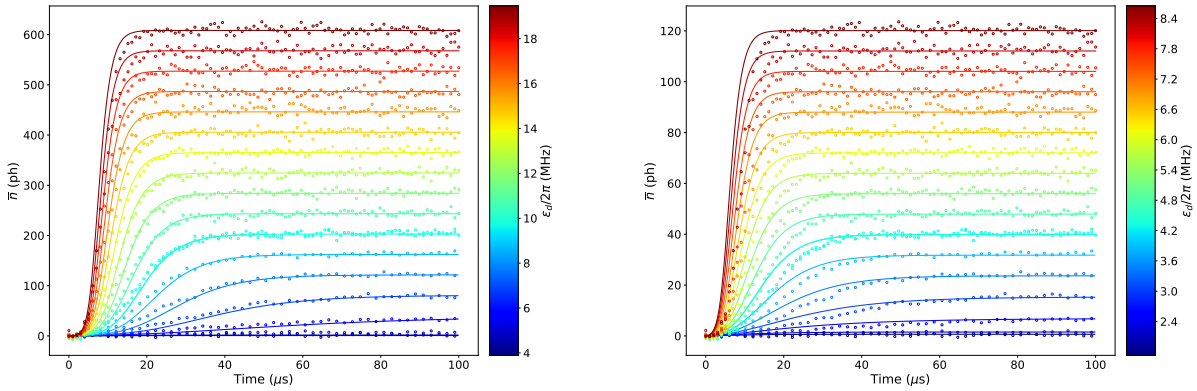

Figure 2.17: Real time number of photons dynamics inside the two-photon dissipative resonator, from measurement and simulation, for increasing drive amplitudes. Right plot is computed with $g_2/2\pi = 24$ KHz. Left plot is computed with $g_2/2\pi = 54$ KHz. Circles are experimental data points, solid lines stand for the simulated dynamics. The color scale indicates the single photon drive amplitude. The data acquisition and calibration procedures are detailed in the caption of Figure 2.16.

steady state amplitude value by averaging along time once the steady state regime is reached. Assuming there is no detunning ($\Delta_a = \Delta_b = 0$), the two-modes model dynamics are given by equation (2.18). As performed in Subsection 3.2, in the mean-field approximation at steady state, the a and b operators can be replaced by their mean value, the complex numbers α and β. As soon as $\alpha \neq 0$, we get from equation (2.37), the value of the steady state in the buffer

$$\beta = \frac{i\kappa_a}{4g_2} e^{2i\arg(\alpha)} . \tag{2.50}$$

One notable feature is that the angle $\arg(\alpha)$ does not depend on how strong we drive the memory state. This property can be used in equation (2.50) as soon as the memory state is not anymore in the blurred phase transition out of vacuum state. Consequently, for high enough drive amplitudes, the steady state of the buffer does not depend on this amplitude and should be the same for all time traces exposed in Figure 2.18.
Knowing that b_{in} is de facto proportional to the drive amplitude, this property allows us to find the scaling factor in front of b_{in} in the input-output equation (2.49). Finally, after removing this input contribution, equation (2.50) returns the actual expected value of β in $\sqrt{\text{ph}}$ units, allowing us to get the scaling factor for all time traces in Figure 2.18.

Simulation To simulate the time dynamics of the buffer, we use the Langevin equation on b operator (equation (2.35)) with zero detuning $\Delta_b = 0$. We take $b(t = 0) = 0$ as the initial condition. This dynamics includes the value of the memory field. Thus, we numerically solve this differential equation using: $< a^2(t) > = Tr(\rho_{sim}(t)a^2)$ with ρ_{sim} the simulated dynamics for the memory showed in Figure 2.16. We can see in Figure 2.18 that the numerical solution

gives the correct dynamics for buffer magnitude, even if the amplitude values do not perfectly match. On the contrary, this model cannot capture the slightly rotating dynamics of the buffer state.

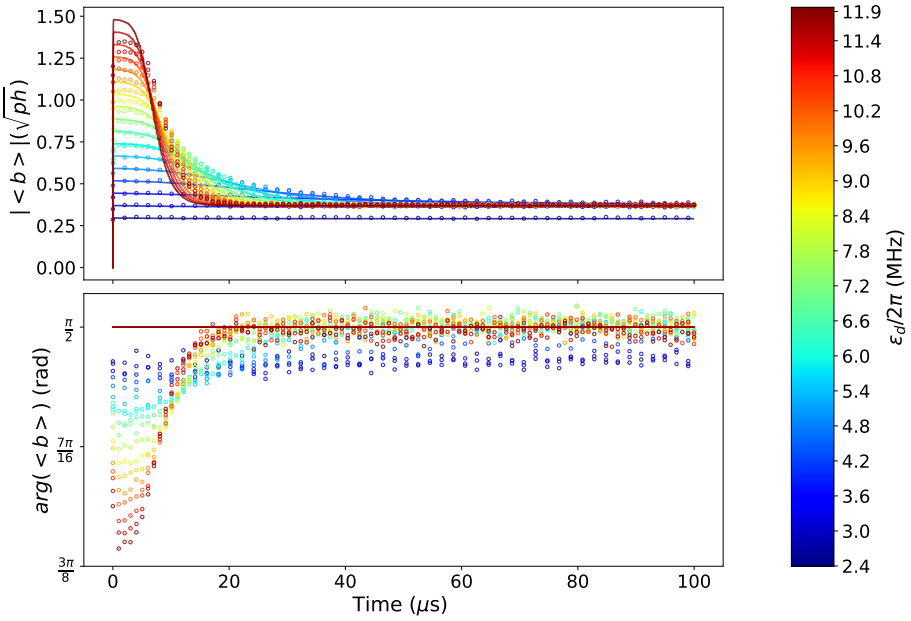

Figure 2.18: Real time dynamics inside the buffer resonator from measurement and simulation for various drive amplitudes. Top, respectively bottom, plot is modulus, respectively argument, of average value of b in the buffer mode. Circles are experimental data points, solid lines stand for the simulated dynamics. The color scale indicates the single photon drive amplitude ϵ_d. The data acquisition and calibration procedures are detailed in the caption of Figure 2.16. Moreover, the buffer data were calibrated referring to the theoretical amplitude of the steady state of the buffer as explained in main text. For each drive amplitude ϵ_d, the simulated dynamics is the numerical solution of the differential equation (2.35) with $\Delta_b = 0$; $\kappa_b/2\pi = 16$ MHz and $g_2/2\pi = 39$ kHz.

Including Kerr terms on the buffer We can refine the model by including the Kerr term on the buffer in the dynamics. This introduces an extra term into the Langevin equation (2.35) which becomes

$$\frac{db}{dt} = -\frac{\kappa_b}{2}b - ig_2^* a^2 + i\epsilon_d + i\chi_{bb}b^\dagger b^2. \tag{2.51}$$

This term has no effect on the field amplitude but causes the numerical curves to follow the data dynamics for the field phase. Figure 2.19 presents the simulation results with a tuned Kerr value in order to match the dynamics of experimental data as closely as possible. We find $\chi_{bb}/2\pi = 1.70$ MHz. Taking into account the estimated sources of self-Kerr in Subsection 1.3 and feeding them with the values of experimental parameters displayed in Table 2.1, we get a total estimated self-Kerr term of $\chi_{bb}^{est}/2\pi = 2.44$ MHz. Even if there are in the same order of magnitude, this estimation differs from the Kerr value numerically tuned to match

the experimental dynamics. This could indicate the presence of another nonlinear second order process modifying the buffer mode Kerr value.

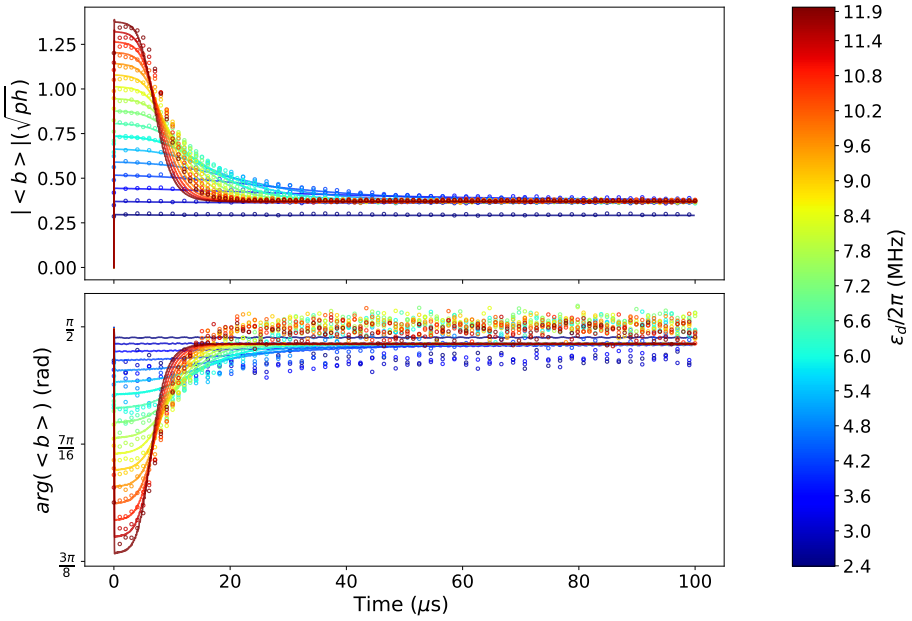

Figure 2.19: Real time dynamics inside the buffer resonator, from measurement and simulation, for increasing drive amplitudes. Top, respectively bottom, plot is modulus, respectively argument, of the average value of b in the buffer mode. Circles are experimental data points, solid lines stand for the simulated dynamics. The color scale indicates the single photon drive amplitude. The data acquisition and calibration procedures are detailed in the captions of Figures 2.16 and 2.18. The model is simulated using the equation (2.51) and takes the Kerr effect on the buffer mode into account with: $\chi_{bb}/2\pi = 1.70$ MHz and $\kappa_b/2\pi = 16$ MHz, $g_2/2\pi = 39$ kHz.

Chapter 3

Control experiment

Contents

Résumé en français

L'expérience de l'oscillateur muni de la dissipation à deux photons décrite dans le chapitre précédent a démontré un temps de bit-flip dépassant les 100 secondes. Toutefois, il est absolument crucial de connaitre le nombre de photons dans les états de la cavité pour lesquels ce temps a été atteint afin de déterminer si ce prototype pourra être utilisé comme bit quantique performant. Ainsi, l'objectif de ce chapitre est de contrôler la calibration du nombre de photons du chapitre précédent en utilisant un circuit de contrôle composé de la cavité couplée à un transmon.
La première section détaille les différents éléments de ce circuit de contrôle. La deuxième section présente la méthode de calibration du nombre de photons basée sur la détermination de l'efficacité quantique de détection de la cavité. La comparaison entre l'efficacité quantique de détection extraite du chapitre précédent avec celle extraite du circuit de contrôle permet de corroborer la calibration de l'expérience principale. Enfin, ce circuit de contrôle est aussi utilisé pour mesurer la population thermique dans le mode de la cavité, comme décrit dans la dernière section de ce chapitre.

In the two-photon dissipative oscillator experiment presented in Chapter 2, bit-flip time of order of magnitude of 100 s was observed. We stress again on the importance of knowing the number of photons in the memory states realizing this bit-flip time. Indeed, since [59] shows that phase-flips are going linearly with the size of the memory state, reaching this high bit-flip time for a macroscopic number of photons in the memory state makes a high-performance qubit impossible. However, reaching this bit-flip time for a few tens of photons in the memory state means that we still can operate it as a coherent qubit.
Chapter 2 details the method used to calibrate in situ the photon number in the memory state. Nevertheless, since the number of photons is definitely a key value, we perform an independent control experiment to corroborate the calibration. The objective of this chapter is to calibrate the number of photons in the memory mode thanks to a new device composed of the memory resonator coupled to a transmon. This device is detailed and characterized in the first section. The second section is dedicated to the calibration method via the extraction of the quantum detection efficiency of the memory resonator. Finally, in the last section, we also use the coupling between the transmon and the memory resonator in this device to measure the thermal population of the memory mode.

1 Chip presentation

1.1 The need for a supplementary device

Bit-flip time saturation due to the tomography apparatus A previous experiment implementing the two-photon exchange mechanism ([59]) revealed the exponential suppression of bit-flips and linear increase of phase-flips for Schrödinger cat states stored in the memory resonator. In this implementation, the memory resonator is coupled to one end to the buffer, and to the other end to a transmon qubit and a readout resonator followed by a parametric amplifier. This tomography apparatus enables probing the Wigner function of the state of the memory resonator. However, in this implementation, the tomography apparatus is the most probable cause for the bit-flip time saturating in the millisecond range. Indeed, [59] explains that the transmon qubit has a thermal population of 1%, a lifetime $T_1 = 5$ µs, and is dispersively coupled to the memory resonator. In the millisecond range, the qubit can get a thermal excitation, shifting the memory frequency by the dispersive shift value. This causes the cat-qubit state to rotate during an average time T_1, taking it out from the two-photon confinement potential and thus out from the cat-qubit computational basis. Once the transmon decays to ground state, the two-photon mechanism brings back the memory state to the computational basis but it can relapse to a bit-flipped state compared to the initial state. As a result, [59] is recommending to highly decrease the dispersive shift value between transmon qubit and memory in order to circumvent the saturation.
In the experiment of this thesis work, we are even more conservative: we decided to completely get rid of the tomography apparatus. Indeed, in the implementation presented in Chapter 2 the objective is to strip the cat-qubit circuit from anything we can afford and to probe the highest limit in bit-flip time we are able to reach thanks to two-photon dissipation mechanism. The

heavy cost of these choices is that we are in the regime where $\kappa_2 \ll \kappa_a$, making it impossible to measure quantum superposition states. However, the results presented Chapter 2 are really encouraging, proving that there is nothing at the core of the two-photon exchange mechanism restricts the bit-flip time up to 100 seconds. Future experiments can gradually work the way back to the regime suitable for qubits with $\kappa_2 \gg \kappa_a$.

Comparing calibration methods via the quantum detection efficiency Another consequence of the absence of tomography apparatus in the chip device is that calibrating number of photons in the memory state is not as straightforward as in [59]. Chapter 2 describes the calibration method of the average photon number $\bar{n}$ in the memory. This method relies on notable features of the dependency between the radiated power out of memory and the single-photon drive amplitude.
The quantum detection efficiency, noted η, quantifies how the signal-to-noise ratio is degraded with respect to the limit imposed by quantum vacuum fluctuation [81]. In the case of a resonator with a coupling rate κ_a^c, for a coherent state measured during the integration time T_m containing a number of photons $\bar{n}$, the measured mean $\overline{I}$ and standard deviation $\sigma(I)$ of the I-quadrature verify

$$\bar{n} = \left(\frac{\overline{I}}{\sigma(I)}\right)^2 \frac{1}{2\eta\kappa_a^c T_m} \,. \tag{3.1}$$

In the chip of Chapter 2, it was not possible to in situ measure the quantum detection efficiency of the memory resonator. If we were able to access to this quantity, the average photon number would have been directly calibrated thanks to (3.1). In this chapter, we present a chip with the memory resonator coupled to a transmon qubit in order to measure the quantum detection efficiency value and check if the calibration of Chapter 2 is accurate. The η value is inherently dependant on all the measurement chain. As a result, the issue is to keep everything as close to the experiment device from the previous chapter (in particular all the wiring setup around the memory resonator).

1.2 Chip presentation

We fabricate a new chip in order to evaluate the quantum detection efficiency η (see Section 2) and the thermal population of the memory mode n_{th} (see Section 3). In this chip, the fabricated memory resonator is identical to the one described in the main experiment and the entire two-photon exchange apparatus is replaced with a transmon qubit (see Figure 3.1). The chip was mounted in a similar sample holder and measured with an identical wiring on the memory port as in the experiment setup displayed in Figure 2.3.

Memory resonator The memory resonator is identical to device of Figure 2.1 based on a $\lambda/2$ resonator with exactly the same structure than the previous chip. We measure the same frequency than previously $\omega_a/2\pi = 4.0457$ GHz, and we measure coupling and internal loss rates $\kappa_a^c/2\pi = 38$ kHz and $\kappa_a^i/2\pi = 17$ kHz.

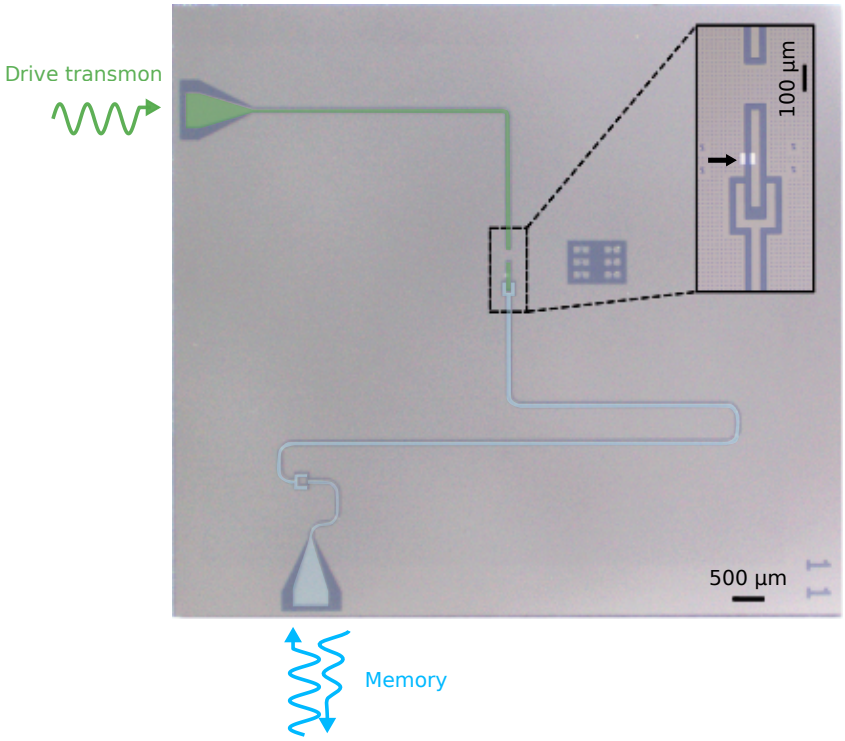

Figure 3.1: False-color optical micrograph of the detection efficiency chip in Nb (grey) on Si (dark blue). The memory resonator (blue) is capacitively coupled to a transmon (green).The inset focuses on the transmon and its Josephson junction in Al (light grey). We can address the memory and collect the reflected signal (blue waves) via the bottom 50 Ω port. The left 50 Ω port is dedicated to drive the transmon (green waves).

Transmon qubit The qubit is a transmon qubit, composed of a central shunting capacitance connected to ground via a Josephson junction, as shown in the inset of Figure 3.1. We aim for a qubit frequency of $\omega_q/2\pi \approx 6$ GHz in order to be sufficiently detuned from the memory resonator.

1.3 Transmon qubit characterization

The goal of this subsection is to present the measurement of the transmon characteristics values used in next sections. In the following, the memory resonator is also used as a readout resonator for the qubit.

Qubit characteristic times The relaxation time T_1 is an important qubit property. It is determined by applying a π-pulse and measuring the population of excited state after a waiting time t. The population is exponentially damped and a fit of the data measurement gives: $T_1 = 19$ µs (see Figure 3.2 left).
The coherence time T_2 is the other relevant characteristic qubit time. It is measured via a Ramsey sequence: a slightly detuned $\pi/2$-pulse is applied to the qubit, which is then left evolving freely

during a time t, after which a second $\pi/2$ pulse is applied, followed by qubit state readout. A fit of data measurement sets: $T_2 = 24$ µs (see Figure 3.2 right).
Those two characteristic times have associated rates κ_1 and κ_φ used later in this chapter and defined as

$$\begin{aligned} \kappa_1/2\pi &= \frac{1}{T_1} \\ \kappa_\varphi/2\pi &= \frac{1}{2T_1} + \frac{1}{T_2}\,. \end{aligned} \tag{3.2}$$

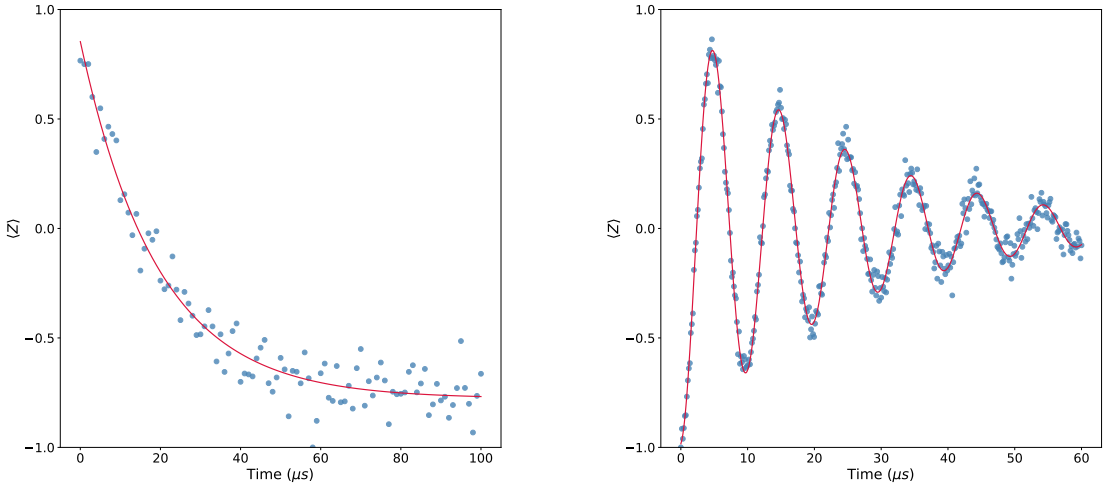

Figure 3.2: Left, respectively right, T_1, respectively T_2, measurement: data (blue circles) and fit (red solid line). (Left) The data are acquired for a total time of $T_{tot} = 100$ µs; time step of $T_s = 250$ ns with $N_{av} = 1000$ averages per point. The red line is the exponential fit $p(t) = A\exp(-t/T_1)$ where A is a scaling constant, giving $T_1 = 19.3$ µs. (Right) The data are acquired for a total time of $T_{tot} = 60$ µs; time step of $T_s = 150$ ns with $N_{av} = 4000$ averages per point. The red line is the fit by an oscillation with period T_2 modulated by an exponential decay due to T_1: $p(t) = A\cos(\frac{2\pi}{T_2}t)\exp(-t/T_1)$ where A is a scaling constant. The fit procedure gives $T_2 = 24.3$ µs.

Dispersive shift We have set the coupling strength between the qubit and the cavity to be sufficiently low in front of their frequency detunning in order to be in the dispersive regime. In this limit, a relevant quantity is the dispersive shift which quantifies the frequency shift induced by the qubit state on the cavity. Reversely, it also characterizes the frequency shift of the qubit induced by the photon number of the cavity. Hence, we can use the transmon to differentiate the different photon number states of the cavity.
We measure the dispersive shift by comparing the cavity spectroscopy measurement results when the transmon is initialized in its ground state or when the transmon is in its excited state (a π pulse is applied on the qubit just before performing the cavity spectroscopy), as displayed in

Figure 3.3. We evaluate: $\chi/2\pi = 1.75$ MHz. For reader convenience, Table 3.1 sums up all the

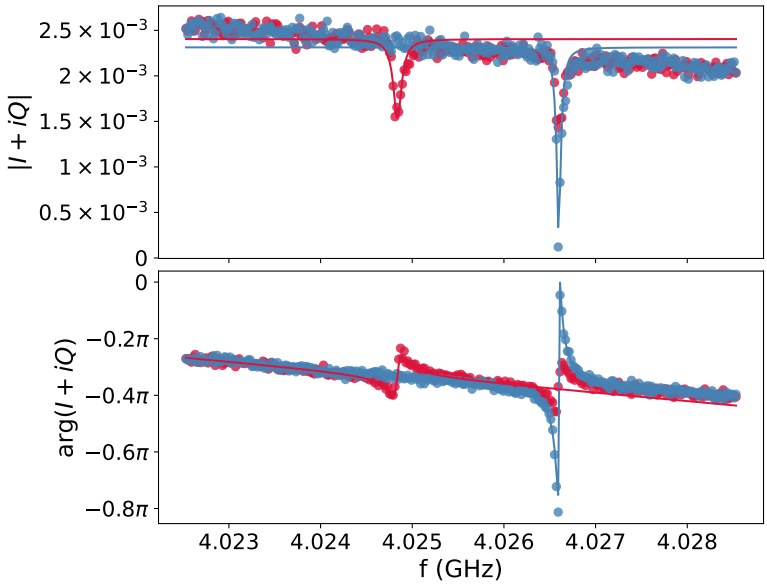

Figure 3.3: Dispersive shift measurement. Readout cavity spectroscopy with the qubit in its ground state (blue dots) and with the qubit in its excited state (red dots). Solid lines are fits of the resonance peaks. The spacing between the two resonance peaks gives $\chi/2\pi = 1.75$ MHz.

characteristic values of the memory resonator and the transmon qubit of the device of Figure 3.1.

$\omega_a/2\pi$	4.057 GHz
$\kappa_a^c/2\pi$	38 kHz
$\kappa_a^i/2\pi$	17 kHz

T_1	19.3 μs
T_2	24.3 μs
$\chi/2\pi$	1.75 MHz

Table 3.1: Parameters of the device used to calibrate the quantum detection efficiency. The transmon qubit lifetime and coherence times are denoted T_1 and T_2. The memory coupling and internal loss rates are denoted κ_a^c and κ_a^i, and χ corresponds to the dispersive coupling rate between the transmon and the memory resonator.

2 Evaluation of the quantum detection efficiency

The goal of this section is to detail the calibration method of the number of photons in the memory using its dispersive coupling to the transmon qubit. The calibration eventually provides an evaluation of the quantum detection efficiency η. Our evaluation of η follows three steps. First, we perform a standard spectroscopy in reflection of the memory mode in order to emulate a measurement signal that is directly proportional to the intra-cavity field amplitude $\langle a \rangle$. Second, for a given amplitude a_{in}, we calibrate the cavity photon number $\bar{n} = \langle a^\dagger a \rangle$ by resolving the

photon number splitting of the qubit. Third, for each calibrated photon number we measure the fluctuations of the output field a_{out} and we retrieve η by inverting eq. (3.1). We detail each step of this procedure in subsequent subsections.

2.1 Photon number resolved qubit spectroscopy

Memory spectroscopy For various incoming signal amplitudes S_{in}, we perform a spectroscopy measurement recording the reflected signal S_{out}. Using the results of the resonance fit, we can then translate the data in the (I, Q) plane in order to emulate a transmission signal: $S_{\text{t}} = A \langle a \rangle$, where A is an unknown scaling factor to be calibrated.

Theoretical description For various resonant signal amplitudes S_{in} we activate a drive on the transmon at a fixed amplitude S_q with a varying detuning Δ_q.
We note down a the memory annihilation mode operator and q the qubit annihilation mode operator. We note Ω_a (respectively Ω_q) the drive on the memory (respectively on the qubit). We recall that κ_1, κ_φ are deduced from characteristic qubit times as in (3.2). χ and κ_a are taken from Table 3.1. The dynamics is described by

$$\begin{aligned} \partial_t \rho &= -i\,[H, \rho] + D\left[\sqrt{\kappa_a} a\right] \rho + D\left[\sqrt{\kappa_1} q\right] \rho + D\left[\sqrt{\kappa_\varphi} q^\dagger q\right] \rho \\ H &= \Delta_q q^\dagger q - \chi a^\dagger a q^\dagger q + \Omega_a \left(a + a^\dagger\right) + \Omega_q \left(q + q^\dagger\right) \ . \end{aligned} \tag{3.3}$$

Numerical simulation and measurement results For each initial input amplitude and transmon drive amplitude and detunning, we collect the reflected signal amplitude and deduce the transmitted amplitude S_{t}. The data $S_{\text{t}}(\Delta_q, S_{\text{in}}, S_q)$ are then fitted to the result of a numerical simulation. Using the `steadystate` function of the QuTiP package [76, 77], we solve the dynamics of (3.3). From this simulation we extract $\langle a \rangle (\Delta_q, \Omega_a, \Omega_q)$, that is used to fit the dataset $S_{\text{t}}(\Delta_q, S_{\text{in}}, S_q)$, where the fit parameters are the proportionality constants relating S_{in} to Ω_a, S_q to Ω_q and S_{t} to $\langle a \rangle$ (see Figure 3.4).

2.2 Output field statistics

For every drive amplitude S_{in}, the previous fit estimates the intra-cavity field $\langle a \rangle$, and hence $\bar{n}$. By acquiring histograms of the output field S_{t}, we now invert eq. (3.1) and retrieve $\eta \simeq 7\%$. This is a factor two larger than the previously estimated value in calibration method of the previous chapter (see Chapter 2, Section 3). This deviation can be attributed to differences in the RF connections of the two samples. These values may be explained by lossy elements (two circulators, one Eccosorb filter and two directional couplers) between the sample and the TWPA.
Yet, this measurement validates the order of magnitude of number of photons in the memory state for the macroscopic bit-flip times presented in Chapter 2. In conclusion, the experiment with this new device corroborates the high-efficiency of the implementation of the two photon dissipative oscillator exposed in this thesis work.

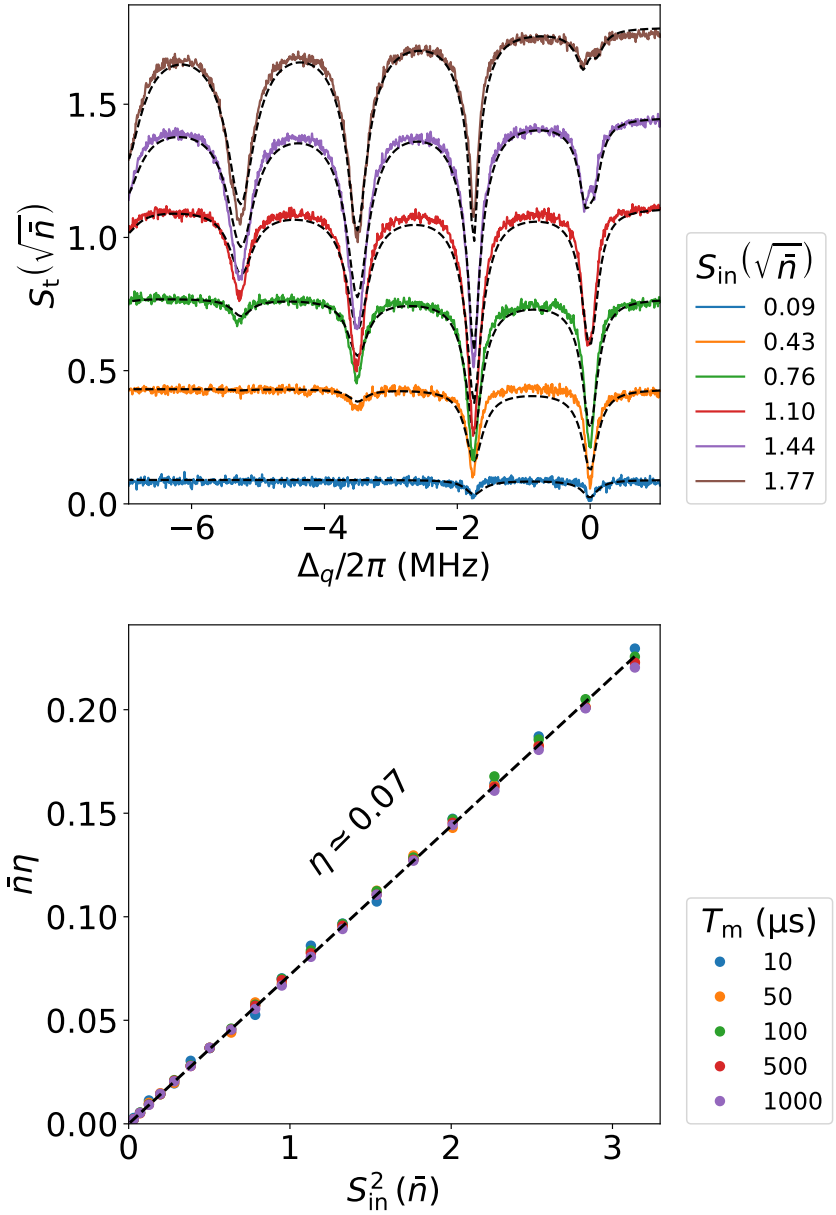

Figure 3.4: Calibration of the detection efficiency η. (Top) Qubit spectroscopy showing photon number splitting for various drive amplitudes (colors): data (solid lines) and fit (dashed lines). (Bottom) Product $\bar{n}\eta$ computed using equation (3.1) as a function of the square input signal S_{in}^2 in units of photon number. This was performed for various integration times T_m (colors) to ensure consistency.

3 Measurement of thermal occupation of the memory resonator

We recall from Chapter 2 that once the two-photon conversion is turned on, we measure the radiated energy from memory as a function of the drive amplitude. Figure 2.12 (c) depicts the I-quadrature acquisition result as a function of drive amplitude and clearly exhibits a phase transition. First, the cavity state remains in vacuum as indicated by the Gaussian distribution centered at $I = 0$. This output power is close to zero until the two-photon injection rate overcomes the memory losses. At this critical point we observe a non-linear dissipative phase transition [75]. The cavity field broadens and eventually adopts two opposing phases, revealing two well-resolved states.
This phase transition is triggered by field fluctuations with two contributions. Vacuum field fluctuations are the first one. Thermal field fluctuations are the second one. Since the memory mode is around 4 GHz, its thermal occupancy is expected to be very small (less than a percent, as typically found in similar setups [59]). This thermal occupation is therefore assumed to be zero in the photon calibration of Chapter 2. In this section, we measure the thermal occupation using the transmon to ensure that our photon number calibration of Chapter 2 is valid.

3.1 Theoretical model

We note down n_{th} the number of thermal photons in the memory mode at frequency $\omega_a/2\pi$. As in equation (3.3), a is the annihilation operator of the memory mode. κ_d and κ_u are the jump rates of the memory due to its thermal environment, which are linked to the coupling rate of memory κ_a as (see [82])

$$\begin{aligned} \kappa_d &= (1 + n_{th})\kappa_a \\ \kappa_u &= n_{th}\kappa_a. \end{aligned} \tag{3.4}$$

The Pauli operators of the qubit are $\sigma_{x,y,z}$, $\sigma_{\pm}$. Δ_q is the detuning of the drive of the qubit. The Linbladian operators L_1, respectively L_φ, stand for relaxation, respectively dephasing, on the qubit, with associated rates defined in (3.2). We model the interaction of the qubit and the cavity in the rotating frame as follows

$$\begin{aligned} H &= -\chi a^\dagger a \sigma_+\sigma_- - \Delta_q \sigma_+\sigma_- \\ L_d &= \sqrt{\kappa_d}a \ ; \ L_u = \sqrt{\kappa_u}a^\dagger \\ L_1 &= \sqrt{\kappa_1}\sigma_- \ ; \ L_\varphi = \sqrt{\frac{\kappa_\varphi}{2}}\sigma_z \, . \end{aligned} \tag{3.5}$$

Intuitive reasoning We note $|\Psi(t)\rangle$ the state of the qubit as a function of time. We study the qubit's dynamics starting from the equatorial state: $|\Psi(t=0)\rangle = \frac{1}{\sqrt{2}}(|0\rangle + |1\rangle)$.
First, we evaluate the dynamics in an intuitive manner. In the case with no thermal photons in the memory mode $n_{th} = 0$, solving (3.5) yields to the expectation value of σ_x noted here $\langle\sigma_x\rangle_0(t)$

$$\langle\sigma_x\rangle_0(t) = \exp^{-t/T_2}\cos(\Delta_q \times t). \tag{3.6}$$

On the contrary, when the cavity has a thermal occupation of $n_{th} = 1$, the measurement result of σ_x operator is noted $\langle\sigma_x\rangle_1(t)$ and follows the dynamics

$$\langle\sigma_x\rangle_1(t) = \exp^{-t(1/T_2+\kappa_a)} \cos\left((\Delta_q + \chi) \times t\right). \tag{3.7}$$

We note $\rho(t)$ the density matrix of the cavity as a function of time. The initial state of the cavity in the generic case is a mixed state: $\rho(t=0) = (1-n_{th})\,|0\rangle\langle 0| + n_{th}\,|1\rangle\langle 1|$. In this case, an intuitive way of thinking is to assume that the qubit will follow the dynamics of (3.6) with probability n_{th}, and a dynamics of (3.7) with probability $1 - n_{th}$. As a result, measuring the expectation value of σ_x as function of time allows us to recover the n_{th} value. This reasoning, however, is not exact: a numerical simulation of the entire Linblad equation (3.5) is required to capture all of the subtleties of the combined effects of memory losses, thermal population, and qubit dephasing.

3.2 Measurement

Experiment description We first apply a $\pi/2$ pulse on the qubit detuned by Δ_q. Then, we wait for a time t and we apply a $-\pi/2$ pulse on the qubit just before qubit state readout. This allows us to access to the measurement of σ_x operator after the evolution during time t. We extract n_{th} from those measurement results using the different timescales of the dynamics.
Two datasets are acquired and are shown in Figure 3.5. Dataset A has a total duration of a few T_2: the time step is too large to distinguish oscillations due to the dispersive shift. Therefore, a dataset B is acquired on a shorter time scale with refined discretization in order to see those oscillations. We call in the following $\sigma_{A,B}(t)$ the qubit measurement results of these two sets.

Estimation of n_{th} We cannot solve the evolution of the qubit dynamics given by (3.5) analytically. Hereafter we use the intuitive model from the previous paragraph to analyze the experimental data and estimate n_{th}. In this approximate model, we assume that the σ_x measurement result is

$$\langle\sigma_x\rangle(t) \;\approx\; n_{th}\langle\sigma_x\rangle_1(t) + (1-n_{th})\langle\sigma_x\rangle_0(t)\,. \tag{3.8}$$

The goal is to extract an approximation of n_{th} using the different timescales in the experimental data. Comparing (3.6) and (3.7) it appears that $\langle\sigma_x\rangle_1(t)$ has faster damped dynamics than $\langle\sigma_x\rangle_0(t)$. Since dataset A is taken on a long time scale and with a large time step, we can assume that it is dominated by dynamics of $\langle\sigma_x\rangle_0(t)$ and we have

$$\sigma_A(t) \approx C + K \exp^{-t/T_2} \cos\left(\Delta_q t\right) \tag{3.9}$$

where C and K are scaling constants. The agreement of the data and the fit of expression (3.9) validates the assumption (see Figure 3.5 left). Furthermore, the fitting routine extracts the constants C and K values, which are then used to rescale the dataset B. This rescaled data

is denoted as $\widetilde{\sigma_B}(t)$ and is shown in Figure 3.5 right, in blue

$$\widetilde{\sigma_B}(t) = (\sigma_B(t) - C)/K\,. \tag{3.10}$$

Since dataset B is acquired with an short time step, it should contain both contributions of (3.6) and (3.7)

$$\widetilde{\sigma_B}(t) \approx \langle\sigma_x\rangle_0(t) + \frac{n_{th}}{1+n_{th}}\langle\sigma_x\rangle_1(t)\,. \tag{3.11}$$

Dataset B is taken for times values $t \ll T_2$ so that the dynamics of $\langle\sigma_x\rangle_0(t)$ in this data can be approximated by a linear dynamics. We linearly fit $\widetilde{\sigma_B}(t)$ and substract this linear contribution from $\widetilde{\sigma_B}(t)$ (Figure 3.5 left, in green). As a result, the final data $\widetilde{\widetilde{\sigma_B}}(t)$ should be as follows

$$\widetilde{\widetilde{\sigma_B}}(t) \approx \frac{n_{th}}{1+n_{th}}\langle\sigma_x\rangle_1(t)\,. \tag{3.12}$$

The data $\widetilde{\widetilde{\sigma_B}}(t)$ can be fitted using (3.12) and (3.7). The agreement between the fit and the data (Figure 3.5 right, green and orange) yields $n_{th} = 0.013$ in the frame of this approximation.

QuTiP simulation Since the extraction of n_{th} value is not exact, we perform a numeric simulation of the full-model Hamiltonian of (3.5), using the `mesolve` function of the QuTiP package [76, 77]. We initialize the system as mentioned above with the qubit in equatorial state and the cavity in the superposition of states weighted by n_{th}. Figure 3.5 demonstrates that the simulation results with extracted parameters values correspond to the experimental data. This simulation validates the value of $n_{th} = 0.013$.

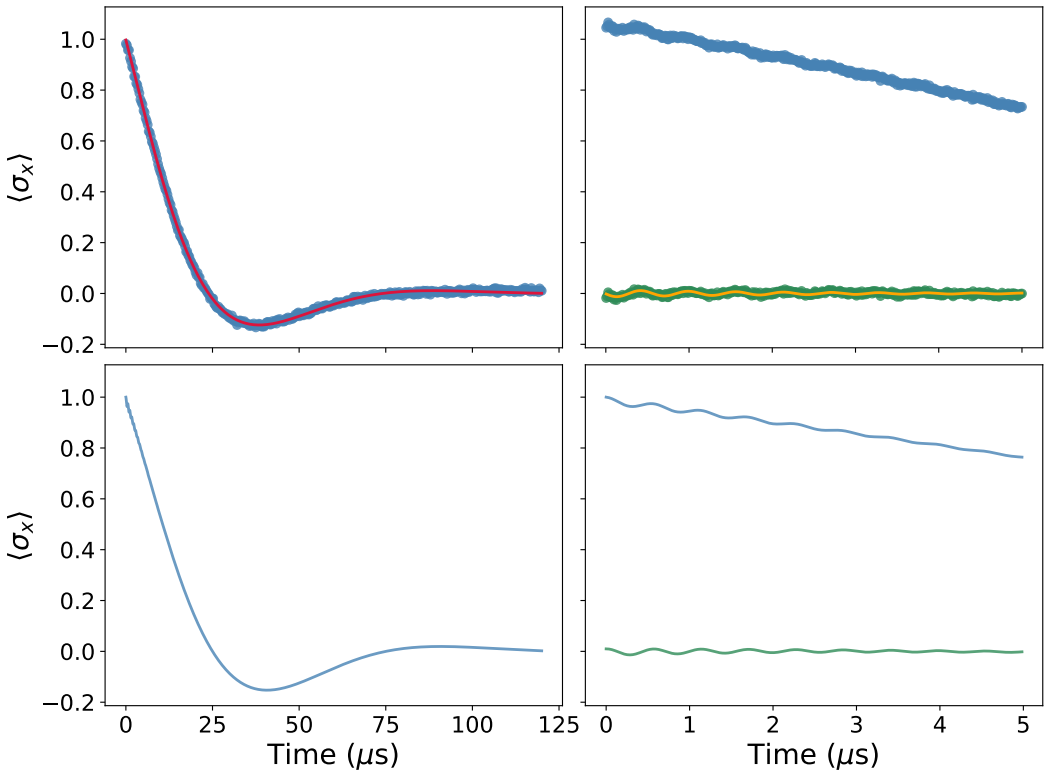

Figure 3.5: Measurement of thermal population of the memory resonator n_{th}. (Top part) Measurement result of σ_x operator of the qubit for different waiting times between the two $\pm\pi/2$ pulses. Left and right plots represent different data sets. Left, respectively right, plot has experimental parameters: $T_{tot} = 120$ µs, respectively $T_{tot} = 5$ µs, time resolution is $T_s = 300$ ns, respectively $T_s = 12$ ns, and $N_{av} = 400000$ averages for one data point for both data sets. Blue circles represent the data. Green circles represent the data calibrated according to (3.10). The red solid line is a fit according to (3.9) with $T_2 = 20.7$ µs, $\Delta/2\pi = 10$ kHz. The orange line is a fit of (3.12) giving $n_{th} = 0.013, \tau = 2.43$ µs, $\chi/2\pi = 1.75$ MHz. (Bottom part) QuTiP simulation result of $\langle\sigma_x\rangle$ solving the dynamics of (3.5) as function of waiting time t. Left plot is the total $\langle\sigma_x\rangle$ dynamics. Right plot is a zoom in time on the short times: the blue line is the total $\langle\sigma_x\rangle$ dynamics and the green line is the $\langle\sigma_x\rangle$ dynamics from which $\langle\sigma_x\rangle_0$ contribution was subtracted. We have simulated Hamiltonian of (3.5) with parameters: $T_1 = 19$ µs, $T_2 = 20.7$ µs, $\chi/2\pi = 1.75$ MHz, $\Delta_q/2\pi = 10$ kHz, $\kappa_a/2\pi = 50$ kHz and $n_{th} = 0.013$.

Chapter 4

Circuit design

Contents

Résumé en français

L'oscillateur pourvu de la dissipation à deux photons est réalisé dans le champ électromagnétique d'un résonateur supraconducteur qui échange les photons par paires avec son environnement. L'implémentation en architecture de circuit d'électrodynamique quantique des principaux éléments de ce circuit est exposée dans le Chapitre 2. Le chapitre qui suit est dédié la conception de composants micro-ondes annexes du circuit, mais toutefois indispensables au bon fonctionnement global du prototype.
Ainsi, la première section traite de la conception d'un filtre coupe-bande centré sur la fréquence fondamentale de la cavité. La section suivante détaille la conception d'un bias-tee sur puce afin d'acheminer de façon adéquate des courants continus et micro-ondes dans le circuit. Les deux sections suivent la même méthode de conception et passent d'un modèle théorique de circuit par bloc fonctionnel, à des simulations électromagnétiques 3D par éléments finis, jusqu'à la fabrication de prototypes qui sont testés et finalement validés. Ce chapitre détaille à dessein certaines techniques et méthodes d'ingénierie micro-ondes afin de pouvoir être une ressource pédagogique pour la conception de composants micro-ondes similaires.

The two-photon dissipative oscillator is embedded in the cavity field of a superconducting resonator that exchanges pairs of photons with its environment. The two-photon interaction is based on the buffer mode that mediates a nonlinear coupling between the memory and its environment. Therefore, the memory and the buffer resonators are the two main parts of the superconducting circuit presented in Chapter 2 (see Figure 2.1). Their implementation in circuit quantum electrodynamics coplanar waveguide architecture is detailed in Chapter 2, Section 1. Yet, other on-chip elements had to be designed to make the whole circuit operational and are presented in this chapter.
First, the two-photon interaction relies on the coupling of the memory mode to the lossy buffer mode. An undesired side effect of this coupling is to increase the decay rate of the memory due to the Purcell effect, which runs counters to the experiment purpose. To prevent this, Section 1 focuses on the design of a stop-band filter centered at the memory frequency, consisting of three $\lambda/4$ sections on both routes linking the memory to its cold bath.
Second, to engineer the two-photon interaction, the ATS has to be threaded with a common and differential DC flux around a specific working point. Moreover, the buffer has to be driven and pumped via RF waves. Since both RF drives and DC currents have to be routed to the ATS, a bias tee component is required. Yet, the left and right loops of the ATS have to be independently DC-biased. This implies to fully control the path of the DC currents on the chip. This is why Section 2 explains the design of on-chip bias tees.
Designing and simulating the circuit of the two-photon dissipative oscillator chip was one of my main contributions to this project. This chapter outlines the process that led me to the experimental chip exposed in Chapter 2. Each component design process gradually goes from theoretical lumped models, to 3D finite elements electromagnetic simulations, to eventually fabricating test devices and probing them. This chapter details some RF design techniques in order to be useful for readers wishing to design similar on-chip elements.

1 Designing a stop-band filter

1.1 Introduction

This section explains the development of filtering elements to mitigate the direct coupling of the memory to the input lines of the buffer. In the previous implementation of [59] the buffer input line was filtered via three $\lambda/4$-stubs filters tuned at the memory frequency. We present the design of more efficient stop-band filters in this section.
We recall that at the experiment operating point the buffer resonates at $\omega_b/2\pi = 6.1273$ GHz with an energy decay rate $\kappa_b/2\pi = 16$ MHz. Regarding the memory, we aim for a relatively low frequency of $\omega_a/2\pi = 4.0457$ GHz and we measure the coupling and internal loss rates $\kappa_a^c/2\pi = 40$ kHz and $\kappa_a^i/2\pi = 18$ kHz. Ideally, the filtering element would block waves at memory frequency and be transparent for the others frequencies. Thus, we aim for a stop-band filter with high attenuation at its center frequency and a narrow bandwidth. There are also dimensional constrains: the filters should fit inside the chip area next to all other coplanar waveguide structures.

The first subsection exposes step by step the theoretical construction of a stop-band filtering lumped circuit element based on [83, 84]. Once we have a lumped model, we should implement it in a coplanar waveguide version. The second subsection presents the 3D finite elements electromagnetic simulations to adjust the circuit element design. Finally, as explained in the last subsection, we fabricate a test version and measure it, before integrating this element to the chip experiment.

1.2 Designing a lumped model of a stop-band filter

We aim to design a stop-band filter between a power source, standing for the memory mode leaking via the buffer, and a 50 Ω impedance that models the circuit port plus all the cables lying behind. Therefore, we want to build a single-terminated filter as shown in Figure 4.1. On the real chip, since the buffer feedline has two arms (see Figure 2.1), we will have to put the filtering element between the buffer and each exterior port.

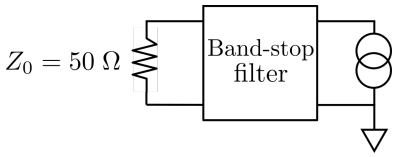

Figure 4.1: Diagram of the stop-band filter between the power source representing the memory mode radiating through the lossy buffer mode and the 50 Ω load impedance standing for the external cabling environment.

We note down $\Delta\omega$ the bandwidth, $\omega_{1,2}$ the -3 dB frequencies on both sides of central frequency. We have: $\omega_{1,2} = \omega_0(1 \pm \frac{\Delta\omega}{2})$. The target parameters are

$$\begin{aligned} \omega_0/2\pi &= 4\ \text{GHz} \\ \Delta\omega/\omega_0 &= 20\%\,. \end{aligned} \tag{4.1}$$

Designing an RF filter is a topic covered by classical RF engineering textbooks. In the following, we mainly refer to [83, 84] in order to explain all the steps to build an on-chip filtering circuit element meeting those requirements.

Low-pass filter prototype The most simple low-pass filter prototype is the default LC filter with $\omega_c/2\pi = 1$ Hz and $Z_0 = 1\ \Omega$. First, we have to choose the filter type, conditioning the attenuation profile as function of frequency. We choose here a Chebyshev filter (also said "equal ripples") with 3-dB ripples since it provides a sharp rate of cutoff. The drawback is that inside the central band around ω_0 the attenuation will be minimal with ripples of maximum amplitude of 3dB, but this is acceptable in our case.
We also have to determine the number of reactive elements in the circuit: the more dipoles, the more efficient is the attenuation in the stop-band zone. However, for implementation, the more reactive elements are involved the more space on the chip is required. It appears that a filter with $n = 2$ reactive elements guarantees acceptable attenuation so we keep this minimal

number.
Figure 4.2 shows a circuit diagram of the filter. For clarity, we take the notation convention of [83] and we note $g_{0,1,2,3}$ for the normalized element values which are defined as:

- $g_0 = 1\ \Omega$ (stands for the normalized 50 Ω impedance)
- g_1 is the normalized coil inductance
- g_2 is the normalized capacitance value
- $g_3 = \infty$ (stands for the power source)

For a single-terminated Chebyshev filter with $n = 2$ elements and 3-dB ripples [83] gives

$$\begin{aligned} g_0 &= 1\ \Omega \\ L = g_1 &= 1.5506\ \text{H} \\ C = g_2 &= 0.9109\ \text{F} \\ g_3 &= \infty \end{aligned} \tag{4.2}$$

with L the inductance value and C the capacitance value.

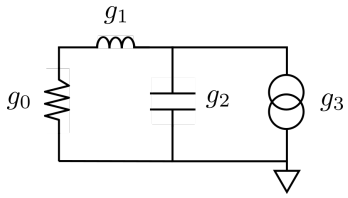

Figure 4.2: Circuit diagram of lumped element low-pass filter prototype with two reactive elements. The circuit is composed of the load impedance g_0, an inductance of normalized value g_1, a capacitance of normalized value g_2, and an ideal power source with infinite impedance g_3.

Scaling on target parameters It is really common when engineering filters to refer to a prototype normalized filter and next, to scale to the requested parameters values. The prototype filter parameters are noted: $\tilde{Z_0} = 1\ \Omega$, $\tilde{\omega_c}/2\pi = 1$ Hz, in order to appear in the scaling formulas. In our case, we must scale the prototype coefficients to get to the desired parameters: $\omega_c/2\pi = \omega_1/2\pi = 3.2$ GHz and $Z_0 = 50\ \Omega$.
In order to change the filter impedance to Z_0, all the individual impedances of the prototype have to be multiplied by $Z_0/\tilde{Z_0}$ factor. Noting with a prime symbol the new components value, this directly gives: $L' = L \times Z_0/\tilde{Z_0}$ and $C' = C \times \tilde{Z_0}/Z_0$.
To change the cut-off frequency from unity to ω_c, we have to globally scale the frequency dependence of the filter by the change of variable: $\omega \to \omega \times \frac{\tilde{\omega_c}}{\omega_c}$. Taking the individual components impedance provides the new capacitance and inductance values

$$\begin{aligned} jL\omega \to jL\omega \times \frac{\tilde{\omega_c}}{\omega_c} = jL'\omega, \text{ with } L' = L \times \frac{\tilde{\omega_c}}{\omega_c} \\ \frac{1}{jC\omega} \to \frac{\omega_c}{jC\omega\tilde{\omega_c}} = \frac{1}{jC'\omega}, \text{ with } C' = C \times \frac{\tilde{\omega_c}}{\omega_c}\,. \end{aligned} \tag{4.3}$$

Impedance and frequency scaling can be combined, resulting in our case in

$$\begin{aligned} g_0' &= Z_0 = 50\ \Omega \\ L_1 = g_1' &= g_1 Z_0 \frac{1}{\omega_c} = 1.92\ \text{nH} \\ C_2 = g_2' &= \frac{g_2}{Z_0 \omega_c} = 0.453\ \text{pF} \\ g_3' &= \infty\,. \end{aligned} \tag{4.4}$$

From low-pass filter to stop-band filter Classic RF engineering textbooks explain how low-pass filters can be converted into other types of filters (high-pass, stop-band, band-pass) by rescaling the frequency variable in the frequency dependency of the filter. To get a stop-band filter from a low-pass filter, we have to perform the transformation $\frac{\omega}{\tilde{\omega}_c} \rightarrow -\Delta\big(\frac{\omega}{\omega_0} - \frac{\omega_0}{\omega}\big)^{-1}$ with Δ being the fractional bandwidth of the filter: $\Delta = \frac{\omega_1 - \omega_2}{\omega_0}$ and $\omega_0,\ \omega_1,\ \omega_2$ defined in (4.1). This change of variables maps the central frequency ω_0 to $+\infty$ and is visually represented by the two attenuation-frequency plots in Figure 4.3.

We can write the expression of individual impedances in this new frame. For instance, in the case of the capacitance C, we get:

$$\frac{1}{jC\omega} \rightarrow -\frac{1}{jC\Delta\tilde{\omega}_c}\big(\frac{\omega}{\omega_0} - \frac{\omega_0}{\omega}\big) = \frac{1}{C\Delta\tilde{\omega}_c\omega_0} \times j\omega + \frac{\omega_0}{C\Delta\tilde{\omega}_c} \times \frac{1}{j\omega} \tag{4.5}$$

Consequently, the capacitance has to be replaced by an LC-series with $\tilde{L} = \frac{1}{C\Delta\omega_0\tilde{\omega}_c}$ and $\tilde{C} = \frac{C\Delta\tilde{\omega}_c}{\omega_0}$. Similarly, the inductance has to be replaced by an LC-parallel. Figure 4.3 illustrates this correspondence with the two lumped models of the filters. As a result, the stop-band filter is composed by two resonators centered around ω_0.

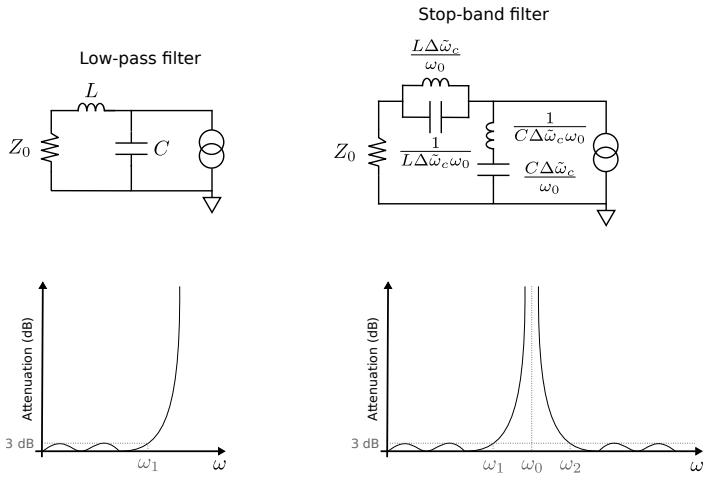

Figure 4.3: Transformation from a low-pass filter to a stop-band filter. Lumped models are represented at the top. Attenuation characteristic profiles of those prototypes are drawn below. For the example, here we have taken a Chebyshev 3 dB ripples filter.

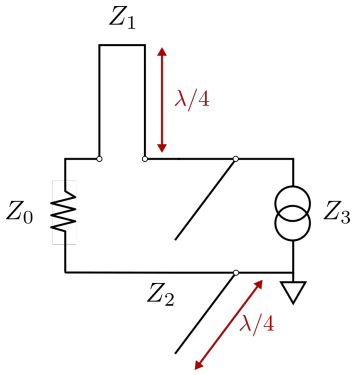

Figure 4.4: Circuit diagram of the stop-band filter composed of a $\lambda/4$ short-terminated stub in series connected to a $\lambda/4$ open-terminated stub in parallel.

Implementation with stubs In order to implement the stop-band filter of Figure 4.3 on our experiment chips with coplanar waveguides, we have to replace the LC-lumped resonator by waveguide sections. Indeed, to approximate ideal lumped elements, distributed elements such as open-circuited or short-circuited transmission line stubs[1] are frequently used. Moreover, the physical distance between distinct elements cannot be neglected at microwave frequencies. Kuroda's identities are an useful transformation to separate the equivalent components using transmission lines sections.

First, the Richard's transformation is used to transform a lumped element to a transmission line section. The core idea of this conversion is that the input impedance of the transmission line section must match the impedance of the initial lumped element at the cut-off frequency $\omega_1/2\pi$. Thus, the LC-parallel resonator can be replaced by a short-circuited series stub $\lambda/4$ resonant at ω_0. Its characteristic impedance is noted here Z_1. Likewise, the LC-series resonator is replaced by an open-circuited parallel stub $\lambda/4$ resonant at ω_0, with characteristic impedance noted Z_2. Our stop-band filter is now represented in Figure 4.4. In order for this stub-based model to be equivalent to its lumped model, the characteristics impedances are set to

$$\begin{aligned} Z_0 &= 50\ \Omega \\ Z_1 &= \frac{\omega_c L_1}{\tan(\frac{\pi}{2}\frac{\omega_1}{\omega_0})} = 25\ \Omega \\ Z_2 &= \frac{1}{\omega_1 C_2}\frac{1}{\tan(\frac{\pi}{2}\frac{\omega_1}{\omega_0})} = 169\ \Omega \\ Z_3 &= \infty\,. \end{aligned} \tag{4.6}$$

Second, we cannot implement a series stub in a coplanar waveguide design, so we have to transform the series stub into an equivalent component. Kuroda's identities illustrated in Figure 4.5 make the equivalence between a short-circuited series stub to an open-circuited parallel stub. Moreover, thanks to this transformation the stubs are physically separated by a transmission line section with a specific length and characteristic impedance. Thanks to these identities, we

[1] A stub is a portion of transmission line connected at one end only (in series or in parallel). The other extremity can be opened or shorted.

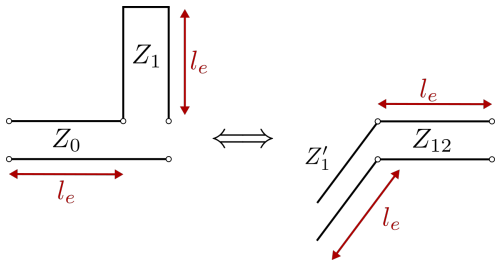

Figure 4.5: Illustration of two equivalent circuits linked by Kuroda's identities. All portions of transmission lines have the same electrical length l_e.

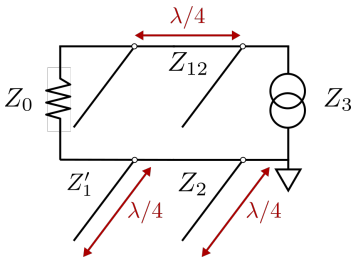

Figure 4.6: Circuit diagram of the stop-band filter composed of two $\lambda/4$ open-terminated stubs in parallel separated by a piece of transmission line of electrical length $\lambda/4$.

convert a line of impedance Z_0 connected to a series stub of impedance Z_1 into a parallel stub of impedance Z_1' connected to a $\lambda/4$ long line of impedance Z_{12}, such as

$$\begin{aligned} Z_1' &= Z_0(1 + \frac{Z_0}{Z_1}) \\ Z_{12} &= Z_0 + Z_1 \,. \end{aligned} \tag{4.7}$$

Eventually, the stop-band filter is shown in Figure 4.6, composed by three $\lambda/4$ resonators whose characteristic impedances are

$$\begin{aligned} Z_0 &= 50\ \Omega \quad \text{and} \quad Z_3 = \infty \\ Z_1' &= 149\ \Omega \\ Z_{12} &= 75\ \Omega \\ Z_2' &= Z_2 = 169\ \Omega \,. \end{aligned} \tag{4.8}$$

Coplanar waveguide implementation The obstacle for the coplanar waveguides implementation now lies in the high impedances required by equation (4.8). Indeed, a coplanar waveguide of high impedance must present a narrow central track and a large gap.
In practice, for reliable nanofabrication with laser lithography we are limited to characteristic sizes of about ~ 1 µm. In order to have a safety margin, we fix the minimal track width to 5 µm. Then, we fix the largest gap width to 100 µm. Indeed, the characteristic impedance increases in a logarithmic way with the size of the gap so we decide to stop at 100 µm for space optimization on the chip. Taking into account those dimensions and the dielectric constant of silicon (the

material of our chips, $\epsilon_r = 11.7$), we get a maximal characteristic impedance of $Z_{\max} = 120\ \Omega$. We now want to be convinced about the filter efficiency even if all impedances are limited to $Z_{\max}$. Electromagnetic power dissipating in the load impedance is the relevant quantity to consider for the filter efficiency. In the case of a single-terminated filter, the power flowing in the load-impedance is proportional to $\mathrm{Re}(Z_{\text{in}})$ where Z_{in} is the impedance seen from the port. Ideally, $\mathrm{Re}(Z_{\text{in}})$ should be $50\ \Omega$ outside the band and $0\ \Omega$ inside.
Hereafter, we detail on purpose the calculation of Z_{in} in order to help newcomers to understand the calculation process. For a $\lambda/4$ open-circuited stub of characteristic impedance Z and resonance frequency ω_0 the equivalent impedance is

$$Z'(\omega) = \frac{Z}{i\tan(\frac{\pi}{2}\frac{\omega}{\omega_0})}\,. \tag{4.9}$$

For $\lambda/4$ long transmission line with resonance frequency $\omega_0/2\pi$ and characteristic impedance Z, loaded at the end by an impedance Z_c the equivalent impedance is

$$Z'(\omega) = Z_c\frac{(Z + iZ_c\tan(\frac{\pi}{2}\frac{\omega}{\omega_0}))}{(Z_c + iZ\tan(\frac{\pi}{2}\frac{\omega}{\omega_0}))}\,. \tag{4.10}$$

Then, using equations (4.9) and (4.10), we can gradually calculate Z^0_{in}, Z^1_{in}, Z^2_{in} and Z_{in} as they are defined in Figure 4.7

$$\begin{cases} Z^0_{\text{in}} &= 50\ \Omega \\ Z^1_{\text{in}}(\omega) &= \frac{1}{Z^0_{\text{in}}+i\frac{\tan(\frac{\pi}{2}\frac{\omega}{\omega_0})}{Z_1}} \\ Z^2_{\text{in}}(\omega) &= Z_{12}\frac{(Z^1_{\text{in}}+iZ_{12}\tan(\frac{\pi}{2}\frac{\omega}{\omega_0}))}{(Z_{12}+iZ^1_{\text{in}}\tan(\frac{\pi}{2}\frac{\omega}{\omega_0}))} \\ Z_{\text{in}}(\omega) &= \frac{1}{Z^2_{\text{in}}+i\frac{\tan(\frac{\pi}{2}\frac{\omega}{\omega_0})}{Z_2}}\,. \end{cases} \tag{4.11}$$

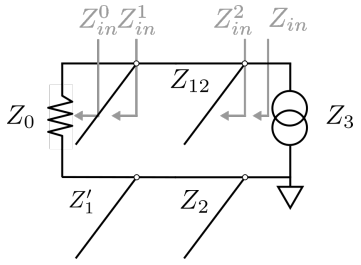

Figure 4.7: Circuit diagram of the stop-band filter with $\lambda/4$ parallel stubs connected with via a $\lambda/4$ portion of transmission line. This diagram is a calculation guide that corresponds to equation (4.11). The impedances seen from a circuit point are indicated with a grey arrow.

Figure 4.8 displays the real part of input impedance Z_{in} (see equation (4.11)) as a function of the frequency $\omega/2\pi$. It compares the ideal case with the parameters of equation 4.8 to the case where high impedances have been capped to $Z_{\max}$ value. In the restricted impedance case, the band is wider and the ripples around the band are less important but it is still an efficient filter for our requirements. Finally, these stubs define a two-port network and we will track the scattering parameter of this network along electromagnetic simulations. If we name port 1,

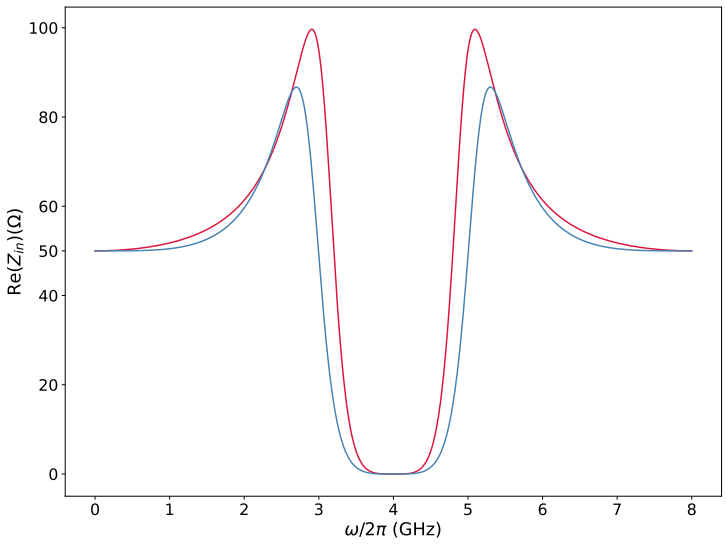

Figure 4.8: Real part of the impedance Z_{in} of the stop-band filter as a function of the waves frequencies. Red line is plotted for values: $Z_0 = 50\ \Omega$, $Z_1 = 149\ \Omega$, $Z_{12} = 75\ \Omega$, $Z_2 = 169\ \Omega$ (theoretical values for the filter design, see (4.8)). Blue line is plotted for values: $Z_0 = 50\ \Omega$, $Z_1 = 120\ \Omega$, $Z_{12} = 75\ \Omega$, $Z_2 = 120\ \Omega$ (the impedances have been restricted to $Z_{\max}$ for coplanar waveguide implementation).

respectively port 2, the ports on both sides of the stubs, for any pulsation ω we get

$$S_{11}(\omega) = \frac{Z_0 - Z_{\text{in}}(\omega)}{Z_0 + Z_{\text{in}}(\omega)} \quad \text{and } |S_{21}|(\omega) = \sqrt{1 - |S_{11}(\omega)|}\,. \tag{4.12}$$

Figure 4.11 uses the formula (4.12) to compare the S_{21} amplitude of the lumped model to the 3D-finite elements simulated model, and to the experimental test.

1.3 Microwave simulations

To tune the filters architecture we use a 3D-electromagnetic finite element simulation tool, High Frequency Structure Simulator (HFSS), of ANSYS Electromagnetics Suite. We proceed step by step from the lumped model towards a stub design while taking the chip dimensions constrains into account. Since simulating the whole 3D structure of a portion of coplanar transmission line is demanding in terms of memory and computation resources, we focus on the relevant parts of the chip. This strategy is time-saving and is based on a simulation technique halfway between a lumped model and a 3D distributed model. We precisely describe all this method in the Appendix A with a view of being a guideline for interested readers wishing to reproduce this method.

We converge on the architecture presented in Figure 4.9. Figure 4.11 displays the amplitude of the scattering parameter S_{21} extracted from the numerical simulation of the 3D model of Figure 4.9 (ports 1 and 2 are defined in this figure).

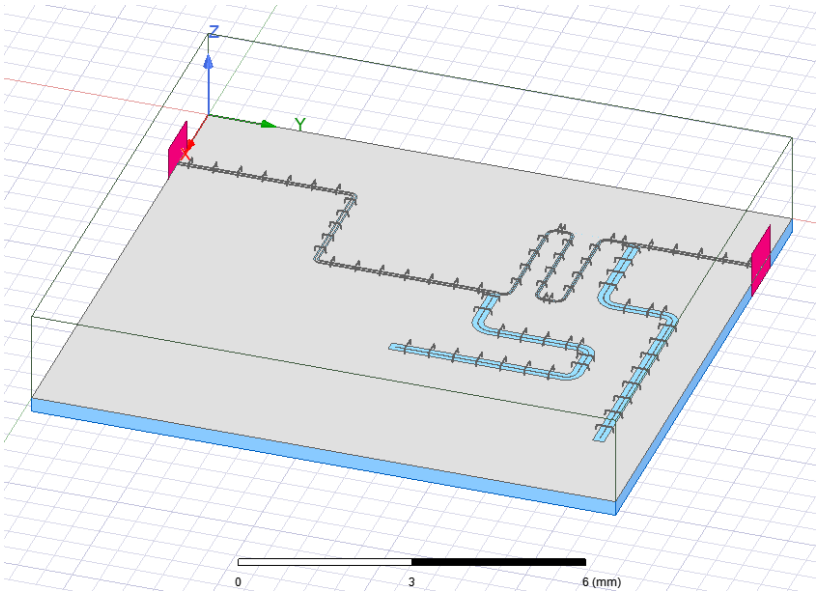

Figure 4.9: Screenshot of the HFSS 3D model of the stop-band filter architecture designed to fit inside the real chip. The silicon chip is in blue, the perfect conductor surface modeling superconducting metal (niobium) is in grey. Bonds are in dark grey. The model is closed on the top with a box filled with air, whose borders are depicted with black lines. The wave ports are in red and are named port 1 and port 2.

1.4 Measurement of the filter

Once the design has been validated by numerical simulations, we nanofabricate the filtering element on a chip in order to measure its scattering parameters. The chip device is shown in Figure 4.10. The remaining space on the chip is used to test another microwave element (on-chip bias tee, see Section 2). The chip is mounted in a sample holder "JAWS" [85] and cooled down in an Helium fridge (we are not interested in probing any quantum effect, we simply need to be at low enough temperatures for the niobium to be superconducting).
The calculated scattering parameter from the lumped model, the scattering parameter simulated from the real geometry simulated in HFSS 3D model (Figure 4.9), and the measured scattering parameter of the fabricated chip are compared in Figure 4.11. The main difference between the measured and simulated data is the duplication of the central off-peak. Indeed, due to the fabrication the two parallel stubs cannot be rigorously identical and this is why there is a small discrepancy on their resonance frequency. Yet, the impact on the filtering performances is limited and this measurement confirms the adequate filtering by the stubs.

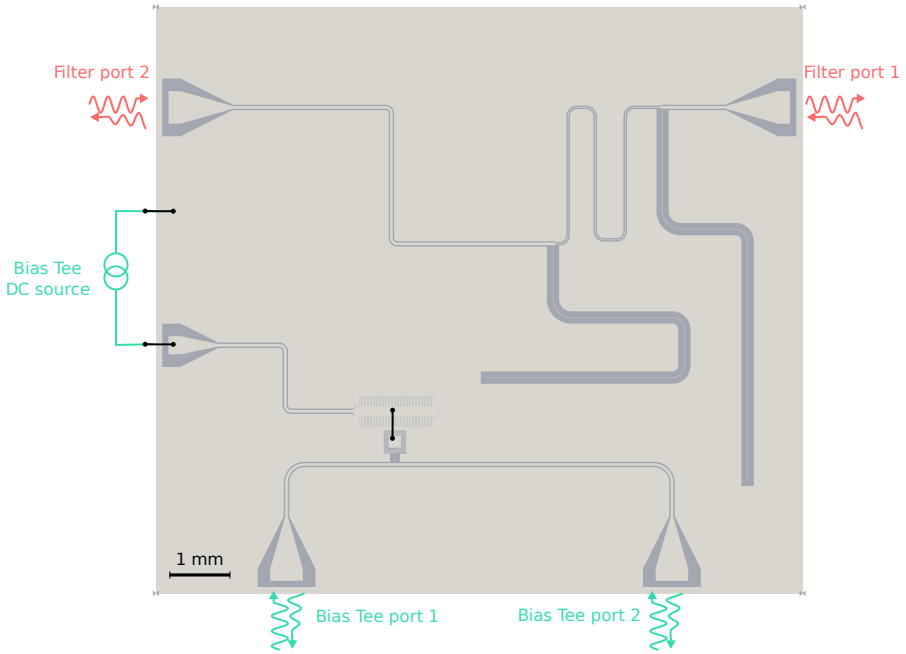

Figure 4.10: Graphic presentation of the chip used for testing the stop-band filter. It is based on the drawing file that was used to pattern the circuit with laser lithography. Blue represents silicon. Grey represents niobium. Bonds are signaled with black lines. This chip is intended for testing two distinct on-chip electromagnetic components. The top part of the chip is dedicated to testing stop-band filter: the red waves signal the two RF-ports. The bottom part is dedicated to testing on-chip bias tee: the green waves signals the two RF-ports, the green straight line represents the DC connection.

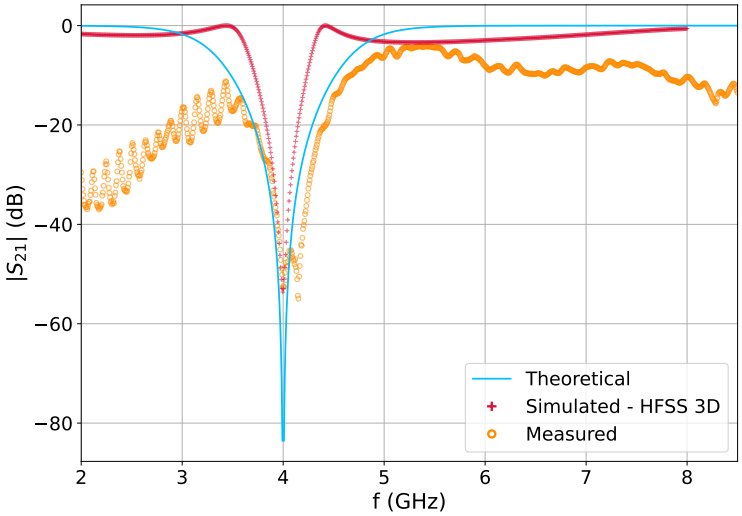

Figure 4.11: Comparison of the analytical, simulated, and measured amplitude of scattering parameter S_{21} as function of frequency of the two-port network made by the stubs. Blue line is the analytical amplitude from the lumped diagram (see (4.12)), red dots mark the simulation result of the chip with HFSS 3D model (see Figure 4.9), orange dots mark the measured scattering parameter (see chip of Figure 4.10).

2 Designing an on-chip bias tee

2.1 Introduction and objectives

We recall from Chapter 2 that the ATS has to be biased in flux by DC currents at a specific operating point to activate the two-photon interaction regime (see Subsection 1.5 of Chapter 2). Besides, the RF pump tone required for the two-photon conversion propagates with opposite phase trough the arms on both sides of the buffer: it induces common flux when reaching the ATS. Finally, the buffer mode is driven by waves propagating in phase trough the arms of the feedline. Accordingly, a component is required on both arms in order to jointly route the DC currents and the RF excitations towards the buffer. This section presents the construction of an on-chip bias tee, a three-port network dedicated to combine DC current and RF waves. As specified in Figure 2.3, we place the on-chip bias tees on both arms of the buffer and we collect back the current on the two sides of the chip. This defines two independent paths for the current on the chip in order to separately address the left and right loops of the ATS. Then, varying independently common and differential flux (φ_Σ, φ_Δ), we can explore the whole potential landscape of the ATS (see equation (2.5)) as proven by the measured buffer frequency flux maps in Figure 2.4.
As shown in Figure 4.12, a bias tee can be seen as a capacitor on RF port blocking low-frequency signal (with C being the capacitance, the dipole impedance is: $Z(\omega) = \frac{1}{jC\omega} \to 0$ for high ω) and an inductor blocking high-frequency signal on the DC port (with L being the inductance, the dipole impedance is: $Z(\omega) = jL\omega \to 0$ for low ω) [86].

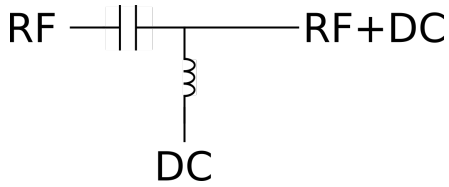

Figure 4.12: Lumped model of a bias tee. The Radio-Frequency (RF) port has a capacitor in order to block continuous signal. The Direct Current (DC) port has an inductance in order to block RF signal.

Requirements specification We want to drive and probe the buffer via the RF compatible branches of the bias tee, so we need to minimize the losses of RF signal going through the bias tee. Thus, the most important criteria is to avoid RF signal coming out from the buffer (that is to say coming from the RF+DC port) leaking to the DC port. Conversely, in this case it is not significant if some DC current leaks the towards RF port so we decide not to add a capacitance on the RF port in this first design.
The ports are named as referred in Figure 4.12. In terms of scattering parameters, we want for

$\omega/2\pi$ in the usual frequency range (2 to 8 GHz):

$$\begin{aligned} &S_{\text{RF+DC, RF}}(\omega) = S_{\text{RF, RF+DC}}(\omega) = 1, \\ &\text{which directly implies (due to energy conservation)} \\ &|S_{\text{RF+DC, DC}}(\omega)| = |S_{\text{RF+DC, RF+DC}}(\omega)| = |S_{\text{RF, RF}}(\omega)| = |S_{\text{RF, DC}}(\omega)| = 0. \end{aligned} \tag{4.13}$$

To sum up, the key idea is that our bias tee should allow a way for DC current while being invisible in terms of RF transmission in the buffer feedline.

2.2 Electromagnetic design and microwave simulations

We start working with the lumped model before implementing it in a 3D on-chip geometry. Next, we compare the 3D model and the lumped model RF-characteristics using the 3D finite element electromagnetic simulation tool HFSS.

Lumped model To design the bias tee we start from the lumped model of Figure 4.12. Since we do not care about possible DC current leaking towards the RF port, we can remove the capacitor and concentrate our efforts on the DC port branch. An intuitive way of thinking the design of the bias tee is exposed in Figure 4.13. The goal is to adapt the impedance $Z(\omega)$ of the DC branch in order to get: $Z(\omega) \gg 50\ \Omega$ for $\omega/2\pi$ in the RF-range and $Z(\omega) \ll 50\ \Omega$ for $\omega/2\pi$ in the DC-range.

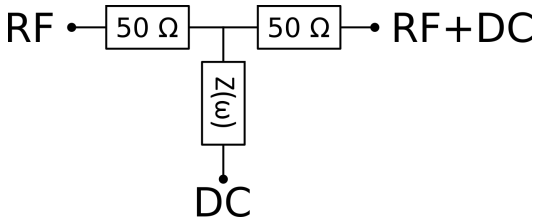

Figure 4.13: Lumped model of the bias tee we want to design.

Inductance design The first idea is to put an inductive element in the DC branch as in the prototype of Figure 4.12. The constrain $Z(\omega) \gg 50\ \Omega$ for $\omega/2\pi$ in the GHz range implies a target inductance value of about 10 nH.
In order to make an on-chip inductive element with limited spatial extension, we devise a square spiral inductor with a large central pad to connect it to the rest of the DC branch using an aluminium bond.
According to [87], the design exposed in Figure 4.16 should give an inductance of $L \approx 1.1 \times 10^{-8}$ H. Comparing the scattering parameters extracted from a lumped model and a 3D finite element simulation confirms the inductive value of the on-chip component (see Figure 4.14). However, Figure 4.14 also reveals an undesirable remaining attenuation on frequency range 2-8 GHz. To decrease this unwanted attenuation, we would need a really higher inductance value which would not be achievable on-chip with coplanar architecture.

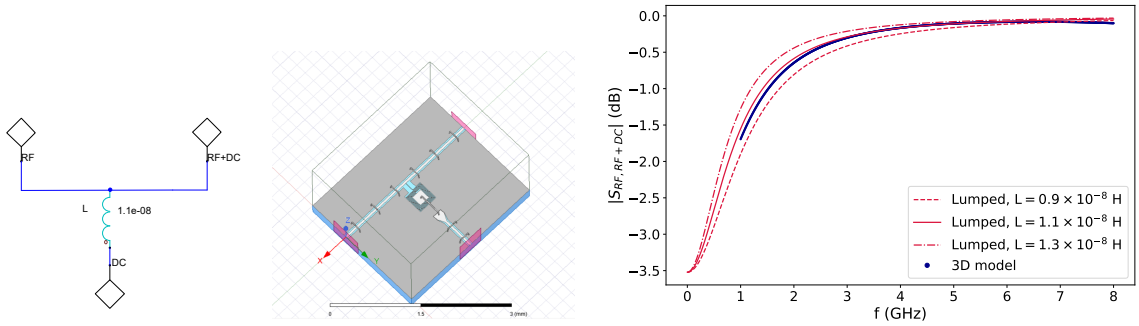

(a) (b) (c)

Figure 4.14: Simulation of the bias tee with an inductor. (a) Lumped circuit diagram simulated in Ansys Electronic Desktop (see Appendix A for more details on lumped element simulation) (b) On-chip bias tee with an inductor simulated using HFSS 3D model. Grey is the superconducting metal, blue is the dielectric chip in silicon, red represents the wave ports for the simulation. Note that our bias tee is symmetrical and RF+DC, RF ports can commute. (c) Results of scattering parameter $S_{\mathrm{RF+DC,RF+DC}}$ as function of frequency, simulated in lumped model and in 3D model. Blue dots are the result of 3D simulation exposed in (b). Red lines are the results of lumped simulation displayed in (a) with different values of inductance. The solid line corresponds to $L = 1.1 \times 10^{-8}$ H, the dashed (respectively dashed-dotted) line gives a confidence interval and correspond to $L = 0.9 \times 10^{-8}$ H, respectively $L = 1.3 \times 10^{-8}$ H.

Capacitance design To enhance the effect of cutting out high frequencies we add a parallel capacitor to ground as displayed in Figure 4.15 (a). The lumped model simulations give us an order of magnitude of the required capacitance value ($C \sim 10^{-12}$ F). We now have to implement such a capacitor in coplanar geometry.

In order to minimize the space required on the chip while maximizing the capacitance, we design an interdigitated capacitance. The central part of the capacitance should be large enough to be connected to the inductor via an aluminium bond. We can have a first rough estimation of the capacitance value using a coplanar capacitance calculator[2] and estimating the facing surfaces dimensions. Figure 4.16 displays the dimensions of the final design on which we have converged after several trials (Figure 2.1 of Chapter 2 shows an optical micrograph view of this component fabricated on the experiment device). By comparing the simulated 3D geometry and the lumped model scattering parameters, we can estimate the capacitance value to C $\approx 2 \times 10^{-12}$ F (see 4.15). Moreover, Figure 4.15 (c) confirms the reduced attenuation imposed by this design on the frequency range 2-8 GHz, which validates this approach. In addition, we also compare the leaking of RF waves travelling in the bias-tee through the DC port in Figure 4.17. We can observe that the capacitance is also useful to prevent those leaks.

[2]https://www.emisoftware.com/calculator/coplanar-capacitance

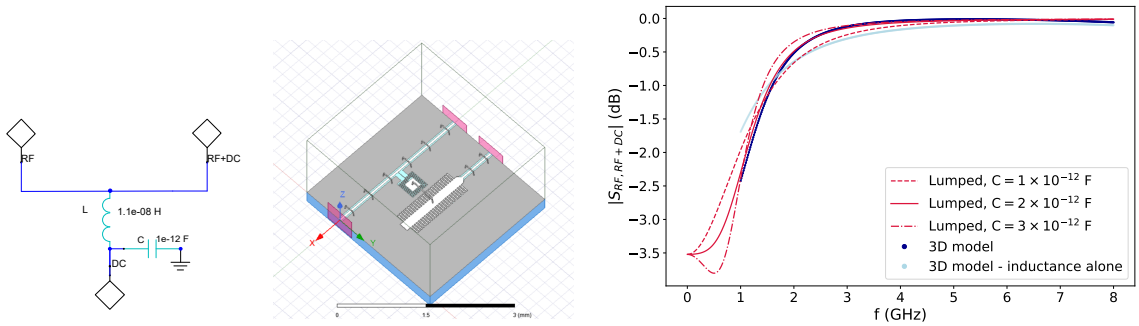

(a) (b) (c)

Figure 4.15: Simulation of the bias tee with an inductor and a parallel capacitor. (a) Lumped circuit diagram simulated in Ansys Electronic Desktop. (b) On-chip bias tee with an inductor and the parallel capacitor simulated using a HFSS 3D model. Grey is the superconducting metal, blue is the dielectric chip in silicon, red represents the wave ports for simulation. (c) Results of scattering parameter $S_{\mathrm{RF+DC,RF+DC}}$ as function of frequency, simulated in lumped model and in 3D model. Blue dots are the result of 3D simulation exposed in (b). Light blue dots are the result of 3D simulation with inductance alone to give some comparison. Red lines are the results of lumped simulation (screenshot in (a)) with different values of capacitance. The solid line is plotted with $C = 2 \times 10^{-12}$ F, the dashed (respectively dashed-dotted) line gives a confidence interval and correspond to $C = 1 \times 10^{-12}$ F, respectively $C = 3 \times 10^{-12}$ F.

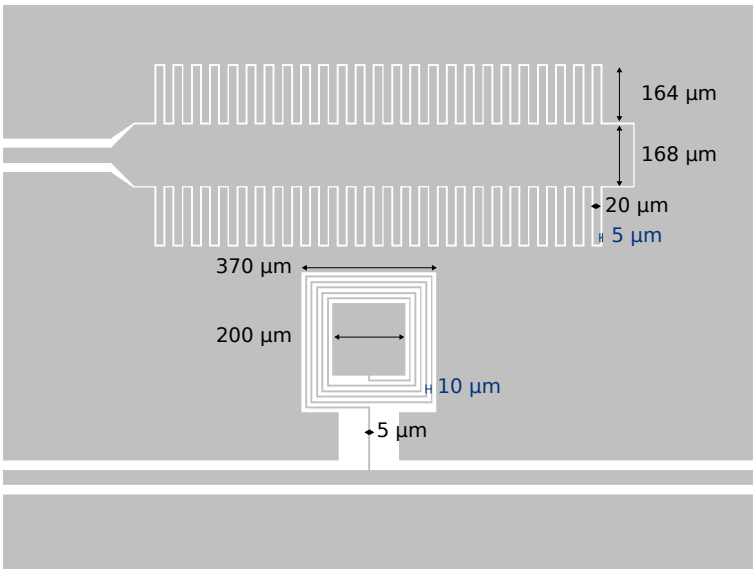

Figure 4.16: Dimensions of the coplanar implementation of the bias tee. Grey symbolises the superconducting metal (niobium in our case), white is the dielectric material (silicon in our case). Dimensions annotated in black are superconducting tracks dimensions. Dimensions in blue are related to gaps. In the interdigitated capacitance there are 25 fingers of 20 µm width, separated by a gap of 5 µm. The inductance is winding 6 times around the central plate with a 5 µm width wire, spaced by gap of 10 µm. An aluminium bond (not represented here) has to connect the central pad of the coil to the central pad of the capacitance. Figure 2.1 of Chapter 2 presents an optical micrograph view of this component fabricated on the experiment device.

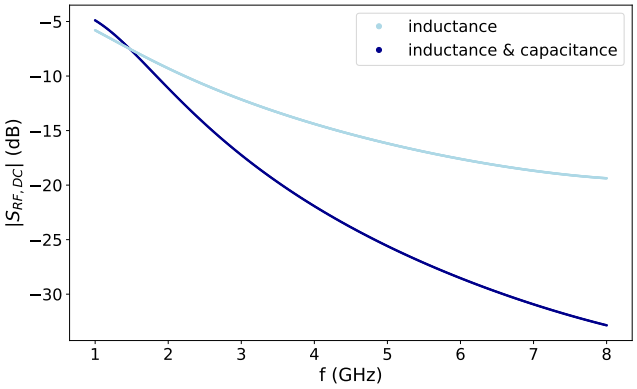

Figure 4.17: Comparison of simulated scattering parameter $S_{\mathrm{RF,DC}}$ of the bias tee with and without the parallel capacitor. $S_{\mathrm{RF,DC}}$ is given as function of frequency simulated in 3D model. Light blue dots are in the case of bias tee with inductance alone (see Figure 4.14). Dark blue dots are in the case of bias tee with inductance and parallel capacitance (see Figure 4.15). Since the bias tee ports RF+DC and RF are symmetric, looking at scattering parameter $S_{\mathrm{RF,DC}}$ is equivalent to looking at $S_{\mathrm{RF+DC,DC}}$.

2.3 Measurement of a test device

Similarly to the previous section (Section 1), we want to test an on-chip design of the bias tee in order to validate the electromagnetic simulations. The design of the chip for the test is presented in Figure 4.10. Figure 4.18 exposes the measurement results of the scattering parameter between the RF and RF+DC port. We can notice the discrepancy between the electromagnetics simulation and the measurement. This could be explained by the small dimensions of the elements (coil, capacitance) requiring a lot of meshing points in 3D finite elements simulation to be more precise but becoming then out of reach for the computer performance. This demonstrates the importance of keeping a critical thinking on electromagnetic simulation results. Finally, we can see that in a range of frequencies from 3.5 GHz to 8 GHz the bias tee implies very few attenuation on the RF line, which validates this on-chip component.
In this first implementation, the possible leaks of DC currents through the RF port were not a primary requirement. As a result, no capacitance is implemented in the RF port. In the next implementation, an improvement could consist in integrating a capacitance in this port. This could simply be a discontinuity in the feedline coplanar waveguide (a thin strip of ground plane crossing the central track) preventing the remaining DC currents from leaking out through the RF port.

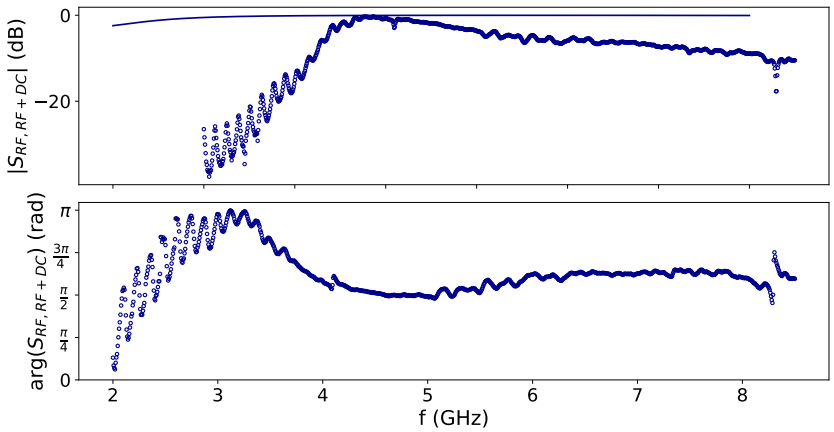

Figure 4.18: Measured scattering parameter between the RF and RF+DC ports of the bias tee as a function of the frequency. Top plot is the amplitude in dB. Bottom plot is the phase in radians. Circles are data measurement. Solid line is the result of the 3D electromagnetic simulation.

Chapter 5

Nanofabrication

Contents

Résumé en français

Le circuit présenté dans ce manuscrit de thèse est composé de structures de guides d'ondes coplanaires et de jonctions de Josephson. La fabrication de ces éléments était partie intégrante de ce travail de thèse et a été réalisée dans les salles blanches de l'ENS et du Collège de France. Le circuit de l'expérience de l'oscillateur à deux photons, décrit dans le Chapitre 2, est le fruit d'itérations successives qui ont intégré les différentes fonctionnalités de manière incrémentale. Au cours de ces cycles de fabrication, des variations du procédé de fabrication ont été réalisées dans des buts d'optimisation.

Ce chapitre se concentre sur la nanofabrication et propose une revue de différents procédés possibles. La première section détaille les techniques et protocoles pour fabriquer un circuit supraconducteur en salle blanche. La seconde section est axée sur la fabrication des jonctions de Josephson et sur les différentes difficultés pouvant être rencontrées au cours de la fabrication de ces éléments. Ce chapitre est détaillé de manière à servir de guide introductif pour la nanofabrication.

The sample presented in this manuscript is composed of coplanar wave-guide structures and Josephson junctions. Their fabrication was part of my thesis work, which was performed in the clean room at ENS and at Collège de France. The main device of the two-photon dissipative oscillator is the result of successive iterations implementing the features in an incremental way. I fabricated various devices during this thesis work: nanofabrication stands for a significant part of my work during this PhD project. During these consecutive rounds of fabrication, different variations of fabrication processes were tested for optimization purpose. This chapter focuses on the nanofabrication of coplanar waveguide structures and Josephson junctions. The first section details the recipe techniques to fabricate a superconducting chip in the clean room. The second section discusses about issues I encountered in the Josephson junctions' fabrication process, and techniques I developed to circumvent those. This chapter is intended to provide enough detail to serve as a useful guide for readers interested in beginning nanofabrication.

1 Device fabrication

This section presents the steps of the nanofabrication starting with a bare silicon wafer up to a mounted chip in a sample holder ready to be cooled down and measured. This recipe was modified thanks to the investigation of Section 2. Here we present the final recipe that was used to fabricate both chips presented in Chapter 2 and 3. Appendix B contains a more detailed recipe.

1.1 Wafer preparation

We start with a 2-inch intrinsic silicon wafer with a 280 µm thickness and a resistivity larger than 10 kΩcm. We load it into the sputterer to deposit 120 nm of niobium (Nb).
In order to be able to circumvent small variations inherent to nanofabrication process, we fabricate twelve 10 x 11 mm chips on the same wafer. We separate the individual chips at the end of the process and select the sample that is best suited for the experiment.

Cleanliness of the wafer At the beginning of the fabrication process, caution must be taken to ensure that the wafer is really clean. Examining the wafer with an optical microscope in dark field mode is a good practice to spot some potential imperfections.

1.2 Circuit patterning

We pattern the large features of the circuit (> 5 µm) using laser lithography.

Spinning resist We pattern the circuit using positive resist. We spin-coat S1805 resist on the wafer and bake it for 1 min at 115°C.

Laser lithography We use a laser lithography writing machine to draw the circuit patterns with a dose of 203mJ/cm^2.

Development We develop the chip in MF319 for 1 min, then rinse it in deionized water for 1 min. In order to solve the exposed resist more homogeneously, we shake the beaker by a soft rotation. At the end of this step, it is recommended to visually check that lithography was correct with a yellow light optical microscope[1].

Reactive Ion Etching This step is dedicated to take off the niobium located on the unprotected parts of the resist mask. The wafer is etched in a reactive ion etching (RIE) machine with a SF6 plasma and a 10 s overetch.

Lift-off and final cleaning The remaining resist on the wafer has now to be lifted-off. We first put the wafer in a beaker of acetone at 50°C with sonication for 5 min. Next, we assume that the acetone is saturated in dissolved resist, so the wafer is sonicated in a second bath of acetone at 50°C for 20 min. We finally rinse in IPA and blow dry with N_2 gun.
At the end of the process, we perform 20 s of O_2 stripping to be sure to remove all residual organic contaminants.

1.3 Josephson junctions fabrication

Due to issues encountered while attempting to fabricate the two-photon dissipative oscillator chip, the recipe below results from an investigation based on a literature review and experimental tests. For clarity purpose, we present here the final recipe that was used for fabricating the chips of Chapter 2 and 3. Then, the next section is dedicated to the discussion on the various recipe processes.

Junction patterning Our Josephson junctions are fabricated from Dolan bridges patterned with electron beam (e-beam) lithography. We spin two layers of resist: first, methacrylic acid/methyl methacrylate (MAA EL13) baked for 3 min at 185 °C and second, poly(methyl methacrylate) (PMMA A3) baked for 30 min at 185 °C. The patterning with SEM lithography is written with a beam aperture of 7.5 µm, a beam voltage of 20 kV and a dose of 283 µAs/cm^2. Once the e-beam patterning completed, we develop in a IPA:H_2O (3:1) bath at 6 °C for 2 min, rinse for 10 s in IPA and blow dry. The development step conditions the exact 3D dimensions of the resist bridges. Thus, the operator should take care to be really consistent for this step (e.g. holding and shaking the chip in the developer in the same way every time). Finally, residual organic contaminants below the bridges are stripped by an O_2 plasma for 10 s. This cleaning step prior to evaporation was investigated (see Section 2).

Junction deposition Secondly, the wafer is introduced in an e-beam evaporator. We start with a 2 min argon milling step at an angle of ± 30° to prepare for a good electrical contact with the niobium layer. We deposit two layers of aluminium (35 nm then 70 nm thick) at an

[1]This step must be done in the resist room with a yellow light microscope in order to avoid to expose the resist that should stay unexposed.

angle of ± 30°, separated by a static oxidation in a pure O_2 atmosphere at 10 mbar for 10 min. Before venting to air, the chamber is filled with 300 mbar of O_2 for 5 min.

Lift-off and cleaning We lift-off in a 50 °C acetone bath for 1 h. We use a pipette to flow some acetone on the chip to help the removal of resist and aluminium foil. Then, we transfer the wafer to a new acetone bath for 5 min and sonicate for 10 s at very low power to ensure that small aluminium residues are removed without damaging the junction structure. Eventually, the wafer is rinsed in IPA and blown dry with N_2 gun.

1.4 Selecting the chip and mounting the sample

We select the most favorable chip of the wafer and prepare it for the experiment at the end of the fabrication process.

Selection and verification process First we check at the optical microscope the visual aspect of all the coplanar waveguide lines. Second, we should pick the sample with the Josephson energies values suiting the best for the experiment (see Subsection 2.1). We evaluate the Josephson energy of the test junctions fabricated on each sample. We measure the room temperature resistance of the Josephson junction at the probe station and deduce the Josephson coupling energy thanks to the Ambegaokar-Baratof formula [43].

Dicing The samples are protected against dust produced by the dicing thanks to a PMMA resist layer spun and baked for 1 min at 185°C (the baking time is reduced in order to minimize junction ageing due to heating, see next section). Then, the wafer is diced face up in an automated dicing machine.

Cleaning This is the last cleaning step before cooling down of the sample for measurement. We first clean the protective resist layer by flowing deionized water on the sample, since we believe it can remove the small dusts due to dicing. We next pour the sample in two successive bathes of acetone at 50°C. At this step, we do not turn on the sonication in order to avoid breaking the junctions on the sample. Finally, we rinse in IPA and blow-dry with a N_2 gun and perform a 10 s O_2 stripping step in order to be sure to remove all organic residues.

Mounting on the sample holder The chips of this thesis work were measured in the sample holder developed in the ENS group called "JAWS" [85]. A good practice when renewing the chip in the sample holder is to clean the holder itself. It is opened, poured in acetone bath at room temperature, scrubbed with clean room cotton buds, rinsed in IPA and dried. The chip is glued inside the sample holder, in the center of the dedicated Printed Circuit Board (PCB). Finally, we have to proceed to microbonding to connect all parts of the ground plane on the chip and to connect the device electrodes to their respective PCB lines.

2 Focus on the Josephson junctions fabrication

This section focuses on the fabrication process of Josephson junctions. We start by presenting the junctions of the device of the two-photon oscillator experiment device (described in Chapter 2) and the issues in the fabrication process that had to be overcome before fabricating this chip. We present a bibliographical overview of fabrication protocols of different groups working with superconducting circuits. Based on this comparative study, we test various fabrication processes in the ENS and Collège de France clean rooms. Even though we were unable to draw clear conclusions from this experimental study, it allowed us to step back from the pre-existing group recipe and to derive a new one. This hindsight can be beneficial for newcomers in nanofabrication, which is why we chose to detail this investigation in this manuscript.

2.1 Junctions of the ATS

In the two-photon dissipative oscillator experiment, the ATS is the central element to mediate the two-photon interaction for the memory resonator. The ATS is formed by two Josephson junctions in a loop split in its center by an inductance made of an array of five junctions. Figure 5.1 depicts the different junctions composing the ATS. The junctions of the loop have a Josephson energy of $E_J/h = 37$ GHz and should be as symmetric as possible. The central array has an inductive energy of $E_L/h =$ 62 GHz. Ideally, all junctions in a junction array inductance should have the same junction energy and thus the same area. Figure 5.1 shows that this is not the case in our experiment, and while this could be improved in the next fabrication iteration, it is not detrimental to the experiment.
We remind from Chapter 2 that E_J value linearly tunes the two-photon coupling factor g_2 (equation (2.17)), thereby setting the value of the two-photon exchange rate κ_2. We want to keep g_2 as high as possible staying in the limit of $g_2 \ll \kappa_b$. Moreover, the E_L value directly tunes the frequency of the buffer mode (equation (2.23)) which is a constrained parameter. First, the presence of stop-band filters around the memory frequency (see Chapter 4) results in a lower bound limit. Second, in order to maintain a decent value of hybridization factor between the memory and the buffer modes, the buffer frequency should not be too far away from the memory frequency. As a conclusion, the values of the junction energy are constrained so it is even more critical to have a good repeatability in junction fabrication.

Critical current density The critical current density is a good number to monitor as a sanity check for our junctions. It is calculated by dividing the critical current value I_c by the area of the junction S. I_c is directly related to the Josephson coupling energy [43] which is obtained by measuring the room temperature resistance with the probe station. The S area is determined by observing the junction with a Scanning Electron Microscope (SEM) or an Atomic Force Microscope (AFM).
This value should be a constant for junctions of varying dimensions and for distinct fabrication batches. In our thesis work, this number is around 450 nA/ µm^2.

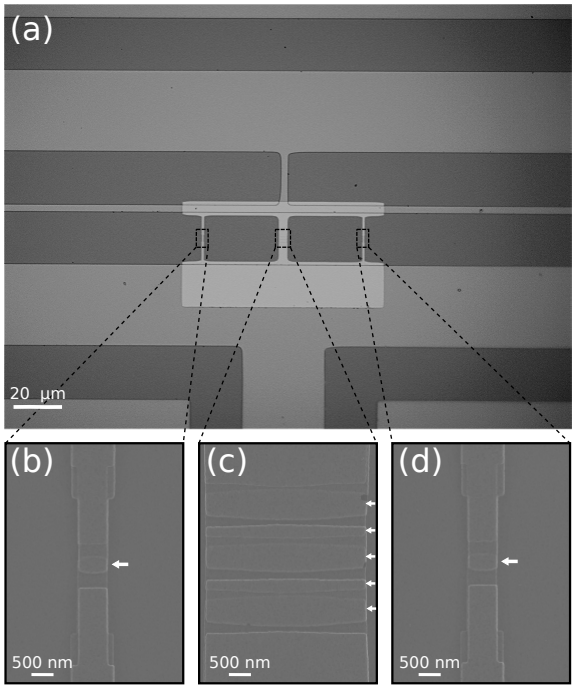

Figure 5.1: (a) Optical micrograph of the asymmetrically threaded SQUID (ATS) made of aluminium (light grey) deposited on the niobium circuit (grey) over a silicon substrate (dark grey). (b-d) Scanning electron microscope images of the small single junctions (b,d) forming the SQUID loop and the five array junctions (c) forming the inductive shunt. The small junctions are 275 nm × 700 nm. The array junctions, which would ideally all be equal in area, are in fact composed of three 600 nm × 3.9 µm and two 270 nm × 3.9 µm junctions. This results in a critical current density of about 450 nA/µm^2. For clarity, small arrows point to the location of each junction.

2.2 Investigation for better repeatability in junctions fabrication process

2.2.1 Unexpected variability with same fabrication process

We encountered issues with Josephson junctions fabrication on a global 2-3 months timescale in our first attempts to fabricate the chip presented in this thesis work. Junctions had already been fabricated in previous fabrication cycles with nothing unusual noted. On the contrary, during this period, the junctions fabricated on tests chips presented unexpectedly high variability for the same experimental fabrication parameters. Furthermore, the critical current density was unusually high. We were employing the ENS group's shared recipe at the time, which is similar to the recipe described in this manuscript with some differences implemented thanks to the investigation discussed below.

Observation of irregular junctions Examining the junctions made during this time period with a Scanning Electronic Microscope revealed that they were unusually dirty. Figure 5.2 compares a previously fabricated junction (with nothing particular to note) to an irregular junction. Those two junctions were fabricated using the same recipe. Yet, Figure 5.2 displays

unexpected sprinkled-like dust on the abnormal junction, which is a marker of fabrication issues. Moreover, we assumed that this contamination issue was related to the non-repeatability of the targeted Josephson inductance. As a result, we decided to investigate on the fabrication recipe in order to get rid of the source of contamination.

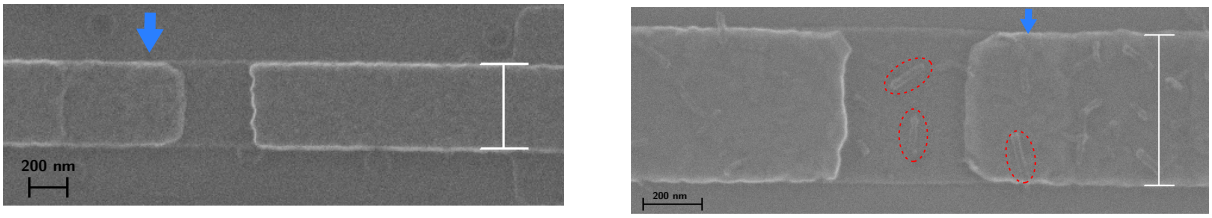

Figure 5.2: Comparison of SEM images of junctions on a test chip made with the same recipe and parameters. Left: "normal" junction, with no issues made on September 2020. Right: irregular junction with cleanliness issues made on February 2021. The two junctions are fabricated with a bridge width of 400 nm. For clarity, blue arrows point to the location of each junction. The red dashed lines are circling examples of anomalous sprinkled-like dust. The white bar corresponds to a measurement of the junction width : $w = 451$ nm on the left, $w = 510$ nm on the right.

2.2.2 Literature review

We collect the recipe fabrication techniques from groups that work with superconducting qubits. Table 5.1 summarizes the current state of the art for fabricating Josephson junctions. We indicate as a reference point in the table the previous ENS group recipe process. This table is commented in the following paragraphs.

Types of junctions In the review, we encounter various junction styles but the fabrication principle remains the same: patterning a resist structure in order to evaporate one electrode of aluminium, oxidize it, and build another electrode of aluminium with an overlay with the first layer and the oxide barrier. Thus comparing the various recipes is still relevant. The junction style differs by the configuration of the two aluminium electrodes in space. In the Dolan style, for instance, the two electrodes are parallel, whereas in the Manhattan style, they are orthogonal. Some groups are performing Dolan bridges using bandage patches. First, they pattern the resist structure and evaporate metal only in the limited spot of the junctions. Second, they open windows in the resist structure and evaporate metal to connect the junctions to the rest of the circuit. This technique allows the cleaning steps (especially argon milling) to be differentiated in order to have a clean junction and a good contact with the rest of the circuit. The main drawback of this technique is that it adds a full cycle of lithography/evaporation and increases the risk of undesirable nanofabrication errors.

O_2 stripping after development A lot of groups perform a O_2 stripping cleaning step after development. This step belongs to the plasma cleaning methods, with a plasma made out of O_2 gas. Due to the nature of the process it is also called O_2 ashing. This method is really

effective at removing organic contaminants from the sample since the high energy of the plasma is very efficient at breaking chemical bondings in organic contaminants. Plus, oxygen species are created in the plasma (for instance: O^+, O^-,...) and they can react with organic contaminants to form low molecular weight hydrocarbons. Thanks to their high vapor pressure these molecules are evacuated from the load-lock during the cleaning process [88]. The main drawback of O_2 plasma cleaning is due to the material that composes the chip. Indeed, exposing silicon to O_2 plasma causes the growth of silicon oxide SiO_2 layer on the Si layer, which alters the dielectric's electromagnetic properties. A measurement performed in ENS clean room was quite reassuring about the use of O_2 plasma on silicon chips. On a bare silicon wafer, 15 min of exposure to plasma O_2 (which is a quasi-infinite cleaning time) results in the growth of a 3 nm thick SiO_2 layer that is still negligible in comparison to the Si thickness (280 µm).

Argon milling This step is performed before evaporation to clean the surface where the metal will be deposited. It belongs to ion milling cleaning methods. Ion milling is a technique that involves accelerating ions of an inert gas (typically argon) from a wide beam ion source into the surface of a substrate in vacuum to remove material from the surface The term "ionic sandblasting" is a relevant name to describe this technique[89].

Lift-off In the previous ENS group recipe, the lift-off time (few minutes) is extremely short in comparison to the duration of other groups' recipes (few hours). Moreover, some groups are concluding the lift-off with a brief ultrasonic bath. After testing with low power ultrasonication, it appears that it is not breaking the junctions and we believe that it can help in the dissolution of any remaining aluminium residues.

Stabilizing the junctions Some groups are performing a final step to stabilize the junction and to counteract the effect of junction aging. When the junction is left at room temperature in ambient air, it ages and the Josephson coupling energy decreases over time. This aging is known to be caused by two phenomena: either the diffusion of oxygen atoms from the oxide barrier to the aluminium electrodes, or absorption of unwanted atoms or molecules into the barrier [90, 91]. To saturate this ageing process, we can heat the junction for a certain time or perform a long time O_2 stripping. Saturating the ageing process helps to be more systematic so it seems to be a good sanity process for better repeatability.

Group & reference	**Type**	**Spinning resist**	**Development**	**O_2 stripping**	**Ar milling**	**Oxidation**	**Lift-off**	**Additional step**
Houck lab Princeton University [92]	Dolan bridges	MAA 2 min @ 175°C PMMA 30 min @ 175°C	MIBK:IPA 1:3 Rinse IPA	P = 0.5 mbar t = 2 min Power = 200 W	V = 400 V 45 s / angle	O_2/Ar 85%/15% P = 200 mbar t = 15 min	NMP 1 h @80°C Rinse IPA NMP, US 3 s	No
Martinis group UC Santa Barbara [93]	Dolan bridges (+bandages)	MAA (300 nm) 10 min @160°C PMMA (500 nm) 10 min @160°C	MIBK:IPA	No	V = 400 V I = 21 mA 3 min / angle	O_2 P = 5 mbar t = 80 min	NMP @80°C	No
Schuster lab Chicago University [94] [95]	Dolan bridges & Manatthan	MAA PMMA	H20:IPA 1:3 (90s) Rinse IPA	No	Yes	O_2/Ar 80%/20% P = 20 mbar t = 12 min	NMP 3 h @80°C	Ion producing fan (avoid electrostatic discharge)
Quantum Nanoelectronics Laboratory Berkeley National Laboratory [96]	Manatthan	60 s @200°C cooled 60 s MAA 90 s @150°C AR-P 6200.9 60 s @150°C	IPA:H2O - US on Rinse IPA (10s)	P = 500 mbar t = 5 s per orientation Power = 10 W	No	10 min cooldown O_2/Ar 95%/5% (dynamic) P = 20 mbar t = 20 min	Acetone 2 h @67°C New acetone US 2 min Rinse IPA	Junction stabilization O_2 ashing P = 500 mbar t = 3 min Power=80 W
QuantECA Néel Institute Grenoble [97] [98]	Bridge-Free Fabrication technique	2 min @200°C PMMA-MAA 9% 600 s @200°C PMMA 4% 300 s @150°C	MIBK:IPA 1:3 (60s) Rinse IPA (30s)	P = 0.07 mbar t = 15 s Power = 10 W	No	O_2 P = 5.3 mbar t = 300 s	NMP 4 h @80°C US 1 min	No
SPEC CEA Saclay [99]	Dolan bridges (+bandages)	1 min @110°C MAA (EL10) 5 min @172°C PMMA A3 15 min @175°C	MIBK (60s) Rinse IPA (30s)	P = 0.2 mbar t = 10 s Power = 75 W	I = 5 mA 3 min / angle	O_2 P = 5 mbar t = 5 min	Acetone 10 min @80°C	Junction stabilization Heating 1 min @100°C
Quantic group LPENS [100]	Dolan bridges	MAA (EL 13) 3 min @ 180°C PMMA (A6) 3 min @ 180°C	H_2O:IPA 1:3 Rinse IPA	No	V = 500 V I = 30 mA 2 min / angle	O_2 P = 20 mbar t = 10 min	Acetone 5 min @50°C Rinse IPA	No

Table 5.1: Comparison of Josephson junctions fabrication recipes of various superconducting qubits groups. The evaporation steps before and after oxidation step, are marked by double lines. If the parameters in some boxes are not detailed, it means that we were unable to find them in the literature.

2.2.3 Experimental comparison of three different recipes

We remind that the motivation of this investigation is that our junctions get contaminated during the fabrication process. Hence our goal is to modify the pre-existing recipe in order to get rid of this contamination. Based on the recipes reviewed above, we test three different cleaning processes prior to the evaporation step. We image the junctions during fabrication after each step in order to compare the cleaning efficiency.

Presentation of the three test samples We test three different cleaning processes after development and before evaporation on three samples, all else being equal.

- **Sample 1: "Hard" argon milling** This sample is the control sample. It is fabricated with the usual ENS group recipe (last line of Table 5.1). In comparison to the other recipes, argon milling is performed with a highly energetic beam (thus called "hard" argon milling)
  - No O_2 stripping
  - Milling parameters : V = 500 V ; I = 30 mA ; 2 min / angle.
- **Sample 2: "Soft" argon milling** This sample undergoes a milling with a less energetic beam than sample 1 (thus sample 2 is called "soft" argon milling). Those voltage and intensity parameters were chosen after consulting an expert at Plassys company (the manufacturer of the evaporator used during fabrication).
  - No O_2 stripping
  - Milling parameters : V = 250 V ; I = 8 mA ; 2 min / angle.
- **Sample 3: O_2 stripping and no argon milling**

  This sample is only cleaned with O_2 plasma cleaning before evaporation. The pressure and power parameters are the same as those used in the ENS clean room machine's standard cleaning program. With those parameters, the resist layer is stripped off at a rate of $\sim$ 1-2 nm/s. Knowing that the resist thickness is $\sim$ 400nm (see Figure 5.3 top), we can deduce that $t = 40$ s is an appropriate upper limit to avoid breaking the resist suspended structures.
  - O_2 stripping : P = 0.13 mBar ; Power = 30 W ; t = 40 s.
  - No argon milling

Experimental protocol The samples are diced and taken from the same wafer. The fabrication protocol for tracking and imaging the differences between the samples is (the imaging steps are highlighted in bold):

- Clean the sample
- Spin resist

- E-beam lithography
- Development
- **Atomic Force Microscope imaging**
- O_2 stripping / argon milling (depending on the sample)
- **AFM imaging**
- Evaporation
- Lift-off
- **AFM imaging**

Results Figure 5.3 displays the result of this comparison for a single junction. Because there is not a clear optimal solution among the three options, it is difficult to draw positive conclusions from this investigation. All samples seem to have been contaminated during the evaporation and lift-off steps.
The surface of the resist appears irregular after hard argon milling, with a lot of cavities due to the milling (Figure 5.3 in sample 1 middle image). We can imagine that those impacts may project resist residues into the trenches so a softer argon milling, as performed on sample 2, is preferable.
Furthermore, in this investigation, the argon milling and the evaporation steps are carried out in a separate cleanroom from the ENS one (where the rest of the process and AFM imaging are performed). These back and forth trips in the outside environment are a limitation. On the contrary, in the real recipe, the argon milling is performed inside the evaporator, which thus may account for some inaccuracies in this comparative study.

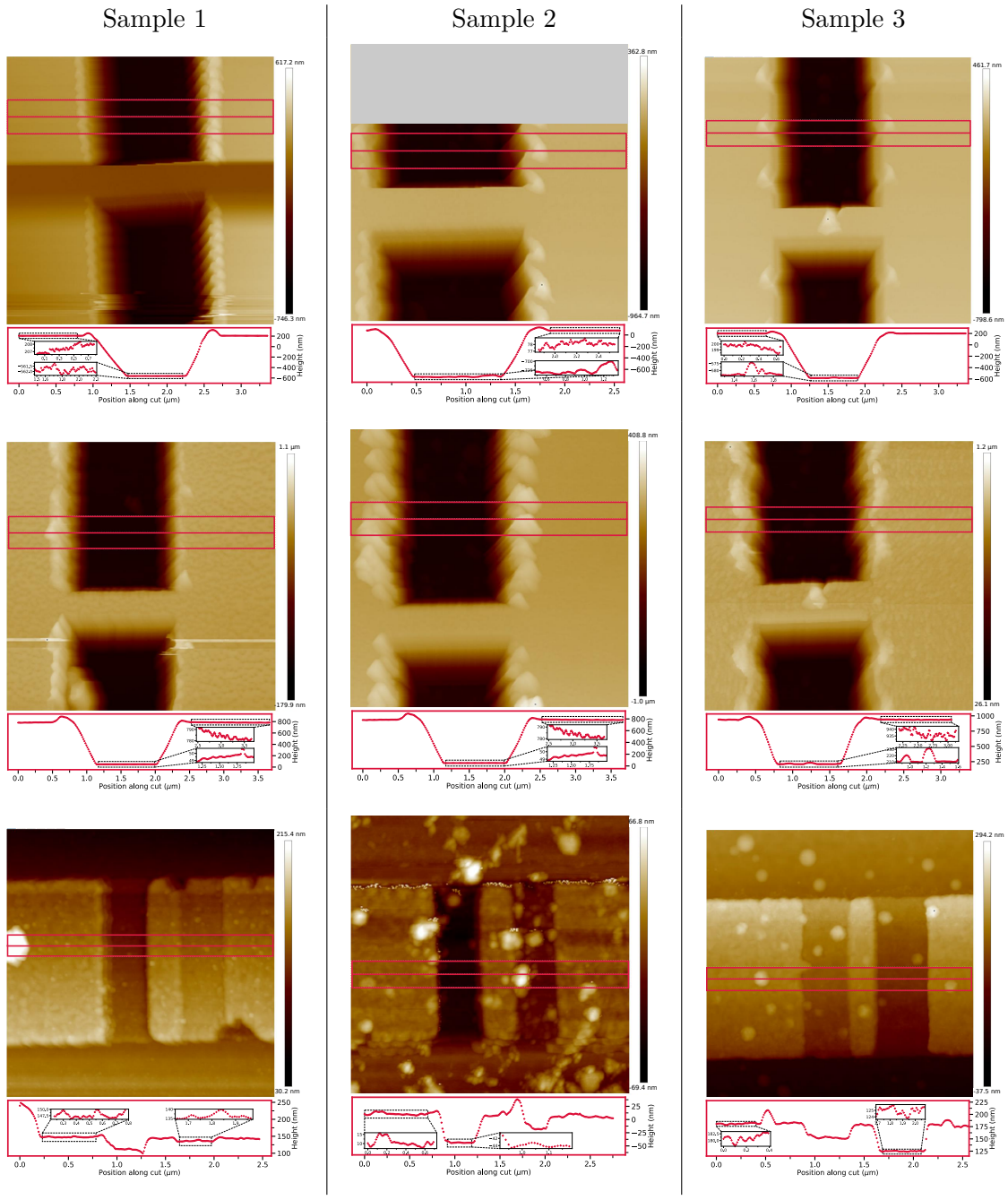

Figure 5.3: Comparison of AFM analysis of the 3 samples at different stages of fabrication of a single junction with a bridge width of 1.4 µm. Top: After development. Middle: After cleaning process (argon milling / O_2 stripping depending on samples). Bottom: After lift-off.
The 2D plots correspond to the tip sensor's measured relative height in forward motion. They are visualized using the software Nanoscope Analyis. The color scale indicates the relative heights. The height extrema are noted on both sides of the color scale box. Grey pixels indicate that no data was collected. The red line indicates a data cut along one direction. The red box around the line signals the area where the cut is averaged. The cut section is represented below each AFM image ; it plots the height as a function of the position along the cut. Insets in the plots are zoom windows that help to see the surface roughness more clearly.
The images of the bottom column are rotated with respect to the top columns. Indeed, since there are resist structures on the first two imaging steps, we wanted to scan along the direction of the resist bridge to avoid damaging it with the AFM's tip. When the junction is completed, in the bottom pictures, we wanted to scan perpendicular to the junction in order to have a cutting profile of the different sections on both sides of the junction.

2.2.4 Supplementary observation in favour of O_2 stripping

The following is another experimental observation that demonstrates O_2 stripping efficiency. A test sample on which we already had patterned niobium structure with laser writing (see process of Section 1) still presented resists marks after lift-off. These marks were visible with the optical microscope and long acetone baths at 50°C were useless to remove those residues. A 1 min O_2 stripping cleaning was efficient to remove those marks as displayed by Figure 5.4.

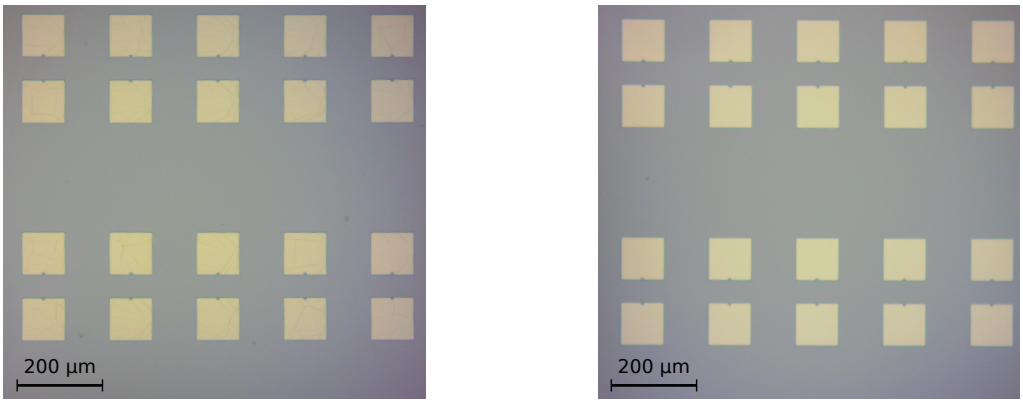

(a) Before stripping (b) After 1 min of O_2 stripping

Figure 5.4: False colors optical micrograph of a sample before (left) and after (right) cleaning step with 1 min of O_2 stripping. Blue is silicon, yellow is the niobium. The right picture shows cracking lines symptomatic of residual resist. The two pictures do not display the exact same locations on the sample but their comparison is still relevant since the resist residues were observed on the entire sample surface before cleaning.

2.2.5 Relevant points in the Josephson junction fabrication process

The investigation results are not conclusive but they allows us to take a step back from the pre-existing recipe of ENS that we modified to create our recipe, which is presented in Section 1. In particular, the literature review and investigation draw our attention to the cleaning steps: we added O_2 stripping cleaning steps in a more systematic manner, as indicated in the recipe description in the previous section. The following paragraphs are a summary of the other aspects of our recipe (see Section 1) that were changed as a result of the literature review and the experimental investigation.

Spinning resist We took the opportunity of testing the fabrication process to switch from PMMA A6 (anisole 6 %) resist to slightly lighter PMMA A3 (anisole 3 %) resist. In light of the literature review (see Table 5.1) we increase the baking time of this last resist layer to 30 min.

Cleaning procedure before evaporation Even though the investigation did not clearly show the efficiency of O_2 stripping prior to evaporation, it proved that it was not detrimental to the bridge structure. As a result, we include this cleaning step in order to be sure to ensure

that resist residues are removed after development.
We also have changed the argon milling parameters to perform a softer ion milling on the sample.

Lift-off As found in the literature review, we decided to increase the lift-off duration time and we also added a final step of low power sonication to ensure that small aluminium residues were removed. For interested readers, the detailed recipe with clean room machines parameters can be found in Appendix B.

Chapter 6

Conclusion and perspectives

Résumé en français

Ce chapitre de conclusion revient sur les résultats principaux du manuscrit et les met en perspective dans le cadre des avancées vers la conception d'un ordinateur quantique universel.
Le principal résultat de cette thèse est d'avoir mesuré un temps de bit-flip de l'ordre de 100 secondes pour des états à environ 40 photons dans un oscillateur pourvu de la dissipation à deux photons. Afin d'atteindre ces ordre des grandeurs, le circuit précédent de [59] a été réduit au minimum. Ces choix de design ont alors réduit à néant la possibilité de préparer et de mesurer des superpositions quantiques d'états dans notre système. Toutefois, notre expérience prouve qu'il n'y a rien au cœur du mécanisme de la dissipation à deux photons qui est au contraire à des longs temps de bit-flip. De plus, cette expérience démontre un temps de bit-flip macroscopique pour des états contenant un nombre mésoscopique de photons. Par la suite, d'autres expériences pourront progressivement retourner vers un régime plus approprié pour l'implémentation d'un bit quantique.
De façon plus générale, avec ce système, les flips de bit peuvent être corrigés de façon continue et autonome : il reste alors à utiliser les ressources de la correction d'erreur quantique pour éradiquer les flips de phase, seul canal d'erreur restant. Les performances démontrées dans ce travail de thèse permettent finalement d'envisager une réalisation concrète de la feuille de route menant à un ordinateur quantique universel.

This thesis work is in line with the emerging strategy which consists of encoding quantum information in the two meta-stable pointer states of an oscillator exchanging pairs of photons with its environment, a mechanism that has been demonstrated to provide stability without inducing decoherence. This strategy has resulted to a recent qubit, called the cat-qubit [51] which is embedded in the cavity field of a superconducting resonator that exchanges pairs of photons with its environment [58]. Adding photons in the cat qubit states has two opposing effects [59]. On the one hand, their distinguishability increases by an inevitably coupled uncontrolled environment, resulting in a linear increase of the phase-flip error rate. On the other hand, higher photon number implies a wider state separation resulting in a exponential increase of the bit-flip time. Therefore, in theory, it is possible to achieve macroscopic bit-flip times with computational states containing only a handful of photonic excitations, making them suitable for quantum information processing. However, in the previous experimental realisation, bit-flip time was saturating in the millisecond range [59].

The main result of this thesis is that we have measured timescales of the order 100 seconds for bit-flips between pointer states of a two-photon dissipative oscillator containing about 40 photons. In order to reach these numbers, we stripped of the previous circuit of [59] from everything we could afford. First, we devised a circuit with the objective of removing all suspected sources of dynamical instabilities. We fabricate the ATS, a two-photon exchange dipole element, close to the regime where its energy landscape exhibits a single global minimum at any operating point, which could be a requirement for stability [63, 67]. Second, we employ a minimally invasive fluorescence detection tool. Instead of using a transmon and readout mode, we directly measure the field radiated by the cavity, allowing us to access individual oscillator state trajectories. These design choices came at the expense of a two-photon exchange rate dominated by single-photon loss, resulting in the depletion of ability to prepare quantum superposition states and thus measure the phase-flip rate. Our experiment proves that nothing at the core of the two-photon dissipation mechanism is detrimental for high bit-flips times and puts a scale on the bit-flip times that can be achieved. Future experiments can then gradually enter the regime suitable for implementing a qubit where two-photon loss is the dominant dissipation mechanism. Moreover, other exploratory work could include monitoring oscillator trajectories over timescales of days or weeks to uncover the phenomena causing these bit-flip events [79, 80, 101].

The cat-qubit is situated at an intermediate scale, between qubits involving single excitations which are too prone to errors, and classical bits involving macroscopic numbers of particles which are incompatible with quantum information processing. This mesoscopic scale, involving a handful of photonic excitations per computational state, is well suited to eradicate bit-flip errors continuously and autonomously at the single qubit level, reserving the expensive arsenal of measurement based quantum error correction for the only significant remaining error: phase-flips. Indeed, phase flips can be corrected by encoding a logical qubit over a 1D chain of physical cat-qubits [64, 66]. Recent theoretical proposition for a controlled-not gate with cat qubits with

achievable experimental parameters is also promising to implement efficient repetition code with cat qubits [102]. This constitutes the road map for a cat-qubit based universal quantum computer.

Appendix A

Electromagnetic simulations

1 Introduction

This appendix is a supplement of Chapter 4. It describes an electromagnetic simulations strategy using the High Frequency Structure Simulator (HFSS) of ANSYS Electromagnetics Suite. This method is described step by step on the example of filtering stubs of Chapter 4 (Section 1 of this chapter). We start from a lumped model simulation (see Figure 4.6) and we gradually sophisticate the model to a realistic on-chip implementation (see Figure 4.9). We compare the simulation results of each step in order to demonstrate our strategy consistency. All the steps are detailed here with a view of being a guideline for interested readers wishing to reproduce this method.

Simplification of the simulation Simulating the whole 3D structure of a portion of coplanar transmission line is demanding in terms of memory and computational resources. Then, an appropriate strategy is to focus on the relevant parts of the chip and use a simulation halfway between the lumped model and the 3D distributed model. In the filter example, the behavior of the electromagnetic field along a coplanar transmission line is consistent with what we can expect from a lumped model. On the contrary, connections between portions of transmission line with impedance discontinuities, or extremities of the transmission lines are spots where the geometry do matter. As a result, in order to optimize the 3D electromagnetic simulation, we think the circuit we want to simulate as a block-based circuit. We simulate each block with a 3D model, register its scattering matrix, then we connect all those elements in a "Circuit design" project. This strategy is illustrated in Figure A.1.

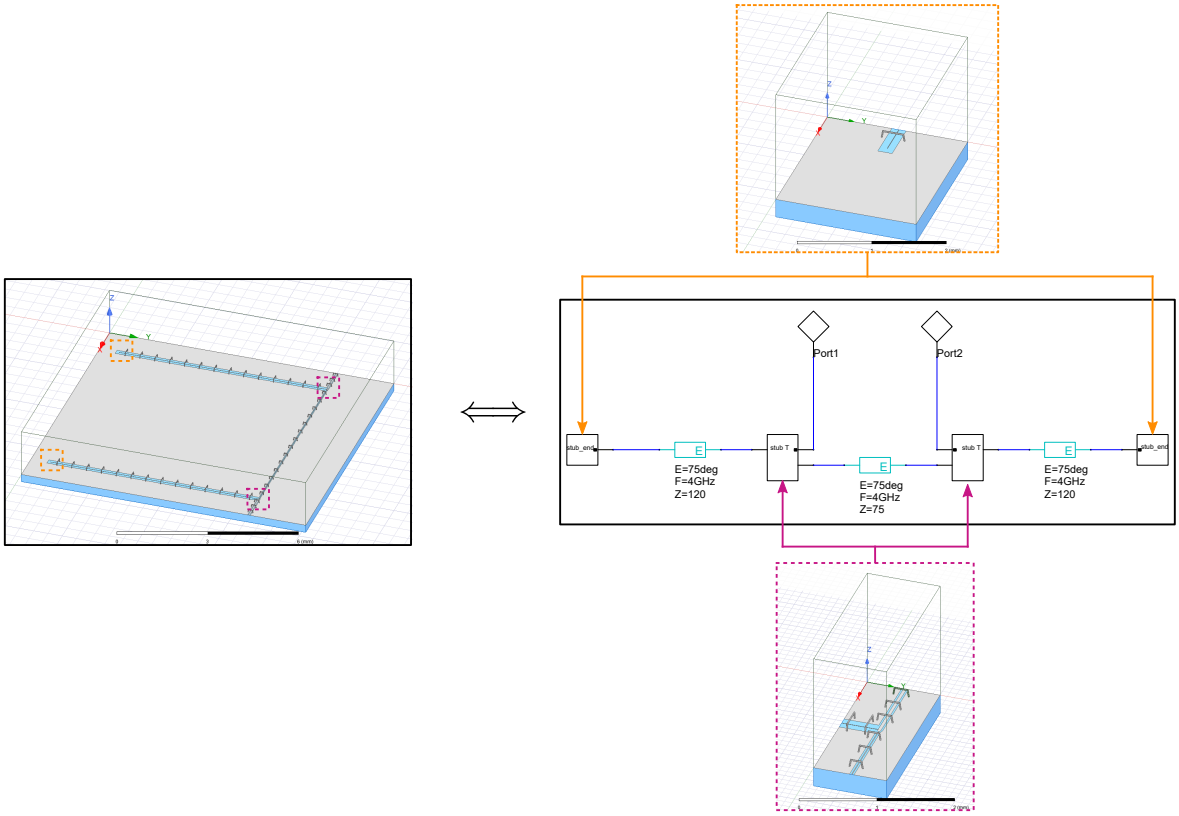

Figure A.1: Strategy for faster electromagnetic simulations. Left: view of HFSS 3D finite element design of the chip. The places of discontinuities for microwaves on the chip are surrounded in color with dashed lines. Those elements are simulated with a specific HFSS design surrounded by the matching color (right, top and bottom pictures). Once their S-matrix simulated, we can integrate those elements as black-box elements in a lumped circuit presented on the right (middle). In the HFSS design views, the silicon chip is in blue, the perfect conductor surface modeling superconducting metal is in grey. Bonds are in dark grey. The model is closed on the top with a box filled with air, whose borders are depicted with black lines. In the lumped circuit design we can create a network between the microwave components that represent simulated S-matrix (black rectangles), portions of transmission lines (blue rectangles with parameters specified below) and ports (black diamonds). The parameters of the transmission line are: the length of the line expressed in phase delay (noted "E"), the frequency (noted "F") and the characteristic impedance (noted "Z"). The blue wires represent the connection between the different elements but they do not match to any physical implementation nor layout.

Block diagram simulation Simulating a block diagram circuit with lumped elements is the most elementary step. We use the project "Circuit Design" in ANSYS Electromagnetics Suite. It is suitable for lumped models since we can connect dipoles and microwave elements (whether predefined from a data base or user defined from a scattering matrix data). In our case we use the lumped model of a transmission line which is in the ANSYS Electronic Desktop component library in the file "Groups", and named "TRL". We also work with the elements "Ports" to simulate the S-matrix between those distinct ports. We can connect the different ports of the network elements thanks to cables (those cables do not have any physical layout reality there are just a way to connect the components in a lumped model). Figure A.2 displays a screenshot of this circuit design. Note that the microwave analysis is extremely fast, which is the main interest of this "Circuit design" mode.
Figure A.6 shows the simulation results of this model. The filtering function of this network is clearly visible, as evidenced by a dip centered around central frequency 4 GHz. Plus, it confirms that the scattering parameter simulated through this lumped two-ports network perfectly matches with the analytical formula of scattering parameters.

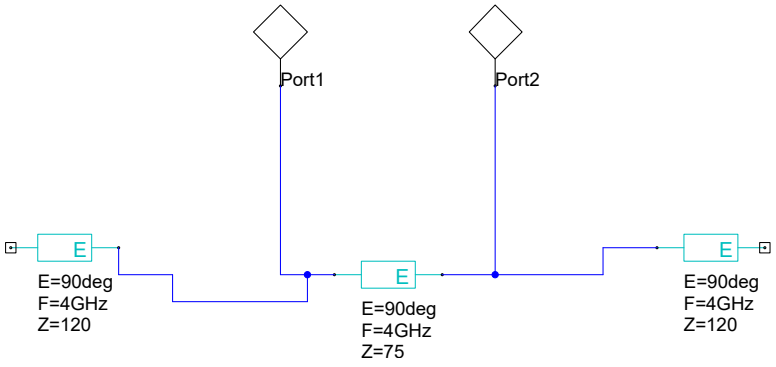

Figure A.2: Screenshot of the equivalent circuit diagram of the filters made in "Circuit Design" in ANSYS Electromagnetics Suite. Light blue rectangles are portions of transmission lines, black diamonds are ports. Blue wires represent the connection between the different elements.

Block diagram simulation with blocks defined from 3D components As we explained, there can be some mismatch between the lumped model and the real implementations due to angular shapes and design discontinuities encountered by the microwaves. Thus, the next step after the lumped circuit block diagram is to include blocks from simulated 3D elements.
We have simulated in "HFSS design" the connection between the three portions of transmission lines with different characteristic impedances as shown in Figure A.1 (purple color). We have used the solution type "Driven Modal" where we define wave ports at each extremities of transmission lines. Once we have simulated its S-matrix, this element can be viewed as a three-ports black-box element. Similarly, we simulate in "HFSS design" in "Driven Modal" the end of the stubs (orange color in Figure A.1). This element can now be summed up as a one-port element via its S-matrix.
In the "Circuit design", we can add a user-defined element by going in the component library, in

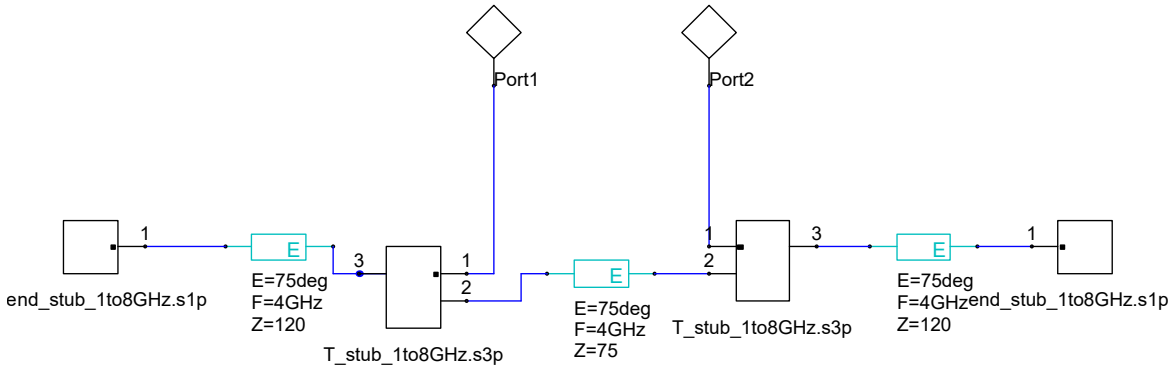

Figure A.3: Screenshot of the equivalent circuit diagram of the filters with 3D blocks included made in "Circuit Design" in ANSYS Electromagnetics Suite. Light blue rectangles are portions of transmission lines, black diamonds are ports, black rectangles are user-defined microwave components. Blue wires represent the connection between the different elements.

the file "Models", and select "N-port". Next, we have to indicate the path towards the registered data file including the simulation results of the 3D element (this is a .s*p file where * is the ports number). The ports name (1,2,3,..) are in agreement with the port definition set in the respective HFSS design 3D model.
In the 3D HFSS models standing for the connection and the end of the stubs, a small portion of cable is included in the model. Therefore, even if we should have $\lambda/4$ (that is to say 90°) long transmission lines, we should take into account the physical length already included in the partial 3D models. This gives a reduced effective length of the transmission line portion between the microwave elements. Figure A.3 shows a screenshot of the circuit diagram.
Simulating the 3D HFSS elements separately is quite fast since there are restricted in spatial dimensions. This strategy allows us to optimally test different configurations of shapes of connections between the portions of stubs.
Figure A.6 confirms that this semi-lumped simulation gives the same dynamics for S_{21} parameter than the full lumped model.

3D finite elements simulation Once we have tuned the shape of the connections between the stubs, we can validate the semi-lumped simulation thanks to a full 3D simulation. We have to take care to finely tune the lengths of the transmission lines sections since there are the ones that set the resonance frequency and thus the central frequency of the filter. Figure A.4 is a screenshot of simulated HFSS model. Figure A.6 demonstrates that the dynamics of S_{21} parameter stays the same when we go from lumped model to the 3D model.

3D simulation with geometrical constrains Adjusting the stubs to the layout constrains is the final step before on-chip implementation. Indeed, there are a lot of elements on the chip of the experiment (see Figure 2.1) so the stubs cannot be straight lines as in Figure A.4. As a result, we have to find a configuration in order to restrict the required space for the stubs on the chip. When changing the stubs geometry, we obviously have to take care to keep exactly

the same section lengths. Finally, using a 3D HFSS simulation ensures that the changes in geometry have not impacted the RF-behavior of the filters. Figure A.5 is a screenshot of the simulated HFSS model. S_{21} amplitude is shown in Figure A.6: it differs slightly from the other simulated models but it still exhibits the desired dynamics with an attenuation peak centered on the frequency of 4 GHz.

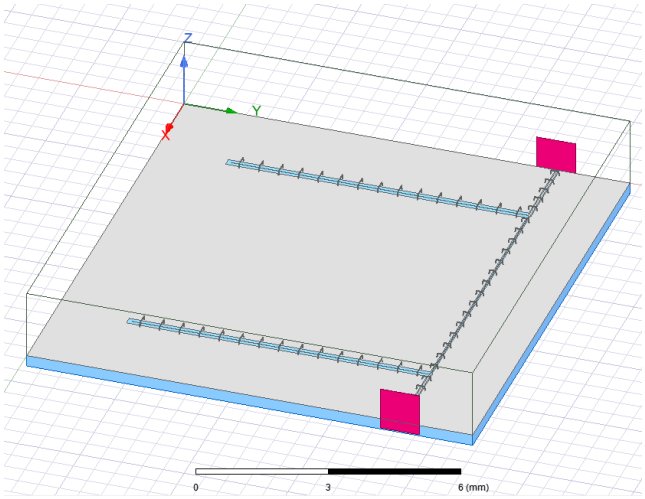

Figure A.4: Screenshot of HFSS 3D model of stubs filters. The silicon chip is in blue, the perfect conductor surface modeling superconducting metal is in grey. Bonds are in dark grey. The model is closed on the top with a box filled with air, whose borders are depicted with black lines. The wave ports are in red.

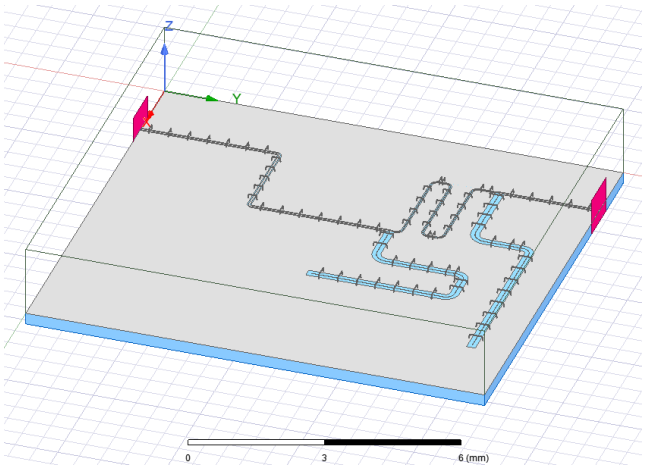

Figure A.5: Screenshot of HFSS 3D model of stubs filters revised to fit inside the real chip. The silicon chip is in blue, the perfect conductor surface modeling superconducting metal is in grey. Bonds are in dark grey. The model is closed on the top with a box filled with air, whose borders are depicted with black lines. The wave ports are in red.

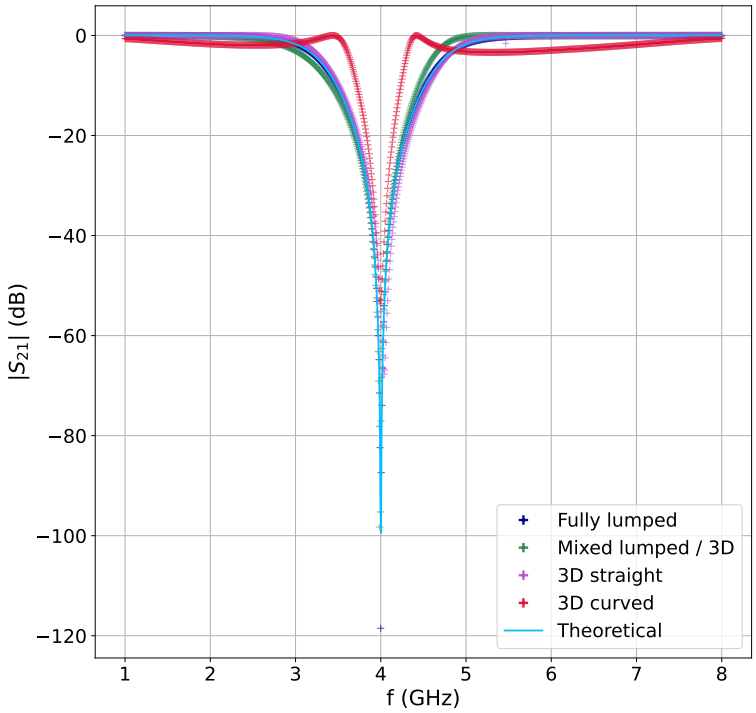

Figure A.6: Comparison of the amplitude of scattering parameter S_{21} as function of frequency of the filtering two-port network for different strategies of simulations. Light blue solid line, labelled as "Theoretical", is plotted from analytical calculations as a reference (see Section 1 of Chapter 4). Simulations results are plotted for the fully lumped circuit diagram simulation results (blue crosses, labelled as "Fully lumped") ; lumped circuit diagram with S-matrix of 3D elements (green crosses, labelled as "Mixed lumped / 3D") ; HFSS 3D model with no geometrical constrains (purple crosses, labelled as "3D straight") ; HFSS 3D model with geometrical constrains and curved stubs (red crosses, labelled as "3D curved").

Appendix B

Nanofabrication recipe

This appendix details the nanofabrication recipe of the chips presented in the main manuscript. It comes as a supplement of Chapter 5.

1 Nanofabrication recipe

1.1 Wafer preparation

We start with a 280 µm, 2-inch intrinsic silicon wafer. We load it into the sputterer and deposit 120 nm of Nb when the pressure in the load is suffiently low.
In order to be able to circumvent small variations inherent to nanofabrication process, we fabricate 12 10 x 11 mm chips on the same wafer. We cut the individual chips at the end of the process.

Cleanliness of the wafer At the start of the fabrication process, caution must be taken to ensure the cleanliness of the wafer. Examining with the optical microscope in dark field mode in order to see the imperfections on the wafer is a good practice.
We tried to clean the wafer before any other process (acetone bath with sonication on, rinsing in IPA and blow-drying with N_2 gun). It appears that this step leaves some traces such as dried drops on the edge of the wafer so we have decided not to include a pre-cleaning step in the recipe.

1.2 Circuit patterning

Spinning resist

- Deposit S1805 resist on the wafer. Use a pipet or use a filtered syringe if you have cleanliness issues with contaminants deposition at this step.
- Spin using the registered recipe "qelec jpc".
- Bake it on a hot plate for 1 min at 115°C with a beaker as a cover on top.

- Check at the microscope that there is not any comet or important dust density on the chip (this must be done in the resist room with a yellow light microscope in order to avoid exposing resist to light).

Laser lithography

- Load into the laser lithography machine.
- Look for the wafer edges, note down their coordinates and use them to go to the center of the wafer (this step is done using lens 3).
- Perform the 3-point plane focus (using the lens used for writing step) around the center.
- Do not forget to go back to the center of the wafer before launching the writing process.
- Since the minimal dimensions of our circuit are typically ~ 5 µm, on the ENS laser-writer using lens 4 and D-step of 2 is precise enough for writing.
- Launch the lithography with the dose 203 mJ/cm^2.

Development

- Develop in MF319 for 1 min in a big beaker. During the development, softly rotate the beaker in order to solve the exposed resist in a more homogeneous way.
- Rinse in DI water for 1 min shaking in the same way.
- Blow dry.
- Check at the optical microscope that everything seems to be correctly developed (this must be done in the resist room with a yellow light microscope in order to avoid exposing remaining resist to light).

Reactive Ion Etching

- Load into the RIE machine.
- Wait for sufficiently low pressure in order to avoid to have some impurities in the load-lock during the etching (wait for $P_{\text{load}} \sim 9$nBar).
- Etch with SF6.
- We monitor in real time the reflectivity of a laser light spot sent on a region of the chip dedicated to be etched. As long as there is still some niobium, the reflectivity remains constant. When all niobium has been etched, the light spot reflects now on the silicon layer which is less reflective than niobium. Thus, we observe a steep decline of reflectivity plot: this is the end criterion for the etching process.
- To be sure that all niobium has been taken off, we process to an over-etching of 10 s (we wait for 10 extra seconds as a safety margin after the reflectivity drop before stopping the process).

Lift-off and final cleaning

- Put the wafer in a beaker of hot acetone at 50°C and sonicate for 5min (US 7). Then we assume that acetone is saturated in resist and has taken the major part so we change the wafer.
- Put the wafer in a new beaker of hot acetone at 50°C and sonicate for 20-25min (US 7).
- Rinse in IPA and sonicate for 1min.
- Blow dry with N_2 gun.
- Load for 20 s of O_2 stripping in order to remove all residual organic contaminants. For this stripping step we wait for the pressure in the load-lock to be low enough (wait to have $P_{load} \sim 9$ nBar) to avoid impurities. The parameters are: P = 0.13 mBar ; Power = 30 W ; Flow=100 sscm.

1.3 Josephson junctions fabrication

Cleaning It is really important to start spinning resist on a clean sample. In a complete fabrication process with a previous laser circuit patterning this cleaning step is actually done with the lift-off of laser writing resist.

- Acetone with US.
- Rinse in IPA.
- Blow dry with N_2 gun.
- O_2 stripping t = 10 s ; P = 0.13 mBar ; Power = 30 W ; Flow=100 sscm.

Spinning resist To fabricate Dolan-bridge junctions we need two layers of resist.

- Bake the sample 60 s @185°C. During all baking steps we are covering the sample with an upside down beaker to avoid impurities from falling onto the chip.
- Spin MAA EL 13 - 5 s @500 rpm - 60 s @5000 rpm.
- Bake 1 min @185°C.
- Spin PMAA A3[1] - 3 s @500 rpm - 60 s @4000 rpm.
- Bake 30 min @185°C.

SEM lithography The pattern of the Dolan bridge is written in the resist with SEM lithography. We write with a beam aperture of 7.5 µm, a beam voltage of 20 kV. The reference dose is 283 µmAs/cm^2.

[1] Noting PMMA Ax, x represents the percentage in anisole which is a solvent for the resist.

Development The development is made in a solution of H_2O:IPA at temperature of 6.0°C. When developing, the operator should shake the chip in order to make the development more homogeneous. The development step is crucial since it controls the 3D dimensions of the bridges. Then, the operator should take care to be consistent and regular for each fabrication batch, even in the way they are shaking the chip.

- H_2O:IPA 1:3 90 s @6.0°C.
- Rinse in IPA for 10 s.
- Blow dry.

O_2 stripping We add this cleaning step in order to be sure to remove resist residues after development. The parameters are : P=0.13 mBar ; Power = 30 W ; t = 40 s ; Flow = 100 sscm.

Evaporation step This step occurs in a Plassys evaporator and includes multiple sub-steps. First, argon milling is done for each evaporation angle to clean and to ensure a good connection between the niobium and the aluminium layer to be deposited. Then, we perform a titanium cleaning of the load-lock to catch impurities before the evaporation. Next, we proceed to the two angles evaporation, separated by an oxidation time dedicated to the growth of oxide barrier. A final oxidation is realized in order to passivate and protect the junction.

- Argon milling with O_2: Flow Ar : 4 sscm ; Flow O_2 = 1 sscm. U = 250 V ; I = 8 mA. 2 min / angle.
- Titanium cleaning of the chamber.
- Evaporate aluminium at angle +30°. Rate 1 nm/s, total width = 35 nm.
- Oxidation O_2 ; P = 20 mbar ; t = 10 min.
- Evaporate aluminium at angle -30°. Rate 1 nm/s, total width = 70 nm.
- Final oxidation O_2 ; P = 300 mBar ; t = 3min (static).

Lift-off As found in the literature review, we have increased the lift-off duration time and we have added a final step of low power sonication in order to be sure to take off small aluminium residues.

- Acetone @50°C for 1 h.
- Use a pipette to flow some acetone on the chip to help the removal of resist/aluminium foil.
- New acetone @50°C for 5 min.
- US for 10 s low power.
- Rinse IPA.
- Blow dry with N_2 gun.

O_2 stripping This step is the final cleaning step, performed with the following parameters: P=0.13 mBar ; Power=30 W ; t = 10 s ; Flow=100 sscm.

Testing the junctions For each sample, we fabricate control junctions on the chip in order to measure their Josephson energy. We measure the room temperature resistance of the Josephson junction at the probe station and deduce the Josephson coupling energy thanks to the Ambegaokar-Baratof formula [43].

1.4 Selecting the chip and mounting the sample

The chips are fabricated on a wafer in order to optimize the fabrication process and to be more robust to small variations of nanofabrication. At the end of the wafer fabrication we select the most favorable chip for the experiment.
This means that we first check at the optical microscope the visual aspect of all coplanar waveguide lines. Second, we have to select the sample focusing on the Josephson junctions. This is done by measuring via a probe station the Josephson energy of the test junctions fabricated on the same sample (see the item above)

Dicing In order to protect the samples against dust produced by the dicing step we first spin and bake a PMMA resist layer on the wafer. The exact nature of the resist is not important as long as it can be removed easily after dicing.

- Spin PMMA resist on the sample.
- Bake 1 min @185°C.

Then, we cut the samples on the wafer with the automated dicing machine (the wafer is face up towards the saw).

Cleaning This step is the last cleaning step before cooling down of the sample and measuring it.

- Flow DI water on the sample (we believe it can remove the small dusts due to dicing).
- Acetone bath at 50°C, no sonication for 20 min.
- New acetone bath at 50°C no sonication for 20 min.
- Rinse in IPA for 1 min.
- Blow dry.
- Perform a 10 s O_2 stripping to remove all organic residues.
- Measure the test junctions on the sample again to check the Josephson energy drift between the first measurement and just before cooling down.

Mounting on the sample holder The chips of this thesis work were measured in the sample holder developed in the laboratory [85] called JAWS. A good practice when renewing the chip in the sample holder is to clean the sample holder itself.

- Open the sample holder in the three parts (top cover, bottom cover, and middle part hosting the PCB).
- Pour all the three parts in an acetone bath at room temperature.
- Wipe the PCB with a clean room cotton bud in order to be sure to take off all residues of bonds.
- Rinse the three parts in IPA.
- Dry with cleanroom paper and use N_2 gun for small asperities.
- Reassemble the sample holder.

Then we can mount the sample in the JAWS holder.

- Place a small amount of PMMA on the four corners of the sample location in the sample holder. The amount of PMMA in each corner should be enough to glue the chip. However, it should not be excessive to prevent the resist from overflowing and spreading on the sample.
- Drop the sample on its location.
- Gently press with tweezers on the sample corners for gluing it thanks to resist.

Finally, we have to proceed to microbonding to connect all parts of the ground plane on the chip and to connect the device DC and RF electrodes to their respective sample holder lines.

2 Useful tips

2.1 How to convert a .gds into a .svg file to create beautiful pictures?

I wanted to share this tip but I did not find a better location in this manuscript, so here it is! When creating beautiful circuit illustrations for reports, articles or PhD dissertations, it can be very useful to convert a .gds file (which is the drawing of the chip for laser writer) to a .svg file (which is a format compatible with a lot of image softwares). The following trick works with the K-layout software. This tips was obtained from the K-Layout forum:
https://www.klayout.de/forum/discussion/873/working-with-dxfs.
The idea is to use a specific macro code (here in Ruby).

- Open your .gds file with K-Layout software.
- Click on "Macros" → "Macro Development (F5)". The macro window opens.

- Select the "Ruby" tab.
- Create a new macro by clicking on the cross "new" (you can create and save the macro in any file you want).
- Select "general" type for macro.
- Copy and paste the following macro code below in the file window (on the right).
- Click on green triangle icon "Run current script".
- A window opens for you to select the location for the .svg file to be created.
- Tadaam ! There is no particular message at the end of the process so you can just go and check on the desired location that your .svg file has been generated.
- You can save this macro to use it again by clicking on the saving icon.

The macro code in Ruby

```
class SVGWriter

  def initialize(file)
    @file = File.open(file, "w")
  end

  def start(w, h)
    @file.puts(<<"END")
<?xml version="1.0" encoding="UTF-8" standalone="no"?>
<!-- Created with Inkscape (http://www.inkscape.org/) -->

<svg
   xmlns:svg="http://www.w3.org/2000/svg"
   xmlns="http://www.w3.org/2000/svg"
   xmlns:xlink="http://www.w3.org/1999/xlink"
   width="#{'%.12g'%w}"
   height="#{'%.12g'%h}"
   version="1.1">
END
  end

  def finish
    @file.puts("</svg>")
    @file.close
  end

  def begin_layer(lp)
    @stroke_color = lp.frame_color
    @fill_color = lp.fill_color
  end

  def polygon(p, dbu)

    pts = []
    p.each_point_hull { |pt| pts << ("%.12g %.12g" % [pt.x * dbu, pt.y * dbu]) }
    ctrs = [ "M " + pts.join(" L ") + " z" ]
    p.holes.times do |h|
```

```
      pts = []
      p.each_point_hole(h) { |pt| pts << ("%.12g %.12g" % [pt.x * dbu, pt.y * dbu]) }
      ctrs << [ "M " + pts.join(" L ") + " z" ]
    end
    d = ctrs.join(" ")

    @file.puts("  <path style=\"fill:##{'%06x' % (@fill_color & 0xffffff)}\"")
    @file.puts("        d=\"#{d}\"/>")

  end

end

lv = RBA::LayoutView::current
lv || raise("No view opened")

cv = RBA::CellView::active
cv || raise("No layout loaded")
ly = cv.layout
cell = cv.cell

out = RBA::FileDialog::ask_save_file_name("Chose SVG file to write", ".", "SVG files (*.svg);;All files (*)")
if out

  layers = []

  li = lv.begin_layers
  while !li.at_end?
    if li.current.visible? && !li.current.has_children? && li.current.layer_index >= 0
      layers << li.current
    end
    li.next
  end

  bbox = cell.bbox
  dbu = ly.dbu

  writer = SVGWriter::new(out)
  writer.start(bbox.width * dbu, bbox.height * dbu)

  canvas_tr = RBA::CplxTrans::new(1.0, 0.0, true, RBA::DPoint::new(-bbox.left, bbox.top))

  layers.each do |lp|
    writer.begin_layer(lp)
    si = cell.begin_shapes_rec(lp.layer_index)
    while !si.at_end?
      s = si.shape
      if s.is_path? || s.is_box? || s.is_polygon?
        writer.polygon(s.polygon.transformed(canvas_tr * si.trans), dbu)
      end
      si.next
    end
  end

  writer.finish

end
```

Bibliography

[1] Maxwell, J. C. (1868). I. on governors. *Proceedings of the Royal Society of London*, (16), 270–283 (cit. on p. 3).

[2] Petit, N., & Rouchon, P. (2016, February). *Principes fondamentaux de l'automatique. dynamique et contrôle des systèmes*. CAS - Mines ParisTech. (Cit. on p. 3).

[3] Guckenheimer, J., & Holmes, P. (1983). Closed orbits, poincare maps, and forced oscillations. In *Nonlinear oscillations, dynamical systems, and bifurcations of vector fields* (pp. 22–32). Springer New York. (Cit. on p. 6).

[4] Heugel, T. L. (2022). Parametric driving. In *Parametrons: From sensing to optimization machines* (pp. 12–16). ETH Zurich. (Cit. on pp. 6–8).

[5] Lescanne, R. (2020a). Bistable systems in classical mechanics. In *Engineering multi-photon dissiption in superconducting circuits for quantum error correction* (pp. 11–14). École Normale Supérieure. (Cit. on p. 8).

[6] Mumford, W. (1960). Some notes on the history of parametric transducers. *Proceedings of the IRE*, *48*(5), 848–853 (cit. on p. 10).

[7] Slichter, D. H. (2011). *Quantum jumps and measurement backaction in a superconducting qubit*. University of California, Berkeley. (Cit. on p. 10).

[8] Faraday, M. (1837). On a peculiar class of acoustical figures; and on certain forms assumed by groups of particles upon vibrating elastic surfaces. *Abstracts of the Papers Printed in the Philosophical Transactions of the Royal Society of London*, (3), 49–51 (cit. on p. 10).

[9] Feldman, M., Parrish, P., & Chiao, R. (1975). Parametric amplification by unbiased josephson junctions. *Journal of Applied Physics*, *46*(9), 4031–4042 (cit. on p. 10).

[10] Vijay, R., Slichter, D. H., & Siddiqi, I. (2011). Observation of quantum jumps in a superconducting artificial atom. *Physical review letters*, *106*(11), 110502 (cit. on p. 10).

[11] Castellanos-Beltran, M., Irwin, K. D., Hilton, G., Vale, L. R., & Lehnert, K. W. (2008). Amplification and squeezing of quantum noise with a tunable josephson metamaterial. *Nature Physics*, *4*(12), 929–931 (cit. on p. 10).

[12] Abdo, B., Schackert, F., Hatridge, M., Rigetti, C., & Devoret, M. (2011). Josephson amplifier for qubit readout. *Applied Physics Letters*, *99*(16), 162506 (cit. on p. 10).

[13] Pfaff, W., Axline, C. J., Burkhart, L. D., Vool, U., Reinhold, P., Frunzio, L., Jiang, L., Devoret, M. H., & Schoelkopf, R. J. (2017). Controlled release of multiphoton quantum states from a microwave cavity memory. *Nature Physics*, *13*(9), 882–887 (cit. on pp. 10, 13).

[14] Eddins, A., Kreikebaum, J., Toyli, D., Levenson-Falk, E., Dove, A., Livingston, W., Levitan, B., Govia, L., Clerk, A., & Siddiqi, I. (2019). High-efficiency measurement of an artificial atom embedded in a parametric amplifier. *Physical Review X*, *9*(1), 011004 (cit. on pp. 10, 13).

[15] Aumentado, J. (2020). Superconducting parametric amplifiers: The state of the art in josephson parametric amplifiers. *IEEE Microwave magazine*, *21*(8), 45–59 (cit. on pp. 10, 12).

[16] Dykman, M. (Ed.). (2012, July). *Fluctuating nonlinear oscillators*. Oxford University Press. (Cit. on pp. 10, 13).

[17] Boyd, R. W. (2020). *Nonlinear optics*. Academic press. (Cit. on p. 11).

[18] Melkonian, J.-M., Dherbecourt, J.-B., Raybaut, M., & Godard, A. (2021). Optical parametric oscillators. *Photoniques*, (110), 53–57 (cit. on p. 11).

[19] Giordmaine, J. A., & Miller, R. C. (1965). Tunable coherent parametric oscillation in linb o 3 at optical frequencies. *Physical Review Letters*, *14*(24), 973 (cit. on p. 12).

[20] Roy, A., & Devoret, M. (2016). Introduction to parametric amplification of quantum signals with josephson circuits. *Comptes Rendus Physique*, *17*(7), 740–755 (cit. on p. 12).

[21] Yamamoto, T., Koshino, K., & Nakamura, Y. (2016). Parametric amplifier and oscillator based on josephson junction circuitry. In *Principles and methods of quantum information technologies* (pp. 495–513). Springer. (Cit. on p. 12).

[22] Krantz, P., Kjaergaard, M., Yan, F., Orlando, T. P., Gustavsson, S., & Oliver, W. D. (2019). A quantum engineer's guide to superconducting qubits. *Applied physics reviews*, *6*(2), 021318 (cit. on p. 12).

[23] Metelmann, A., & Clerk, A. A. (2015). Nonreciprocal photon transmission and amplification via reservoir engineering. *Physical Review X*, *5*(2), 021025 (cit. on p. 12).

[24] Ranzani, L., & Aumentado, J. (2015). Graph-based analysis of nonreciprocity in coupled-mode systems. *New Journal of Physics*, *17*(2), 023024 (cit. on p. 12).

[25] Yamamoto, T., Inomata, K., Watanabe, M., Matsuba, K., Miyazaki, T., Oliver, W. D., Nakamura, Y., & Tsai, J. (2008). Flux-driven josephson parametric amplifier. *Applied Physics Letters*, *93*(4), 042510 (cit. on p. 12).

[26] Yaakobi, O., Friedland, L., Macklin, C., & Siddiqi, I. (2013). Parametric amplification in josephson junction embedded transmission lines. *Physical Review B*, *87*(14), 144301 (cit. on p. 12).

[27] Zhou, X., Schmitt, V., Bertet, P., Vion, D., Wustmann, W., Shumeiko, V., & Esteve, D. (2014). High-gain weakly nonlinear flux-modulated josephson parametric amplifier using a squid array. *Physical Review B*, *89*(21), 214517 (cit. on p. 12).

[28] Sivak, V., Shankar, S., Liu, G., Aumentado, J., & Devoret, M. (2020). Josephson array-mode parametric amplifier. *Physical Review Applied*, *13*(2), 024014 (cit. on p. 12).

[29] Dykman, M., Maloney, C., Smelyanskiy, V., & Silverstein, M. (1998). Fluctuational phase-flip transitions in parametrically driven oscillators. *Physical Review E*, *57*(5), 5202 (cit. on p. 13).

[30] Krantz, P. (2013). *Parametrically pumped superconducting circuits* [Ph.D. Thesis]. Chalmers Tekniska Hogskola (Sweden). (Cit. on p. 13).

[31] Wilson, C. M., Johansson, G., Pourkabirian, A., Simoen, M., Johansson, J. R., Duty, T., Nori, F., & Delsing, P. (2011). Observation of the dynamical casimir effect in a superconducting circuit. *nature*, *479*(7373), 376–379 (cit. on p. 13).

[32] Haus, H. A., & Mullen, J. (1962). Quantum noise in linear amplifiers. *Physical Review*, *128*(5), 2407 (cit. on p. 13).

[33] Yurke, B., Corruccini, L., Kaminsky, P., Rupp, L., Smith, A., Silver, A., Simon, R., & Whittaker, E. (1989). Observation of parametric amplification and deamplification in a josephson parametric amplifier. *Physical Review A*, *39*(5), 2519 (cit. on p. 13).

[34] Lin, Z., Inomata, K., Koshino, K., Oliver, W., Nakamura, Y., Tsai, J.-S., & Yamamoto, T. (2014). Josephson parametric phase-locked oscillator and its application to dispersive readout of superconducting qubits. *Nature communications*, *5*(1), 1–6 (cit. on p. 13).

[35] Siddiqi, I., Vijay, R., Pierre, F., Wilson, C. M., Metcalfe, M., Rigetti, C., Frunzio, L., & Devoret, M. H. (2004). Rf-driven josephson bifurcation amplifier for quantum measurement. *Phys. Rev. Lett.*, *93*, 207002 (cit. on p. 13).

[36] Krantz, P., Bengtsson, A., Simoen, M., Gustavsson, S., Shumeiko, V., Oliver, W. D., Wilson, C. M., Delsing, P., & Bylander, J. (2016). Single-shot read-out of a superconducting qubit using a josephson parametric oscillator. *Nature Communications*, *7*(1) (cit. on p. 13).

[37] Awschalom, D. D., Bassett, L. C., Dzurak, A. S., Hu, E. L., & Petta, J. R. (2013). Quantum spintronics: Engineering and manipulating atom-like spins in semiconductors. *Science*, *339*(6124), 1174–1179 (cit. on p. 14).

[38] Monroe, C., & Kim, J. (2013). Scaling the ion trap quantum processor. *Science*, *339*(6124), 1164–1169 (cit. on p. 14).

[39] Jaksch, D., & Zoller, P. (2005). The cold atom hubbard toolbox. *Annals of physics*, *315*(1), 52–79 (cit. on p. 14).

[40] Gross, C., & Bloch, I. (2017). Quantum simulations with ultracold atoms in optical lattices. *Science*, *357*(6355), 995–1001 (cit. on p. 14).

[41] Knill, E., Laflamme, R., & Milburn, G. J. (2001). A scheme for efficient quantum computation with linear optics. *nature*, *409*(6816), 46–52 (cit. on p. 14).

[42] Kok, P., Munro, W. J., Nemoto, K., Ralph, T. C., Dowling, J. P., & Milburn, G. J. (2007). Linear optical quantum computing with photonic qubits. *Reviews of modern physics*, *79*(1), 135 (cit. on p. 14).

[43] Girvin, S. M. (2014). Circuit QED: Superconducting qubits coupled to microwave photons. In M. Devoret, B. Huard, R. Schoelkopf, & L. F. Cugliandolo (Eds.), *Quantum Machines: Measurement and Control of Engineered Quantum Systems (Les Houches Session XCVI)* (pp. 113–256). Oxford University Press. (Cit. on pp. 14, 93, 94, 117).

[44] Goto, E. (1959). The parametron, a digital computing element which utilizes parametric oscillation. *Proceedings of the IRE*, *47*(8), 1304–1316 (cit. on p. 15).

[45] Rojas, R., & Hashagen, U. (2002). *The first computers: History and architectures*. MIT press. (Cit. on p. 15).

[46] Mabuchi, H. (2011). Nonlinear interferometry approach to photonic sequential logic. *Applied Physics Letters*, *99*(15), 153103 (cit. on p. 15).

[47] Kerckhoff, J., & Lehnert, K. W. (2012). Superconducting microwave multivibrator produced by coherent feedback. *Physical Review Letters*, *109*(15) (cit. on p. 15).

[48] Joshi, A., Noh, K., & Gao, Y. Y. (2021). Quantum information processing with bosonic qubits in circuit qed. *Quantum Science and Technology*, *6*(3), 033001 (cit. on p. 15).

[49] Michael, M. H., Silveri, M., Brierley, R., Albert, V. V., Salmilehto, J., Jiang, L., & Girvin, S. M. (2016). New class of quantum error-correcting codes for a bosonic mode. *Physical Review X*, *6*(3), 031006 (cit. on p. 15).

[50] Gottesman, D., Kitaev, A., & Preskill, J. (2001). Encoding a qubit in an oscillator. *Phys. Rev. A*, *64*(1), 012310 (cit. on p. 15).

[51] Mirrahimi, M., Leghtas, Z., Albert, V. V., Touzard, S., Schoelkopf, R. J., Jiang, L., & Devoret, M. H. (2014). Dynamically protected cat-qubits: A new paradigm for universal quantum computation. *New J. Phys.*, *16*(4), 045014 (cit. on pp. 15, 22, 50, 105).

[52] Gautier, R., Sarlette, A., & Mirrahimi, M. (2022). Combined dissipative and hamiltonian confinement of cat qubits. *P R X Quantum*, *3*, 020339 (cit. on p. 16).

[53] Puri, S., Boutin, S., & Blais, A. (2017). Engineering the quantum states of light in a Kerr-nonlinear resonator by two-photon driving. *npj Quantum Inf.*, *3*(1), 18 (cit. on pp. 16, 43).

[54] Grimm, A., Frattini, N. E., Puri, S., Mundhada, S. O., Touzard, S., Mirrahimi, M., Girvin, S. M., Shankar, S., & Devoret, M. H. (2020). Stabilization and operation of a kerr-cat qubit. *Nature*, *584*(7820), 205–209 (cit. on p. 16).

[55] Frattini, N. E. (2021). *Three-wave mixing in superconducting circuits: Stabilizing cats with snails* [Doctoral dissertation, Yale University]. (Cit. on p. 16).

[56] Krauter, H., Muschik, C. A., Jensen, K., Wasilewski, W., Petersen, J. M., Cirac, J. I., & Polzik, E. S. (2011). Entanglement generated by dissipation and steady state entanglement of two macroscopic objects. *Physical review letters*, *107*(8), 080503 (cit. on p. 16).

[57] Shankar, S., Hatridge, M., Leghtas, Z., Sliwa, K., Narla, A., Vool, U., Girvin, S. M., Frunzio, L., Mirrahimi, M., & Devoret, M. H. (2013). Autonomously stabilized entanglement between two superconducting quantum bits. *Nature*, *504*(7480), 419–422 (cit. on p. 16).

[58] Leghtas, Z., Touzard, S., Pop, I. M., Kou, A., Vlastakis, B., Petrenko, A., Sliwa, K. M., Narla, A., Shankar, S., Hatridge, M. J., Reagor, M., Frunzio, L., Schoelkopf, R. J., Mirrahimi, M., & Devoret, M. H. (2015). Confining the state of light to a quantum manifold by engineered two-photon loss. *Science*, *347*(6224), 853–857 (cit. on pp. 16, 17, 22, 23, 105).

[59] Lescanne, R., Villiers, M., Peronnin, T., Sarlette, A., Delbecq, M., Huard, B., Kontos, T., Mirrahimi, M., & Leghtas, Z. (2020). Exponential suppression of bit-flips in a qubit encoded in an oscillator. *Nature Physics*, *16*(5), 509–513 (cit. on pp. 16, 17, 23–25, 28, 41, 60, 61, 67, 73, 104, 105).

[60] Aiello, G., Féchant, M., Morvan, A., Basset, J., Aprili, M., Gabelli, J., & Estève, J. (2022). Quantum bath engineering of a high impedance microwave mode through quasiparticle tunneling. *Nature Communications*, *13*(1), 7146 (cit. on p. 16).

[61] Touzard, S., Grimm, A., Leghtas, Z., Mundhada, S. O., Reinhold, P., Axline, C., Reagor, M., Chou, K., Blumoff, J., Sliwa, K. M., Shankar, S., Frunzio, L., Schoelkopf, R. J., Mirrahimi, M., & Devoret, M. H. (2018). Coherent oscillations inside a quantum manifold stabilized by dissipation. *Phys. Rev. X*, *8*, 021005 (cit. on p. 17).

[62] Lescanne, R., Verney, L., Ficheux, Q., Devoret, M. H., Huard, B., Mirrahimi, M., & Leghtas, Z. (2019). Escape of a driven quantum josephson circuit into unconfined states. *Phys. Rev. Applied*, *11*, 014030 (cit. on p. 17).

[63] Verney, L., Lescanne, R., Devoret, M. H., Leghtas, Z., & Mirrahimi, M. (2019). Structural instability of driven josephson circuits prevented by an inductive shunt. *Phys. Rev. Applied*, *11*, 024003 (cit. on pp. 17, 27, 105).

[64] Guillaud, J., & Mirrahimi, M. (2019). Repetition cat qubits for fault-tolerant quantum computation. *Physical Review X*, *9*(4) (cit. on pp. 17, 105).

[65] Puri, S., St-Jean, L., Gross, J. A., Grimm, A., Frattini, N. E., Iyer, P. S., Krishna, A., Touzard, S., Jiang, L., Blais, A., Flammia, S. T., & Girvin, S. M. (2020). Bias-preserving gates with stabilized cat qubits. *Science Advances*, *6*(34) (cit. on p. 17).

[66] Chamberland, C., Noh, K., Arrangoiz-Arriola, P., Campbell, E. T., Hann, C. T., Iverson, J., Putterman, H., Bohdanowicz, T. C., Flammia, S. T., Keller, A., Refael, G., Preskill, J., Jiang, L., Safavi-Naeini, A. H., Painter, O., & Brandão, F. G. (2022). Building a fault-tolerant quantum computer using concatenated cat codes. *PRX Quantum*, *3*(1) (cit. on pp. 17, 105).

[67] Burgelman, M., Rouchon, P., Sarlette, A., & Mirrahimi, M. (2022). Structurally stable subharmonic regime of a driven quantum josephson circuit. *arXiv preprint arXiv:2206.14631* (cit. on pp. 17, 27, 105).

[68] Berdou, C., Murani, A., Reglade, U., Smith, W., Villiers, M., Palomo, J., Rosticher, M., Denis, A., Morfin, P., Delbecq, M., Kontos, T., Pankratova, N., Rautschke, F., Peronnin, T., Sellem, L.-A., Rouchon, P., Sarlette, A., Mirrahimi, M., Campagne-Ibarcq, P., ... Leghtas, Z. (2022). One hundred second bit-flip time in a two-photon dissipative oscillator. *arXiv preprint arXiv:2204.09128* (cit. on pp. 18, 19, 21, 22).

[69] Carmichael, H. J. (2008). *Statistical methods in quantum optics 2*. Springer Berlin Heidelberg. (Cit. on p. 22).

[70] Wang, C., Axline, C., Gao, Y. Y., Brecht, T., Chu, Y., Frunzio, L., Devoret, M. H., & Schoelkopf, R. J. (2015). Surface participation and dielectric loss in superconducting qubits. *Appl. Phys. Lett.*, *107*(16), 162601 (cit. on p. 23)
doi: 10.1063/1.4934486.

[71] Azouit, R., Sarlette, A., & Rouchon, P. (2016). Adiabatic elimination for open quantum systems with effective lindblad master equations. *2016 IEEE 55th Conference on Decision and Control (CDC)* (cit. on p. 29).

[72] Barchielli, A., & Gregoratti, M. (2009). *Quantum trajectories and measurements in continuous time*. Springer Berlin Heidelberg. (Cit. on p. 41).

[73] Tilloy, A. (2018). Exact signal correlators in continuous quantum measurements. *Phys. Rev. A*, *98*, 010104 (cit. on p. 41).

[74] Bartolo, N., Minganti, F., Casteels, W., & Ciuti, C. (2016). Exact steady state of a kerr resonator with one- and two-photon driving and dissipation: Controllable wigner-function multimodality and dissipative phase transitions. *Phys. Rev. A*, *94*, 033841 (cit. on p. 43).

[75] Mylnikov, V. Y., Potashin, S. O., Sokolovskii, G. S., & Averkiev, N. S. (2021). Dissipative phase transition in systems with two-photon driving and dissipation near the critical point. *2021 Conference on Lasers and Electro-Optics Europe & European Quantum Electronics Conference (CLEO/Europe-EQEC)* (cit. on pp. 44, 47, 67).

[76] Johansson, J., Nation, P., & Nori, F. (2012). Qutip: An open-source python framework for the dynamics of open quantum systems. *Computer Physics Communications*, *183*(8), 1760–1772 (cit. on pp. 47, 52, 53, 65, 69).

[77] Johansson, J., Nation, P., & Nori, F. (2013). Qutip 2: A python framework for the dynamics of open quantum systems. *Computer Physics Communications*, *184*(4), 1234–1240 (cit. on pp. 47, 52, 53, 65, 69).

[78] McEwen, M., Faoro, L., Arya, K., Dunsworth, A., Huang, T., Kim, S., Burkett, B., Fowler, A., Arute, F., Bardin, J. C., Bengtsson, A., Bilmes, A., Buckley, B. B., Bushnell, N., Chen, Z., Collins, R., Demura, S., Derk, A. R., Erickson, C., ... Barends, R. (2021). Resolving catastrophic error bursts from cosmic rays in large arrays of superconducting qubits. *Nature Physics*, *18*(1), 107–111 (cit. on p. 50).

[79] Vepsäläinen, A. P., Karamlou, A. H., Orrell, J. L., Dogra, A. S., Loer, B., Vasconcelos, F., Kim, D. K., Melville, A. J., Niedzielski, B. M., Yoder, J. L., Gustavsson, S., Formaggio, J. A., VanDevender, B. A., & Oliver, W. D. (2020). Impact of ionizing radiation on superconducting qubit coherence. *Nature*, *584*(7822), 551–556 (cit. on pp. 51, 105).

[80] Cardani, L., Valenti, F., Casali, N., Catelani, G., Charpentier, T., Clemenza, M., Colantoni, I., Cruciani, A., D'Imperio, G., Gironi, L., Grünhaupt, L., Gusenkova, D., Henriques, F., Lagoin, M., Martinez, M., Pettinari, G., Rusconi, C., Sander, O., Tomei, C., ... Pop, I. M. (2021). Reducing the impact of radioactivity on quantum circuits in a deep-underground facility. *Nature Communications*, *12*(1) (cit. on pp. 51, 105).

[81] Bultink, C. C., Tarasinski, B., Haandbæk, N., Poletto, S., Haider, N., Michalak, D., Bruno, A., & DiCarlo, L. (2018). General method for extracting the quantum efficiency of dispersive qubit readout in circuit qed. *Applied Physics Letters*, *112*(9), 092601 (cit. on p. 61).

[82] Haroche, S., & Raimond, J.-M. (2006). The linblad master equation. In *Exploring the Quantum: Atoms, Cavities, and Photons* (pp. 178–189). Oxford University Press. (Cit. on p. 67).

[83] Matthaei, G., Young, L., & Jones, E. (1980). *Microwave filters, impedance-matching networks, and coupling structures*. Artech House. (Cit. on pp. 74, 75).

[84] Pozar, D. M. (2012). *Microwave Engineering* (4th ed.). Wiley. (Cit. on p. 74).

[85] Villiers, M. (n.d.). *In preparation* [Ph.D. Thesis]. ENS. (Cit. on pp. 81, 93, 118).

[86] Andrews, J. R. (2000). Broadband coaxial bias-tees. *Picosecond Pulse Labs* (cit. on p. 83).

[87] Mohan, S. S., del Mar Hershenson, M., Boyd, S. P., & Lee, T. H. (1999). Simple accurate expressions for planar spiral inductances. *IEEE Journal of solid-state circuits*, *34*(10), 1419–1424 (cit. on p. 84).

[88] Belkind, A., & Gershman, S. (2008). Plasma cleaning of surfaces. *Vacuum Coating and Technology November*, 46–57 (cit. on p. 97).

[89] AJAInternational. (n.d.). *What is ion milling ?* Retrieved October 10, 2022, from https://www.ajaint.com/what-is-ion-milling.html (cit. on p. 97).

[90] Koppinen, P., Väistö, L., & Maasilta, I. (2007). Complete stabilization and improvement of the characteristics of tunnel junctions by thermal annealing. *Applied physics letters*, *90*(5), 053503 (cit. on p. 97).

[91] Pop, I. M., Fournier, T., Crozes, T., Lecocq, F., Matei, I., Pannetier, B., Buisson, O., & Guichard, W. (2012). Fabrication of stable and reproducible submicron tunnel junctions. *Journal of Vacuum Science & Technology B, Nanotechnology and Microelectronics: Materials, Processing, Measurement, and Phenomena*, *30*(1), 010607 (cit. on p. 97).

[92] Hazard, T. M. (2019). *Improving quantum hardware: Building new superconducting qubits and couplers* [Doctoral dissertation, Princeton University]. (Cit. on p. 98).

[93] Dunsworth, A., Megrant, A., Quintana, C., Chen, Z., Barends, R., Burkett, B., Foxen, B., Chen, Y., Chiaro, B., Fowler, A., et al. (2017). Characterization and reduction of capacitive loss induced by submicron josephson junction fabrication in superconducting qubits. *Applied Physics Letters*, *111*(2), 022601 (cit. on p. 98).

[94] Chakram, S., He, K., Dixit, A. V., Oriani, A. E., Naik, R. K., Leung, N., Kwon, H., Ma, W.-L., Jiang, L., & Schuster, D. I. (2022). Multimode photon blockade. *Nature Physics*, 1–6 (cit. on p. 98).

[95] Roy, T., Li, Z., Kapit, E., & Schuster, D. I. (2021). Tomography in the presence of stray inter-qubit coupling. *arXiv preprint arXiv:2103.13611* (cit. on p. 98).

[96] Kreikebaum, J., O'Brien, K., Morvan, A., & Siddiqi, I. (2020). Improving wafer-scale josephson junction resistance variation in superconducting quantum coherent circuits. *Superconductor Science and Technology*, *33*(6), 06LT02 (cit. on p. 98).

[97] Planat, L. (2020). *Resonant and traveling-wave parametric amplification near the quantum limit* [Doctoral dissertation, Université Grenoble Alpes [2020-....]]. (Cit. on p. 98).

[98] Puertas, J. (2018). *Probing light-matter interaction in the many-body regime of superconducting quantum circuits* [Doctoral dissertation, Université Grenoble Alpes]. (Cit. on p. 98).

[99] Albertinale, E. (2021). *Measuring spin fluorescence with a microwave photon detector* [Doctoral dissertation, Université Paris-Saclay]. (Cit. on p. 98).

[100] Lescanne, R. (2020b). *Engineering multi-photon dissiption in superconducting circuits for quantum error correction* [Ph.D. Thesis]. École Normale Supérieure. (Cit. on p. 98).

[101] Vool, U., Pop, I. M., Sliwa, K., Abdo, B., Wang, C., Brecht, T., Gao, Y. Y., Shankar, S., Hatridge, M., Catelani, G., Mirrahimi, M., Frunzio, L., Schoelkopf, R. J., Glazman, L. I., & Devoret, M. H. (2014). Non-Poissonian quantum jumps of a fluxonium qubit due to quasiparticle excitations. *Phys. Rev. Lett.*, *113*(24), 247001 (cit. on p. 105).

[102] Le Régent, F.-M., Berdou, C., Leghtas, Z., Guillaud, J., & Mirrahimi, M. (2022). High-performance repetition cat code using fast noisy operations. *arXiv preprint arXiv:2212.11927* (cit. on p. 106).

RÉSUMÉ

Les bits quantiques, plus communément appelés "qubits", subissent encore trop d'erreurs dans leurs implémentations actuelles pour pouvoir être assemblés en processeur quantique pertinent. Une stratégie originale pour contrer les flips de bits consiste à encoder l'information quantique dans deux états stables d'un oscillateur qui échange des photons par paires avec son environnement. Ce mécanisme de dissipation non-linéaire est à la base d'un nouveau qubit : le qubit de chat, implémenté au sein du champ d'une cavité résonante réalisée dans un circuit supraconducteur. Ajouter des photons dans les états de la cavité accentue la séparation inter-états, ce qui permet en principe d'atteindre des temps de bit-flips macroscopiques même pour un faible nombre de photons dans la cavité. Pourtant, les réalisations expérimentales précédant cette thèse saturaient à des temps de l'ordre de la milliseconde.

Le but principal de cette thèse est de maximiser le temps de bit-flip atteignable dans un oscillateur pourvu de la dissipation à deux photons. À partir des réalisations expérimentales pré-existantes, la démarche a été de retirer du prototype tout ce qui n'était pas essentiel au processus de stabilisation à deux photons et de se placer dans un régime de paramètres expérimentaux conservateur. Toutefois, ces choix ont abouti à un taux de dissipation à un photon supérieur au taux de dissipation à deux photons, rendant caduques la préparation de superposition d'états quantiques dans la cavité, et donc aussi la mesure de temps de phase-flips.

Le résultat central de cette thèse est la démonstration expérimentale d'un temps de bit-flip de 100 secondes pour des états dans un oscillateur à dissipation à deux photons, contenant environ 40 photons. Ce travail constitue un point de référence pour les futures implémentations qui pourront revenir dans un régime pour exploiter pleinement la nature quantique de l'oscillateur à deux photons. Les performances démontrées dans cette thèse permettent ainsi d'envisager une réalisation concrète de la feuille de route menant à un ordinateur quantique universel à base de qubits de chats.

MOTS CLÉS

Correction d'erreur quantique, Circuits supraconducteurs, Jonction Josephson

ABSTRACT

Current implementations of quantum bits, also commonly called qubits, continue to undergo too many errors to be scaled into useful quantum machines. An emerging strategy is to encode quantum information in the two meta-stable pointer states of an oscillator exchanging pairs of photons with its environment, a mechanism shown to provide stability without inducing decoherence. This strategy is at the core of a recent qubit, called the cat-qubit, which is embedded in the cavity field of a superconducting resonator with tailored interaction with its environment. Adding photons in these states increases their separation, and macroscopic bit-flip times are expected even for a handful of photons, a range suitable for quantum information processing. However, the bit-flip time demonstrated in previous experimental realizations have saturated in the millisecond range.

The primary goal of this thesis work is to maximize the bit-flip time in a two-photon dissipative oscillator. To that end, we strip the prototype circuit of everything we can afford, select a parameters regime to avoid dynamical instabilities, and notice how much the bit-flip time can be increased. These choices come at the cost of a two-photon exchange rate dominated by single-photon loss, hence losing our ability to prepare quantum superposition states and measuring the phase-flip rate.

The main result of this thesis is the experimental demonstration of bit-flip times exceeding 100 seconds for computational states pinned by two-photon dissipation and containing about 40 photons. This thesis work is a solid foundation for future experiments that can gradually enter the regime suitable to implement a qubit where two-photon loss is the dominant dissipation mechanism. This experimental work supports the strategy of eradicating bit-flip errors continuously and autonomously at the single qubit level, and reserving the costly arsenal of measurement based quantum error correction to address the only significant remaining error: phase-flips. This work paves the way for cat-qubit based universal set of gates and phase-flip error correction, in line with the roadmap for a universal quantum computer.

KEYWORDS

Quantum Error Correction, Superconducting circuits, Josephson junction